Preclinical studies on susceptibility to viral infection driving lung injury and disruptions to lung development in neonates with bronchopulmonary dysplasia

Inaugural Dissertation

submitted to the

Faculty of Medicine

in partial fulfilment of the requirements

for the PhD-Degree

of the Faculties of Veterinary Medicine and Medicine

of the Justus Liebig University Giessen

by

Gunjak, Miša

of

Sarajevo, Bosnia and Herzegovina

Giessen (2025)

From the Max-Planck-Institute for Heart and Lung Research. Department IV Lung Development
Director: Prof. Dr. Werner Seeger
of the Faculty of Medicine of the Justus-Liebig-Universität Gießen
and Department of Translational Pulmonology. Heidelberg University Hospital
Director: Prof. Dr. Rory Morty

First Supervisor and Committee Member: Prof. Dr. Werner Seeger

Second Supervisor and Committee Member: Prof. Dr. Friedemann Weber

Committee Members: Prof. Dr. Martin Diener
Prof. Dr. Friedemann Weber
Prof. Dr. Werner Seeger
Prof. Dr. Ulrich H. Thome

Date of Doctoral Defense:

30 April 2026

I Table of contents

II Table legends

III Figure legends

IV Abbreviations

°C	Degree Celsius
µl	Microliter
2PEA	Two-photon excited autofluorescence
a.u.	Arbitrary unit
AEC1	Alveolar epithelial cell type I
AEC2	Alveolar epithelial cell type II
AM	Alveolar macrophage
ARDS	Acute respiratory distress syndrome
ATCC	American Type Culture Collection
BPD	Bronchopulmonary dysplasia
CD45	Cluster of differentiation 45
CMV	Cytomegalovirus
CoV	Coronavirus
CPAP	Continuous positive airway pressure
Ct	Threshold cycle
DAPI	4′,6 diamidino-2-phenylindole
DC	Dendritic cell
DNase I	Deoxyribonuclease I
dNTP	Deoxynucleotide triphosphate
E	Embryonic day
ECM	Extracellular matrix
ELBW	Extremely low birth weight
EOS	Early-onset sepsis
ExAM	Exudate macrophage

F	Fusion protein
FACS	Fluorescence-activated cell sorting
FiO_2	Fraction of inspired oxygen
FITC	Fluorescein isothiocyanate
FSC-A	Forward scatter area
FSC-H	Forward scatter height
G	Gauge
g	Gram
G-CSF	Granulocyte colony-stimulating factor
GEMs	Gel Beads-in-emulsion
GM-CSF	Granulocyte-macrophage colony-stimulating factor
h	Hour
hBoV	Human bocavirus
HEPES	4-(2-hydroxyethyl)-1-piperazineethanesulfonic acid
hMPV	Human metapneumovirus
hRSV	Human respiratory syncytial virus
hRV	Human rhinovirus
HSV	Herpes simplex virus
IC	Invasive candidiasis
ICU	Intensive care unit
IFN-γ	Interferon-γ
IL	Interleukin
IN	Intranasally
IP	Intraperitoneally
IVC	Individually ventilated cage

kg	Kilogram
L	Polymerase
LIMMA	Linear models for microarray data
LPS	Lipopolysaccharide
M	Matrix protein
M	Molar
MCP	Monocyte chemoattractant protein
MHC	Major histocompatibility complex
MIP	Macrophage inflammatory protein
ml	Millimeter
M-MLV	Moloney Murine Leukemia Virus
N	Nucleocapsid protein
NEC	Necrotizing enterocolitis
ng	Nanogram
NICU	Neonatal intensive care unit
NIV	Non-invasive ventilation
NK	Natural killer
NS1	Non-structural protein 1
NS2	Non-structural protein 2
P	Postnatal day
P	Phosphoprotein
P/S	Penicillin-Streptomycin
PBS	Phosphate-buffered saline
PBSTT	Phosphate-buffered saline with Tween-20 and Triton X-100
PBT	Pixels below the threshold

PCR	Polymerase chain reaction
PCW	Post-conception week
PFA	Paraformaldehyde
PFU	Plaque-forming unit
PIV	Parainfluenza virus
PMT	Photomultiplier tube
Polr2A	RNA polymerase II
PVM	Pneumonia virus of mice
qPCR	Quantitative polymerase chain reaction
R_0	Basic reproductive number
RDS	Respiratory distress syndrome
ROI	Region of interest
ROP	Retinopathy of prematurity
rpm	Revolutions per minute
RPMI	Roswell Park Memorial Institute
RSV	Respiratory syncytial virus
s	Second
SH	Small hydrophobic protein
SHG	Second harmonic generation
SOP	Standard operating procedure
SpO_2	Oxygen saturation
SSC-A	Side scatter area
Th17	T helper 17 cell
TLR	Toll-like receptor
TNF	Tumor necrosis factor

TR-AM	Tissue-resident alveolar macrophage
TransM	Transitional macrophage
UMAP	Uniform manifold approximation and projection
Wt	Wild type

V Abstract

Bronchopulmonary dysplasia (BPD) is the most common complication of preterm birth, with significant morbidity and mortality, and is experimentally modelled by exposure of newborn mice to hyperoxia to mimic oxygen supplementation of preterm infants. Infants with BPD have a higher risk of acquiring a respiratory virus infection and have a worse disease course. The pathophysiological mechanisms underlying this increased risk of infection and more severe pathology have not been clarified, but include oxygen creating a more permissive environment for virus infection, or oxygen modulating the lung inflammatory response to virus infection. When neonatal mice were exposed to hyperoxia (85% O_2) from birth, and then challenged with pneumonia virus of mice (PVM) on postnatal day (P)4, all hyperoxia-exposed pups infected at a 1:1,000 dilution of viral stock exhibited 100% mortality by P12. In contrast, mice maintained in room air survive PVM infection over a range of virus doses (1,1000, 1:2,500, or 1:5,000), highlighting a stark, dose-dependent synergy between oxygen toxicity and viral challenge. By P11, lungs from hyperoxia-exposed mice, with or without PVM infection, exhibit pronounced alveolar simplification, with enlarged airspaces and diminished septation. The PVM infection under conditions of hyperoxia provokes marked inflammatory infiltration, whereas lungs infected under conditions of normoxia (21% O_2) retain normal architecture. Whole-body plethysmography revealed a dose-dependent decline in tidal volume, expiratory volume, minute volume, and breathing frequency in hyperoxia-infected mice. Despite identical early viral replication across both oxygen conditions, the addition of hyperoxia before and concomitant with virus infection reshapes inflammatory signaling and tissue remodeling. Gene expression in lung homogenates indicated early increases of *Ccl2*, *Cxcl10*, and *Ccl3* mRNA transcript abundance under hyperoxia. Antibody microarrays revealed a shift from homeostatic chemokines (CCL2, IL-25) to pro-inflammatory and fibrotic mediators (IL-6, IL-8, TGF-β1-3) upon infection, with prior and concomitant hyperoxia magnifying CCL17, IL-15, and lung fibrosis pathways. Immune cell profiling using single-cell RNA sequencing revealed that hyperoxia depleted tissue-resident alveolar macrophages (TR-AM) and expanded exudate macrophages, dendritic cells, and neutrophils. Under normoxia, PVM infection enriches a virus-responsive TR-AM subset (AM_PVM), while hyperoxia completely eliminates these protective responses. Single-cell transcriptomics confirmed the loss of AM_HYX (a stress-adapted

macrophage subset) and AM_PVM cells in hyperoxia-infected mice, with extensive dendritic cell expansion.

Intranasal clodronate liposome–mediated TR-AM depletion in normoxia-treated, virus-infected animals mimicked the lethal phenotype noted in hyperoxia-infected animals, with 100% mortality by P15. These mice exhibited excessive lung inflammation, impaired respiratory function, and a hyperoxia-like proteomic signature, even as viral loads reduced. Therefore, TR-AM dysfunction and skewed inflammatory chemokine signaling, and not viral load, were associated with fatal outcome. Together, these findings reveal that hyperoxia disrupts macrophage-mediated immune regulation in the newborn mouse lung, converting a balanced antiviral defense into maladaptive inflammation. Strategies to preserve or restore TR-AM function may therefore protect preterm infants from severe respiratory viral disease.

These novel findings might explain the predisposition of BPD patients to a high risk of respiratory virus infection and worse clinical outcomes.

VI Zusammenfassung

Die Bronchopulmonale Dysplasie (BPD) ist die häufigste Komplikation der Frühgeburt und geht mit erheblicher Morbidität und Mortalität einher. Experimentell wird sie durch die Exposition neugeborener Mäuse gegenüber Hyperoxie modelliert, um die Sauerstoffsupplementierung von Frühgeborenen nachzuahmen. Frühgeborene mit BPD weisen ein erhöhtes Risiko für respiratorische Virusinfektionen auf, die zudem mit einem schwereren Krankheitsverlauf einhergehen. Die pathophysiologischen Mechanismen, die diesem erhöhten Infektionsrisiko und der verschärften Pathologie zugrunde liegen, sind bislang nicht vollständig geklärt; diskutiert werden sowohl die durch Sauerstoff geschaffene permissivere Umgebung für Virusinfektionen, als auch die Sauerstoff-induzierte Modulation der pulmonalen Immunantwort. Wurden neugeborene Mäuse unmittelbar nach der Geburt Hyperoxie (85 % O_2) ausgesetzt und am postnatalen Tag (P)4 mit dem Pneumonievirus der Maus (PVM) infiziert, verstarben alle hyperoxie-exponierten Jungtiere bei einer Infektionsdosis von 1:1.000 bis P12. Im Gegensatz dazu überlebten Tiere unter Normoxie (21 % O_2) eine PVM-Infektion über ein Spektrum von Virusdosen (1:1.000, 1:2.500, 1:5.000), was eine deutliche, dosisabhängige Synergie zwischen Sauerstofftoxizität und Virusinfektion offenbart. Ab P11 zeigten die Lungen hyperoxie-exponierter Tiere, unabhängig von einer zusätzlichen PVM-Infektion, eine ausgeprägte Alveolarvereinfachung mit vergrößerten Lufträumen und reduzierter Septierung. PVM-Infektionen unter Hyperoxie führten zu massiver inflammatorischer Infiltration, während unter Normoxie die Lungenarchitektur weitgehend erhalten blieb. Die Ganzkörperplethysmographie zeigte bei hyperoxie-infizierten Mäusen eine dosisabhängige Abnahme von Atemzugvolumen, Exspirationsvolumen, Minutenvolumen und Atemfrequenz. Trotz identischer früher Virusreplikation unter beiden Sauerstoffbedingungen führte die Kombination von Hyperoxie vor und während der Infektion zu einer tiefgreifenden Umgestaltung des inflammatorischen Signals und der Gewebeantwort. Genexpressionsanalysen aus Lungenhomogenaten belegten frühe Anstiege von *Ccl2*, *Cxcl10* und *Ccl3* mRNA unter Hyperoxie. Antikörper-Microarrays zeigten einen Wechsel von homöostatischen Chemokinen (CCL2, IL-25) zu proinflammatorischen und fibrotischen Mediatoren (IL-6, IL-8, TGF-β1–3), wobei vorherige und gleichzeitige Hyperoxie eine Verstärkung von CCL17, IL-15 und fibrotischen Signalwegen hervorrief.

Immunzellanalysen mittels Einzelzell-RNA-Sequenzierung ergaben, dass Hyperoxie gewebsresidente alveoläre Makrophagen (TR-AM) depletiert und exsudative Makrophagen, dendritische Zellen sowie Neutrophile expandiert. Unter Normoxie führte eine PVM-Infektion zu einer Anreicherung einer virusreaktiven TR-AM-Subpopulation (AM_PVM), die unter Hyperoxie vollständig eliminiert wurde. Die Einzelzell-Transkriptomik bestätigte den Verlust sowohl von stressadaptierten AM_HYX, als auch von AM_PVM-Zellen in hyperoxie-infizierten Tieren, begleitet von einer massiven Expansion dendritischer Zellen.

Die intranasale Depletion von TR-AM mittels Clodronat-Liposomen bei normoxie-behandelten, virusinfizierten Tieren reproduzierte das letale Phänotyp-Muster der hyperoxie-infizierten Mäuse und führte zu 100 % Mortalität bis P15. Diese Tiere zeigten eine exzessive pulmonale Inflammation, eine eingeschränkte Atemfunktion und ein Hyperoxie-ähnliches proteomisches Profil, trotz abnehmender Viruslast. Somit waren nicht die Viruslast, sondern TR-AM-Dysfunktion und fehlgeleitete Chemokin-Signale mit dem fatalen Verlauf assoziiert. Insgesamt zeigen diese Daten, dass Hyperoxie die makrophagenvermittelte Immunregulation in der Lunge neugeborener Mäuse stört und eine ausbalancierte antivirale Abwehr in eine maladaptive Inflammation umwandelt. Strategien zur Erhaltung oder Wiederherstellung der TR-AM-Funktion könnten daher Frühgeborene vor schweren viralen Atemwegsinfektionen schützen.

Diese neuartigen Erkenntnisse liefern eine mögliche Erklärung für die Prädisposition von BPD-Patienten zu einem erhöhten Risiko für Virusinfektionen der Atemwege und verschlechterten klinischen Verläufen.

1. Introduction

1.1. Lung development

The lungs are the key organs of the respiratory system, the main function of which is facilitating the exchange of oxygen and carbon dioxide between the external environment and the bloodstream (1). Gas exchange occurs in the alveoli, tiny air sacs located terminally at the end of the bronchioles within the lungs. This process takes place across a double alveolo/capillary barrier, which consists of an epithelial layer supported by extracellular matrix and capillaries surrounding it. In order to achieve maximum gas exchange efficiency, this barrier must have a large surface area but a thin diffusion barrier (2).

The process of lung development aims to maximize the available surface area for gas-exchange, and can be divided into five developmental stages: embryonic, pseudoglandular, canalicular, saccular, and alveolar; grouped into two phases, early, generally the prenatal period, and late, generally the postnatal period, of lung development (3). The developmental stage of the lungs at birth varies significantly across species, including between humans and mice. While term mice are born during the saccular phase, term humans are born in the alveolar phase (4). During gestation, the fetal lungs must undergo substantial morphological changes to develop into a fully functional organ capable of respiration and gas exchange at birth (5). The lung and trachea are derived from the anterior foregut endoderm, which also gives rise to the esophagus, thyroid, and liver (1). Early lung development involves the progressive division of airways to form a branched lung structure. The two primary lung buds develop around embryonic day (E)9.5 in mice and approximately 28 days post-conception in humans, initiating the embryonic phase of lung development, at 4-7 weeks in humans and E9.5–E12.5 in mice. At this stage, the single foregut tube anterior to the lung buds then separates into dorsal and ventral components: a dorsal esophagus that ends at the stomach and a ventral trachea that connects to the lung buds (6). The embryonic and pseudoglandular (5–17 weeks in humans; E12.5–E16.5 in mice) stages are distinguished by branching morphogenesis, a tightly regulated process that generates a complex tree-like airway structure with thousands of terminal branches (1). This is followed by the canalicular stage (16–26 weeks in humans; E16.5–E17.5 in mice), which is marked by the thinning of interstitial tissue and the

expansion ("opening") of air spaces in the developing lung, characterizing the beginning of the alveolarization (7).

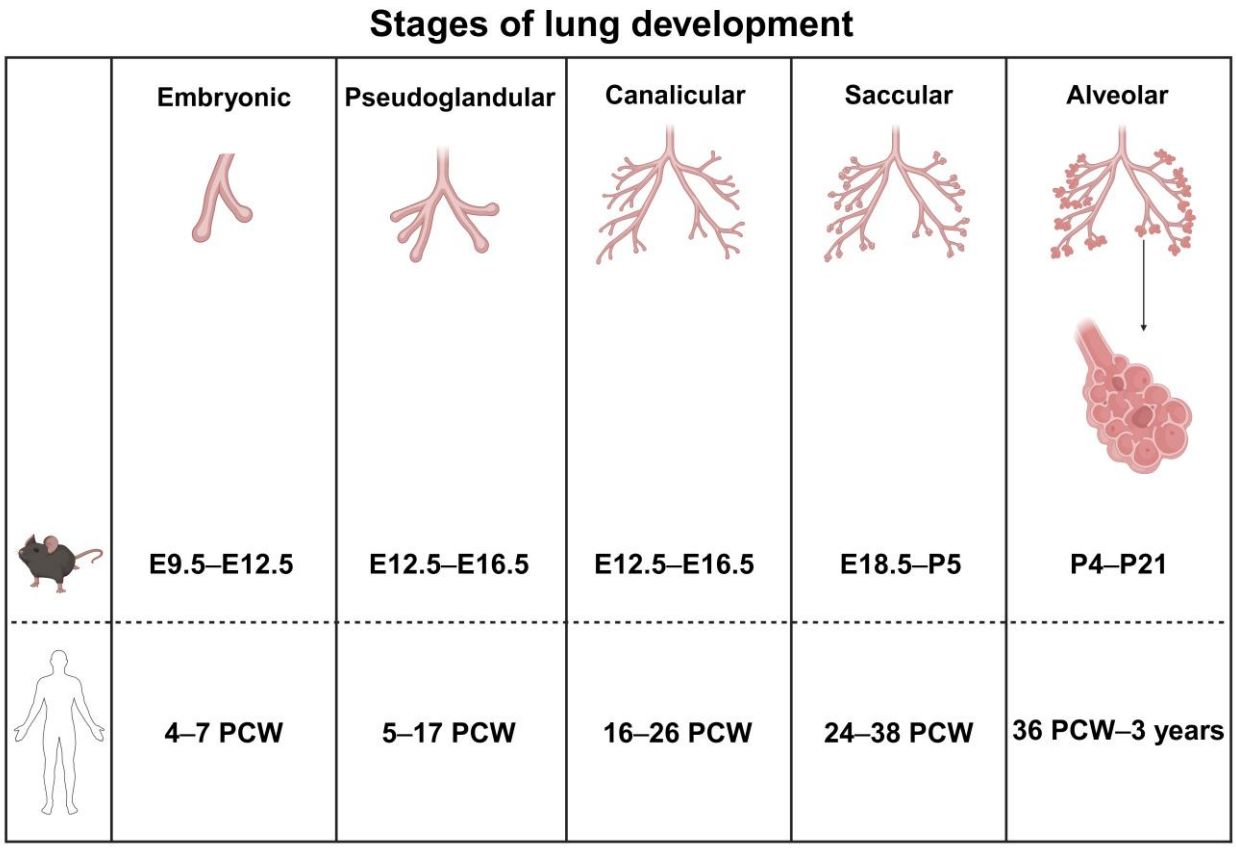

Figure 1. Stages of lung development in mouse and human.

Lung development progresses through five conserved stages: embryonic, pseudoglandular, canalicular, saccular, and alveolar. Each stage is characterized by distinct morphological features and branching patterns (illustrated schematically). Developmental timing differs between mouse (E9.5–P21) and human (4–7 PCW to 3 years), with mouse alveolarization occurring entirely postnatally. The alveolar stage shows mature alveolar clusters (magnified view) representing the final gas-exchange structures. E, embryonic day; P, postnatal day; PCW, post-conception weeks.

At this stage bronchioles emerge, laying the foundation for gas exchange units concurrently. Epithelial differentiation occurs, establishing structural distinctions between conducting airways and respiratory airways, as well as forming acini and ventilatory units. Furthermore, during the canalicular stage, the distal epithelial cells differentiate into alveolar epithelial cell type 1 (AEC1) and alveolar epithelial cell type 2 (AEC2). Where AEC1 enable gas exchange, AEC2 secrete surfactant and are progenitors of AEC1. The AEC2 differentiation is characterized by lamellar body formation and surfactant secretion, an important determinant for the survival of

extremely preterm humans (6, 8). The first air-blood barrier is created by the interaction between the alveolar epithelium and mesenchymal capillaries.

This is followed by the saccular stage (24–38 weeks in humans; E18.5–postnatal day (P)5 in mice), when terminal branches remodel to give rise to clusters of epithelial sacs, which will eventually form alveoli. It is during this stage that the lungs become prepared for respiration at birth, secondary to the mature differentiation of alveolar pneumocytes and the formation of respiratory units. Precursor cells of smooth muscle migrate into the developing lung to construct a fibrous network of elastic fibers and collagen fibrils critical for the later process of alveolarization. The alveolarization process is characterized by the appearance of secondary septa in terminal airways and the formation of definitive cup-shaped alveoli with double capillary walls. Alveolar expansion and septation at this stage ensure enough surface area for gas exchange. In mice, alveolarization takes place postnatally between P4 and P21, whereas in humans, this process extends for at least the first two years of life (9). After that, alveoli are generated at a rate commensurate with lung growth.

1.2. Preterm birth

Preterm birth, defined as delivery before 37 completed weeks of gestation, is increasingly a significant burden on global public health systems and one of the most common causes of neonatal morbidity and mortality, especially among children under five years of age (10). Neonatal outcomes are related to the gestational age, where extremely preterm infants (<28 weeks of gestation) are at the most significant risk of mortality and morbidity, followed by very preterm (28 to <32 weeks) and moderate to late preterm (32 to <37 weeks) gestation. Preterm birth is related to a variety of short- and long-term adverse health outcomes that extend beyond the neonatal period. Such outcomes include suboptimal growth trajectories, cognitive and developmental disabilities, and increased risk of early-onset chronic diseases (11-13). Moreover, common complications of preterm birth span from respiratory disorders such as bronchopulmonary dysplasia (BPD), vision impairments including retinopathy of prematurity (ROP), gastrointestinal diseases, for example, necrotizing enterocolitis (NEC), neurological complications, and various neurodevelopmental impairments (14-16). Global health data collected from 2000 to 2014 show a significant increase in the preterm birth rate, from 9.8% to 10.6% (10), from which each

year approximately 1 million infants die due to complications directly linked to preterm birth (17). In 2020, an estimated 13.4 million infants were born prematurely worldwide, which accounted for 9.9% of all live births. The incidence of preterm birth varied significantly across the globe; southern Asia and sub-Saharan Africa accounted for 55.6% of all global preterm births (13). In high-income countries such as the United States, preterm birth rates have decreased in recent years but remain unequally distributed by race, religion, and socioeconomic status, externalizing inequities in social determinants of health for maternal and newborn care (18).

1.3. Risk factors for preterm birth

Known risk factors that contribute to and are correlated with preterm birth can include social determinants such as socioeconomic status and education level, which influence the level of healthcare access. Furthermore, physical determinants such as prior preterm births, infections, interpregnancy intervals, various substance abuse, multiple gestations, and maternal age also pose as risk factors for preterm birth (19-21). For women across all socioeconomic backgrounds, age is a common potential risk factor, where pregnancy younger than 18 or older than 35 contributes significantly to the risk of preterm birth (22, 23). Another risk factor that poses a significant risk for preterm birth is intrauterine infection, specifically prior to 30 weeks of gestation. Bacterial infections of the uterine environment lead to the release and accumulation of bacterial cytotoxins, namely endotoxin and exotoxin. These bacterial cytotoxins induce inflammatory cytokine signaling and cascading from the decidua and fetal membranes, leading to uterine contractions, preterm birth, and potential fetal sepsis (24).

1.4. Management of preterm birth

The management of preterm birth is multifaceted, including prevention and various treatment strategies in order to provide the most streamlined positive health outcome. Risk factor identification is central to the management of preterm birth for both prevention and treatment, allowing medical personnel to address the health concern at hand with a multitude of treatment options. Some preventative treatment options include progesterone administration to inhibit uterine contractions and induce uterine relaxation for high-risk pregnancies. Other common antenatal treatments are the use

of corticosteroids to promote fetal lung maturation and magnesium sulfate injection to increase neuroprotective activity. Often, when an infant is born prematurely, mechanical ventilation is utilized (25-28). Early on, invasive mechanical ventilation, such as endotracheal intubation, was the primary approach to managing early respiratory dysfunction, such as severe respiratory distress syndrome (RDS). However, increased understanding of neonatal lung physiology and the harmful effects that mechanical ventilation causes both mechanically and physiologically on the developing lung has significantly impacted how clinicians employ its use on premature infants in the clinic (29).

In the 1980s, the introduction of artificial surfactant therapy in clinical practice represented a major advance in the ever-evolving management of RDS (30). Surfactant replacement therapy involves administering exogenous surfactant to neonates, reducing surface tension within the alveoli, and leading to increased lung compliance and gas exchange. In the first 1-2 h after birth, surfactant also participates in facilitating two important processes: enhanced fetal lung liquid clearance and airway aeration. Prior to surfactant therapy, treatment options for prematurely born infants heavily relied on invasive mechanical ventilation, leading to a considerable increase in morbidity and mortality in comparison with current available treatment strategies. Surfactant administration has been found to not only reduce mortality but also the incidence of BPD, a common disorder in very low birth weight infants (31-35). In recent years, non-invasive ventilation (NIV) strategies have gained popular attention in the approach to treatment strategies, through its ability to minimize injury to the lung, while improving the health outcome of the premature infant. Continuous positive airway pressure (CPAP) delivers respiratory support by maintaining positive airway pressure to prevent the collapse of alveoli and the maintenance of spontaneous breathing. Several randomized controlled trials evaluating early CPAP administration, compared to invasive mechanical ventilation, demonstrated improved respiratory outcomes, including lower rates of BPD and other complications. Significantly, infants born prematurely and who were transitioned to CPAP (within a certain period) statistically require fewer days on mechanical ventilation, and have a lower reported rate of mortality (36-39). Treatment options are important for managing preterm birth through improving respiratory health outcomes and, at the same time, mitigating trauma caused by invasive intervention.

1.5. Bronchopulmonary dysplasia

Bronchopulmonary dysplasia is a chronic lung disease most commonly seen in very low birth weight preterm infants, who are dependent for long periods on mechanical ventilation or oxygen. Survivors of BPD have chronic respiratory symptoms and abnormal lung function even as adults, making BPD a leading cause of pediatric lung disease (40, 41). Bronchopulmonary dysplasia was first described in 1967 by Dr William Northway and colleagues as findings on chest X-ray in preterm neonates that had characteristic changes in lung parenchyma (42). Further studies found associations between chronic lung disease and mechanical ventilation and high fraction of inspired oxygen (FiO_2) in the early postnatal period. Bronchopulmonary dysplasia is the consequence of abnormal lung development occurring during the late canalicular and early saccular stages and is often referred to as "growth arrest." Defining features of BPD include alveolar simplification, pulmonary vascular dysangiogenesis, pro-inflammatory stimuli, and pulmonary inflammatory response. More specifically, alveolar simplification is described as having impaired septation and hypoplasia, leading to reduced alveolar surface area available for gas exchange. Moreover, due to the cell death of critical cells required for alveolar and vascular development, and massive remodeling of the extracellular matrix, there is increased thickening of the muscular layer between alveoli and pulmonary arterioles. Consequently, this increases the pulmonary vascular resistance and contributes to increased pulmonary hypertension, morbidity, and mortality.

Pro-inflammatory stimuli or factors, including congenital or nosocomial infections, mechanical ventilation, or oxygen toxicity during the perinatal period, further increase the inflammatory response (40). The combined recruitment of immune cells such as neutrophils and macrophages results in the increased classical pro-inflammatory cytokine concentrations, including but not limited to interleukin (IL)-8, IL-6, IL-1β, and tumor necrosis factor (TNF)-α (43). Though it is unknown whether BPD is directly attributable to prematurity itself or other related factors, known major attributing risk factors for BPD include prematurity, fetal growth restriction, antenatal infection, prolonged mechanical ventilation, oxygen toxicity, and postnatal infection (40, 44). Dynamic improvements in perinatal care over the past several decades have continuously increased survival odds of very preterm infants. The main interventions utilized are antenatal corticosteroids, surfactant therapy, new ventilator strategies, and

patent ductus arteriosus management (45). Current research on BPD pathophysiology is limited due to a paucity of human samples; thus, current research is largely reliant on the use of animal models, mainly rodents such as mice and rats. These species are the preferred species for animal models due to quick gestation time and rapid postnatal lung maturation, where lung development is largely completed by two weeks in mice and three weeks in rats. Additionally, rodents are widely available for breeding and are subject to less stringent regulatory restrictions in comparison with larger vertebrates and non-human primates. These models play an important role in testing therapeutic strategies and driving the screening process for potential drug candidates (46).

1.6. Infections in preterm and term newborns

Neonatal infections are a group of diseases of newborns, caused by pathogenic and opportunistic microorganisms, such as bacteria, viruses, and fungi. These infections can manifest as sepsis, pneumonia, meningitis, and other sequelae, accounting annually for up to 23.4% of cases of neonatal mortality worldwide (47, 48). The developing neonatal immune system and environment pose a major risk for increased susceptibility to infections. Moreover, preterm infants possess a more underdeveloped immune system in comparison to full-term neonates, further increasing the risk of infection (49, 50). Common maternal and environmental factors contribute to increased risk. Vertical transmission is still the primary route for early-onset neonatal infections, involving the direct encounter with maternal vaginal flora during childbirth or via ascending infections from the maternal perineum. Mother-related risk factors such as bacterial colonization, chorioamnionitis, and bacteremia significantly add to the susceptibility of the neonate to infection. It is important to note that asymptomatic maternal colonization with pathogenic bacteria may cause severe infections in neonates (48, 51, 52).

1.6.1. Neonatal bacterial infections

Neonatal bacterial infections within the first 28 days of life affect an estimated 3 million neonates annually, contributing substantially to global neonatal morbidity and mortality (53-55). Early-onset sepsis (EOS), defined as culture-confirmed infection within the first 72 h post-birth, varies in incidence based on gestational age. Among neonates

born 29 – 33 weeks of gestation, the incidence is approximately 6.21 per 1,000 live births. This rate decreases to 0.73 and 0.56 per 1,000 live births for late preterm (34–36 weeks) and term (≥37 weeks) infants, respectively (56). Despite higher rates of EOS in extremely preterm neonates, late preterm and term infants account for a greater absolute number of cases due to their larger population size. Prematurity affects approximately 11% of live births globally, with 84.7% occurring in the moderate/late preterm period (32–<37 weeks of gestation) (10). The etiology of EOS encompasses both Gram-positive and Gram-negative pathogens, with Group B *Streptococcus* disproportionately affecting term infants, and *Escherichia coli* predominantly affecting preterm neonates with EOS (56).

1.6.2. Fungal infections

Fungal infections in neonates are primarily caused by the species within the genus *Candida*, of which *C. albicans* and *C. parapsilosis* are the most frequently reported pathogens. Extremely low birth weight (ELBW) infants, defined as those weighing less than 1,000 grams at birth, are particularly susceptible to invasive candidiasis (IC) during their stay in the neonatal intensive care unit (NICU). In large multicenter studies conducted in the United States, the incidence of IC among ELBW infants has been reported to range from approximately 2.4% to 20.4% (57). Invasive candidiasis in ELBW infants is associated with a substantial increase in mortality, with rates often exceeding 30%. Furthermore, survivors of neonatal IC are at heightened risk for a spectrum of adverse neurodevelopmental outcomes, including cerebral palsy, cognitive impairment, hearing loss, visual deficits, and other long-term neurological disabilities (58, 59).

1.6.3. Viral infections

Viral infections pose a significant challenge in neonatal medicine due to the immature immune systems of preterm infants. Respiratory viral infections are particularly concerning as a consequence of their prevalence and potential for severe complications (60). Common respiratory viruses afflicting human populations include respiratory syncytial virus (RSV), human rhinovirus (hRV), influenza virus, human metapneumovirus (hMPV), coronavirus (CoV), and human bocavirus (hBoV) (61, 62).

Systemic viral infections caused by herpes simplex virus (HSV) and cytomegalovirus (CMV) also present ongoing challenges in neonatal care (63).

1.6.3.1. Respiratory syncytial virus

Respiratory syncytial virus is a leading cause of lower respiratory tract infection, mortality, and hospitalization of infants and young children worldwide (64). It spreads rapidly within communities, with most individuals contracting it by the age of two (65). The basic reproductive number (R_0) for RSV has been estimated at approximately 3.0 across various seasons and locations, underscoring its high transmissibility (66). Furthermore, RSV can reinfect individuals throughout their lives, typically causing mild cold-like symptoms in healthy immunocompetent adults and children (67). However, in infants, young children, and immunocompromised individuals, RSV often infects the lower respiratory tract, leading to severe illnesses that can require prolonged hospital stays and even fatality (68-70). As such, RSV is the most common cause of acute lower respiratory tract infections in children under five years old, affecting 33.1 million globally each year and resulting in 59,600 in-hospital deaths annually (70). Despite advancements in medical care and treatment, RSV-associated morbidity and mortality remain disproportionately high in low- and middle-income countries, particularly among children under five years of age (71). Severe RSV infection can further lead to chronic respiratory complications, with preterm infants particularly vulnerable due to their immature immune systems. Understanding and targeting innate immunity is, therefore, critical for developing effective preventive and therapeutic strategies (72).

Respiratory syncytial virus was first isolated in the mid-1950s from chimpanzees with respiratory illnesses and initially named "chimpanzee coryza agent" (73). It was later identified in infants with severe lower respiratory tract infection and renamed respiratory syncytial virus. Over time, its pervasive impact on early childhood health has become widely recognized. RSV resurfaces annually across regions, posing a significant threat to vulnerable populations, particularly during well-defined seasonal epidemics. In temperate climates, RSV activity typically begins in late autumn and peaks in winter, with most epidemics lasting between 2 and 5 months. In tropical regions, RSV circulation often coincides with the rainy season and can persist for longer periods (74-76).

Respiratory syncytial virus is an enveloped virus of the *Pneumoviridae* family, genus *Orthopneumovirus*. Its 15.2-kilobase negative-sense, single-stranded RNA genome encodes 11 proteins, 8 of which are structural. The viral envelope contains 3 transmembrane glycoproteins responsible for mediating distinct stages in viral pathogenesis. The first structural protein, large attachment glycoprotein (G), facilitates the viral attachment to epithelial cells, while the second structural protein, fusion protein (F), mediates fusion between the viral and host cell membranes. The third surface glycoprotein, small hydrophobic protein (SH), has shown some viroporin activity, but its exact role remains unknown. Other structural proteins include L (polymerase), N (nucleocapsid), P (phosphoprotein), M (matrix), and M2-1/M2-2 cofactor proteins. Additionally, RSV also expresses non-structural proteins NS1 and NS2, which are only expressed during cell infection and are not included in the virion. NS1 and NS2 proteins interfere with the host's innate antiviral immune response. NS1, similar in structure to the M protein, modulates interferon responses by obstructing the recruitment of transcription regulators. NS2 promotes autophagy by stabilizing the Beclin-1 protein, which prevents the production of inflammatory cytokines and inhibits apoptosis, a critical defense mechanism against viral infections (77, 78).

The clinical syndrome of RSV bronchiolitis is driven primarily by the host inflammatory response rather than direct viral cytopathology. This explains the weak correlation between viral load and disease severity, while increased concentration of cytokines and chemokines was associated with decreased disease severity (79-81). A combination of clinical, virological, and environmental factors influences severe RSV disease in children (82, 83). The RSV-induced immune responses are transient, as protective antibodies and T cells wane within weeks to months, resulting in frequent reinfections (84, 85). Maternal antibodies provide initial protection against RSV; however, their effectiveness is dependent on gestational age, with reduced transfer observed in infants born before 33 weeks of gestation (86).

The innate immune system's first line of defense against RSV plays a pivotal role in reducing disease severity. This process begins with RSV binding to nasal epithelial cells, triggering an early inflammatory response mediated by toll-like receptors (TLR-2, TLR-3, TLR-4, TLR-7). This activation induces the production of cytokines such as IL-6, IL-8, and type I and III interferons by alveolar macrophages (AM) and epithelial cells. These cytokines recruit neutrophils, monocytes, and dendritic cells (DC) to the

lungs. Interestingly, viral proteins such as soluble G protein, NS1, and NS2 suppress the host's type I interferon response, highlighting potential therapeutic targets (77).

Preterm infants exhibit heightened vulnerability to infections from diverse pathogens (87), and they face a significantly elevated risk of rehospitalization due to respiratory illnesses. Studies demonstrate that the hospital admission rate for respiratory infections in preterm infants is nearly twice that of full-term infants, with respiratory infections accounting for nearly half of all rehospitalizations among very preterm survivors during the first year of life (88). These complications result in prolonged hospital stays, higher rehospitalization rates, and elevated overall mortality compared to full-term infants (88, 89). This is highlighted in a recent meta-analysis published in *The Lancet*, which reviewed 64 global studies on RSV burden from 1995 to 2021. It revealed that preterm infants experience disproportionately high rates of RSV-associated disease, accounting for 25% of all RSV hospitalizations. In 2019 alone, approximately 1.7 million cases of RSV-associated acute lower respiratory infections were reported among premature infants globally, leading to 533,000 hospitalizations and 26,760 deaths attributable to RSV. The study categorized prematurity into early preterm (<32 weeks gestational age) and late preterm (32-37 weeks gestational age). Early-preterm infants exhibited significantly higher hospitalization rates compared to all gestational ages combined, while late-preterm infants revealed increased hospitalization rates primarily within their first six months of life. Additionally, early-preterm infants remained at elevated risk for hospitalization into their second year of life. The analysis also highlighted that a substantial proportion of RSV-related hospitalizations and deaths occurred in developing countries, 92% and 88.5%, respectively, during 2019 (90).

Among preterm patients with severe respiratory infections, the most frequently identified virus was RSV, followed by rhinovirus, HBoV, parainfluenza virus (PIV), and adenovirus (91). The burden of these infections is most pronounced within the first year of life, during which the majority of respiratory and RSV-related rehospitalizations occur (92).

Preterm infants with BPD are at an even greater risk for hospitalization due to RSV compared to preterm infants without BPD. Fourteen studies from 1987 to 2011 evaluated the risk of RSV hospitalization, reporting 16.8% among children with BPD compared to 9.1% in those without BPD. In analyses focused on preterm infants, the hospitalization rate for those with BPD was 15.2% versus 9.2% for those without BPD

(93). Additionally, Homaira *et al.* reported the incidence of RSV hospitalization (per 1,000 child-years) of 81.5 for children with BPD, 10.2 for preterm children with GA 32-36 weeks, 27.0 for preterm children with GA 28–31 weeks, 39.0 for preterm children with GA <28 weeks, and 6.7 for term children with low birthweight. In the other study, by Boyce *et al.*, during their first year of life, children with BPD had an estimated 12 times higher RSV hospitalization rate compared to children born at term with no underlying medical condition (94). Children with BPD face a substantially greater risk of requiring intensive care unit (ICU) admission following RSV infection compared to those without BPD. Multiple studies consistently demonstrate that BPD not only increases the likelihood of severe RSV illness but also raises the chances of needing advanced respiratory support, such as oxygen supplementation and mechanical ventilation. The severity of BPD further amplifies these risks, making critical care interventions more common among this group. In contrast, children without BPD or with milder forms of the condition are much less likely to experience such severe complications or require ICU-level care (93).

1.7. Oxygen therapy in the management of preterm infants

Oxygen therapy remains a cornerstone in the management of preterm infants, particularly those born extremely preterm, defined as infants delivered before 28 weeks of gestation. Despite its essential role in neonatal care, prolonged or excessive oxygen exposure can lead to severe complications in preterm infants. Current evidence emphasizes the importance of carefully titrating oxygen therapy to mitigate its dual potential for beneficial and harmful effects. Bronchopulmonary dysplasia remains a significant concern, with oxygen therapy identified as a contributing factor to its development. Preterm infants often need supplemental oxygen due to their underdeveloped lungs and respiratory system (95). The primary objective of oxygen therapy is to ensure adequate oxygenation to support the function and development of vital organs. However, determining the optimal oxygen saturation (SpO_2) targets for preterm infants remains a topic of ongoing research and debate.

Recent studies have explored the impact of various oxygen saturation targets on neonatal outcomes. A large multicenter trial, coordinated in the United States, Australia, New Zealand, Canada, and the United Kingdom, demonstrated that targeting lower oxygen saturations (85–89%) reduced the risk of ROP but was associated with a potential increase in mortality compared to higher saturation targets

(91–95%) (96). This underscores the delicate balance required when managing oxygen therapy in preterm infants. The timing and method of oxygen delivery are critical factors influencing outcomes. For example, early application of CPAP has been shown to reduce the need for mechanical ventilation and improve outcomes in very preterm infants (97, 98). For extremely preterm infants born at less than 32 weeks of gestation, recent evidence suggests that using higher initial oxygen concentrations may lower mortality risk (99). For ongoing management, SpO_2 targets between 90-94% are generally recommended by multidisciplinary expert groups, with alarm limits set at 89 and 95% (100).

Hyperoxia promotes inflammation, contributes to acute lung injury, and weakens the body's antimicrobial defenses. High concentrations of inspired oxygen profoundly affect immune cell function through various mechanisms. In lung tissue, it reduces the abundance of immunoregulatory cells, such as regulatory B cells and myeloid regulatory cells. It decreases the proliferation of AMs, myeloid regulatory cells, and monocytes. Furthermore, it induces an abnormal macrophage phenotype characterized by elevated expression of markers such as CD44, CD68, CD11c, PD-L1, and CD205 (101). Short-term hyperoxia alone does not significantly alter cytokine levels but can modulate cytokine responses in the presence of pre-existing inflammation. For instance, hyperoxia has been shown to reduce CCL2 levels in inflamed airways and also skews the immune response toward a Th17 phenotype, which is associated with oxidative stress-induced tissue damage and neutrophil infiltration into the lungs and airways (102). Additionally, hyperoxia can interfere with DC development and recruitment, critical for antigen presentation to T cells, potentially weakening immune responses (103). Sublethal hyperoxia has been shown to impair pulmonary innate immunity, increasing susceptibility to mortality from Gram-negative bacterial infections (104). Interestingly, in cancer research, hyperoxia has demonstrated a contrasting effect by enhancing antitumor immunity through multiple pathways, namely resulting in an immunopermissive tumor microenvironment that supports antitumor activity. Nevertheless, extended exposure to supplemental oxygen can trigger an excessive inflammatory response, potentially leading to organ damage, most notably in the lungs (105).

1.8. The immune system of newborns

The immune system of newborns follows a unique developmental trajectory, particularly in the lungs, where immune cells populate the tissue both before and after birth. This early colonization is crucial for establishing the first line of defense against pathogens and supporting the intricate processes required for proper lung development. Embryonic macrophages are among the first immune cells to populate the developing lung, where they contribute to vascularization and airway branching by releasing cytokines, proteoglycans, collagen, and growth factors. As fetal development advances to the canalicular phase (around E16.5 in mice), liver-derived fetal monocytes begin to outnumber both embryonic macrophages and DCs (106). The developing immune system also demonstrates remarkable plasticity, as inflammatory events in the fetal lung can accelerate the maturation and differentiation of monocytes even up until birth (107). Postnatally, the immune landscape of the lung changes substantially, in which fetal monocytes quickly differentiate into AMs, becoming the predominant immune cell type in the developing neonatal airways (108). While murine studies reveal dynamic shifts in DC subsets during development, current literature research suggests that the relative frequencies of DC subsets remain stable in human lungs throughout life (109). The development and maturation of lung immunity in newborns is shaped and influenced by a multitude of variables, nonetheless, early exposure to microbiota and microbial byproducts significantly guides the immune development of the lungs (110).

Preterm infants are born with underdeveloped immune systems characterized by deficiencies in both innate and adaptive immunity. These deficiencies are often exacerbated by complications associated with preterm birth. Compared to term infants, preterm infants have reduced numbers of monocytes, neutrophils, and their precursors due to lower levels of granulocyte colony-stimulating factor (G-CSF) and granulocyte-macrophage colony-stimulating factor (GM-CSF). Moreover, these cells exhibit impaired pathogen-killing abilities and reduced cytokine production, limiting T cell activation and expansion, as well as weakening defenses against bacterial infections and intracellular viruses (50). Preterm monocytes display impaired chemotaxis and phagocytosis during infections and reduced expression of co-stimulatory molecules such as major histocompatibility complex (MHC) II, CD40, CD80, and CD86, integral components for effective antigen presentation, adaptive

immune response, and T/B lymphocyte activation. Natural killer (NK) cells, which are critical for combating viral infections, are also phenotypically and functionally immature in preterm infants, resulting in lower production of IFN-γ and TNF-α, as well as reduced cytotoxic activity (111).

Alveolar macrophages are tissue-resident immune cells that line the inner epithelial surface of the alveoli. They play critical roles in lung development, and modulate intricate processes including surfactant homeostasis, immune surveillance, pathogen recognition, inflammation resolution, tissue repair, and maintaining overall lung homeostasis (112, 113). Alveolar macrophages are a vital component of the lung's innate immune defense against respiratory viruses and other pathogens, acting as a frontline defense by initiating innate immune responses upon exposure to pollutants or microbes (114, 115). Although AMs in preterm infants are immature at birth, they retain important functional capabilities. For example, studies have demonstrated that AMs from preterm neonates can mount a robust innate immune response to bacterial signals, like lipopolysaccharide (LPS). In preterm infants with BPD, AMs express heightened expression of inflammatory mediators in comparison with preterm infants without BPD (116). Inflammation is correlated with BPD, but not all immune cells contribute equally to impaired lung development. In hyperoxia-exposed lungs, neutrophils and exudate macrophages (ExAM) are recruited but do not drive arrested alveolarization. Instead, Csf1r-expressing monocyte/macrophage lineage cells are proven key mediators of this process. Furthermore, hyperoxia in the developing lungs leads to the loss of tissue-resident alveolar macrophages (TR-AM) and the emergence of a new macrophage population, likely formed by TR-AM transdifferentiation. These activated macrophages are implicated in disrupted alveolar development, supported by observations of macrophage phenotypic plasticity and increased MHC II expression in BPD-affected neonatal lungs (117).

1.9. A mouse model of RSV infection

The laboratory mouse (*Mus musculus*) is the most widely used animal model in biomedical research and is especially valued for studies in immunology, infectious diseases, and the evaluation of vaccines and therapeutic interventions worldwide (118). However, translating findings from mice to humans requires careful consideration of both the similarities and differences between the two species (119).

In a murine RSV infection model, mice serve as semi-permissive hosts. As a result, achieving efficient lung replication in the lungs to observe disease conditions requires inoculation with high viral doses. Low doses (10^3–10^5 PFU) generally cause airway inflammation without clinical illness, while higher doses (~10^7 PFU) are needed to induce weight loss and more severe lung pathology, though mice still do not fully reproduce an identical severe disease pathology as seen in humans (120). Among mouse strains, BALB/c mice are commonly used due to their intermediate susceptibility to RSV, displaying symptoms such as ruffled fur, reduced activity, weight loss, and moderate bronchiolitis following high-dose intranasal infection (121).

1.9.1. Pneumonia virus of mice

A more suitable model for studying RSV pathogenesis is the pneumonia virus of mice (PVM), a natural mouse pathogen from the same family as the human respiratory syncytial virus (hRSV). Pneumonia virus of mice provides a more accurate representation of the host-pathogen interactions seen in human RSV infections. Unlike hRSV, PVM efficiently replicates in mouse lung epithelial cells even with a minimal inoculum, leading to high viral titers in the lungs (over 10^8 PFU per gram of tissue). This efficient replication closely mimics the intense viral loads observed in severe RSV infections among preterm infants. Mice infected with PVM exhibit significant morbidity, including hunched posture, ruffled fur, rapid weight loss, and mortality. Airway hyperresponsiveness can persist long after viral clearance (122), paralleling the long-term respiratory complications observed after severe RSV infections in infancy (123). In neonatal mice, PVM infection presents differently than in older animals. Neonates show diminished inflammatory responses but exhibit failure to thrive, evidenced by poor weight gain, similar to virus-infected human newborns (124).

Immunoreactive PVM is predominantly localized to bronchiolar epithelial cells, mirroring human RSV infections. Histological analysis of infected mouse lungs reveals profound inflammation with extensive granulocyte (especially neutrophil) infiltration, severe pulmonary edema, and features consistent with acute respiratory distress syndrome (ARDS). This is accompanied by the production of proinflammatory mediators such as macrophage inflammatory protein (MIP)-1α, MIP-2, monocyte chemoattractant protein (MCP)-1, and interferon-γ (IFN-γ), closely resembling the

pathological and immunological responses observed in severe RSV cases in infants (125).

PVM was initially identified in 1939 by Frank Horsfall and Richard Hahn at Rockefeller University while investigating human pathogens that could replicate in the lung tissue of inbred mice (126). Unexpectedly, PVM was isolated from control mice presumed to be uninfected. Subsequent studies by Ginsberg and Horsfall established PVM as a valuable model for studying acute respiratory infections in mice (127). Pneumonia virus of mice belongs to the *Pneumoviridae* family, genus *Orthopneumovirus*, similarly to human and bovine respiratory syncytial viruses (128). Easton and colleagues have extensively characterized the PVM genome organization, revealing significant similarities to hRSV in gene structure and order (129, 130). They are enveloped viruses with single-stranded, nonsegmented, negative-sense RNA genomes, approximately 15 kb in length. The gene order and structure are highly conserved between the two viruses, except for the M2-L gene overlap, which is present in hRSV but absent in PVM (**Figure 2**) (131).

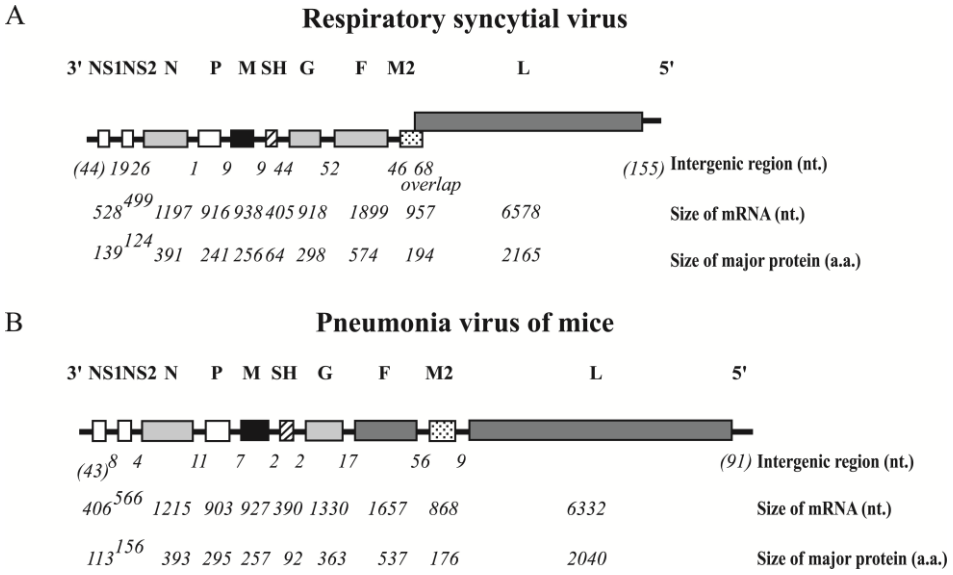

Figure 2. Genomic organization of (A) human respiratory syncytial virus (hRSV) and (B) pneumonia virus of mice (PVM) strain 15.

The figure illustrates the linear gene arrangement of both pneumoviruses from the 3' to 5' end of their negative-sense RNA genomes. Each gene is represented with three key measurements: the intergenic region size in nucleotides (nt, shown in parentheses above), the mRNA transcript size (nt, middle row), and the major protein size in amino acids (a.a., bottom row). Gene abbreviations include: NS1 and NS2, nonstructural proteins 1 and 2; N, nucleocapsid protein; P, phosphoprotein; M, matrix protein; SH, small hydrophobic protein; G, attachment glycoprotein; F, fusion protein; M2, second matrix protein; and L, large polymerase protein; nt., nucleotides; a.a., amino acids. Figure modified from (131).

Two primary strains of PVM are commonly studied: strain 15 and strain J3666. The original strain 15, studied by Horsfall's group, was initially highly pathogenic, yet over a period of time lost virulence after successive tissue-culture passage (132). In contrast, strain J3666 was developed at the Rockefeller University with minimal tissue-culture passage and remains highly pathogenic across most inbred mouse strains (133). Variants of strain 15 exhibit different pathogenic profiles depending on their source. For instance, PVM strain 15 Warwick from Dr Andrew Easton's laboratory is highly attenuated, inducing minimal inflammation (134). Conversely, PVM strain 15 ATCC is pathogenic in BALB/c mice but causes little to no disease in C57BL/6 mice. These noted genetic differences between strains J3666 and 15, particularly in the G and SH proteins, may account for varying virulence across strains (135-138).

Pneumonia virus of mice provides a robust platform for studying RSV pathogenesis due to its ability to replicate efficiently within murine lungs while inducing immune-mediated pathology that closely resembles severe RSV disease in humans. Its utility extends beyond understanding viral mechanisms to evaluating potential therapeutic strategies aimed at mitigating inflammation-driven lung injury, a critical focus for improving outcomes among preterm infants at high risk for severe RSV disease (132, 139).

2. Aims of the study

Preterm infants require supplemental oxygen therapy at birth, which contributes to stunted lung development. Affected infants, both as neonates and in early infancy, are at increased risk for severe respiratory viral infections compared to term-born infants with developed lungs, and they have a worse clinical outcome. Children with BPD, during their first year of life, have an estimated 12 times higher RSV hospitalization rate compared to children born at term with no underlying medical condition. Additionally, children with BPD face a substantially greater risk of requiring intensive care unit admission following RSV infection compared to those without BPD. However, the mechanisms by which oxygen therapy impairs lung development and the potential interplay between oxygen exposure and respiratory viral infection in the immature lung remain poorly characterized.

This project hypothesizes that *oxygen therapy-induced impairment of lung development in preterm infants significantly interacts with and increases susceptibility to respiratory viral infections.*

The main aims of this study were:

Aim 1:
To identify specific macrophage subpopulations that mediate the adverse effects of oxygen therapy on postnatal lung development, and to determine how these macrophage populations are influenced by respiratory viral infection.

Aim 2:
To characterize the transcriptomic mechanisms regulating the phenotypic plasticity of lung TR-AMs in oxygen-injured lungs, and to investigate the role of inflammatory cells in shaping the susceptibility of developing lungs to viral infection following oxygen exposure.

Aim 3:

To characterize cytokine/chemokine dynamics in oxygen-treated lungs with respiratory viral infection and evaluate the consequences of TR-AM depletion.

3. Materials and Methods

3.1. Materials

3.1.1. Equipment

The equipment used in the study is reported below in Table 1.

Table 1 - Equipment used in the study.

The name of the equipment, the manufacturer and the location, and the catalog number (#) used in the study. ##, no catalog number available.

Name	Company, Location	Catalog Number (#)
Flow cytometry		
BD FACSAria™ III	Becton Dickinson, USA	##
EASYstrainer 100 µm	Greiner Bio-One, Germany	542000
EASYstrainer 40 µm	Greiner Bio-One, Germany	542040
EASYstrainer 70 µm	Greiner Bio-One, Germany	542070
Falcon® 5 ml Round Bottom Polystyrene Test Tube	Corning Incorporated, USA	352054
Falcon® 5 ml Round Bottom Polystyrene Test Tube, with Cell Strainer Snap Cap	Corning Incorporated, USA	352235
LSR Fortessa	Becton Dickinson, USA	##
pluriStrainer® 40 µm	pluriSelect Life Science, Germany	43-50040-51
General equipment		
10 ml Stripette Serological Pipets	Corning Incorporated, USA	4488
24G x 0.5" Red Blunt Tip Dispensing Fill Needles	CML Supply, USA	901-24-050
25 ml Stripette Serological Pipets	Corning Incorporated, USA	4489
5 ml Stripette Serological Pipets	Corning Incorporated, USA	4487

Table 1 - continued

Name	Company, Location	Catalog Number (#)
BD Micro-Fine™ + Demi Insulin syringe	Becton Dickinson, USA	324826
BD Microlance 3 Needles 18 G	Becton Dickinson, USA	303262
BD Plastipak™ disposable syringe 5 ml	Becton Dickinson, USA	309649
Cell culture dish	Greiner Bio-One, Germany	664160
Cell culture multiwell plate, 6 well	Greiner Bio-One, Germany	657160
Cellstar® 15 ml tube	Greiner Bio-One, Germany	188261
Cellstar® 50 ml tube	Greiner Bio-One, Germany	227270
Centrifuge 5424 R	Eppendorf, Germany	5424 R
Combitips® advanced 1,0 ml	Eppendorf, Germany	0030089642
Combitips® advanced 10 ml	Eppendorf, Germany	0030089677
Combitips® advanced 2,5 ml	Eppendorf, Germany	0030089650
Combitips® advanced 25 ml	Eppendorf, Germany	0030089685
Combitips® advanced 5,0 ml	Eppendorf, Germany	0030089669
Combitips® advanced 50 ml	Eppendorf, Germany	0030089693
Cryo.s, 2 ml	Greiner Bio-One, Germany	1212XX
Cryostat	Leica, Germany	CM 1950
Delicate Suture Tying Forceps	FST, Germany	11063-07
Digital Slide Scanner	Hamamatsu Photonics, Japan	NanoZoomer-XR C12000
Easypet® 3 - Electronic Pipette Controller	Eppendorf, Germany	4430000018
Eppendorf Safe-Lock Tubes 0.5 ml	Eppendorf, Germany	0030121023
Eppendorf Safe-Lock Tubes 1.5 ml	Eppendorf, Germany	0030120086
Eppendorf Safe-Lock Tubes 2.0 ml	Eppendorf, Germany	0030120094
Eppendorf Tubes ® 5.0 ml	Eppendorf, Germany	0030119460
FastPrep-24™ 5G bead beating grinder and lysis system	MP Biomedicals, USA	116005500

Table 1 - continued

Name	Company, Location	Catalog Number (#)
Fine Scissors - ToughCut®	FST, Germany	14058-11
Heraeus Megafuge 16R Centrifuge	Thermo Fisher Scientific, USA	75004270
Laminar Flow Hood Typ 170	Laborbau Grittmann, Germany	##
Mechanical Pipette 0.5 – 10 µl	Eppendorf, Germany	3123000020
Mechanical Pipette 0.1 – 2.5 µl	Eppendorf, Germany	3123000012
Mechanical Pipette 10 – 100 µl	Eppendorf, Germany	3123000047
Mechanical Pipette 100 – 1,000 µl	Eppendorf, Germany	3123000063
Mechanical Pipette 2 – 20 µl	Eppendorf, Germany	3123000039
Mechanical Pipette 20 – 200 µl	Eppendorf, Germany	3123000055
Microtome	Leica, Germany	RM2255
Microtome Blades MX35 Ultra	Epredia, USA	3053835
Moria Iris Forceps	FST, Germany	11370-31
Moria Iris Forceps	FST, Germany	11373-12
Multipette® E3x	Eppendorf, Germany	4987000380
neoLab 3-1810 Mini Centrifuge Spectrifuge	neoLab Migge GmbH, Germany	55 01 31810
neoLabLine neoMag® magnetic stirrer without heating	neoLab Migge GmbH, Germany	D-6011
neoLabLine neoVortex® shaker	neoLab Migge, Germany	D-6012
Paraffin embedding station	Leica Biosystems, Germany	EG1150 H
PCR SingleCap 8 - SoftStrips 0.2 ml	Biozym Scientific, Germany	710988
Peel-A-Way™ embedding molds	Sigma-Aldrich, Germany	E6032-1CS
Precision Balance	Merck, Germany	Z742801-1EA
SARTORIUS CUBIS® semi-microbalance	Sartorius Lab Instruments GmbH & Co. KG, Germany	MSE225S-1CE-DU
Soft tissue homogenizing CK14-2 ml	Bertin Technologies, France	P000912-LYSK0-A

Table 1 – continued

Name	Company, Location	Catalog Number (#)
Spring Scissors	FST, Germany	15006-09
Superfrost™ Plus Adhesion Microscope Slides	Epredia, USA	J1800AMNZ
Surgical suture thread 4/0	Serag-Wiessner, Germany	IC158000
Tissue Section Bath	CellPath, United Kingdom	JAW-0100-00I
Transfer Pipettes	VWR International, Germany	612-6803
Vannas Spring Scissors	FST, Germany	15002-08
VeritiPro™ Thermal Cycler, 96-well	Thermo Fisher Scientific, USA	A48141
VWR® DRY-Line® Oven	VWR International, Germany	DL 53
Warm Plate	Medax, Germany	12895
Water bath for paraffin sections	Leica, Germany	HI1210
Quantitative polymerase chain reaction		
DeNovix DS-11 Series Spectrophotometer/Fluorometer	DeNovix Incorporated, USA	DS-11
QuantStudio™ 5 Real-Time PCR System	Thermo Fisher Scientific, USA	A28569
Hyperoxia-based model of bronchopulmonary dysplasia		
A-Chamber Animal Cage Enclosure	BioSpherix, USA	##
Oxygen Sensor	BioSpherix, USA	E-702
ProOx 110 Compact O_2 Controller	BioSpherix, USA	##
Whole body plethysmography		
Drierite Indicating Desiccant, 8 Mesh	Cole-Palmer, Germany	0719315

Table 1 – continued

Name	Company, Location	Catalog Number (#)
Plethysmograph chamber	Emka Technologies, France	##
usbAMP device	Emka Technologies, France	##

3.1.2. Reagents

The reagents used in the study are reported below in Table 2.

Table 2 - Reagents used in the study.

Name	Company, Location	Catalog Number (#)
Bulk RNA-seq		
RNase-Free DNase Set	Qiagen, USA	79254
RNeasy Plus Micro Kit	Qiagen, USA	74034
SMART-Seq® HT Kit	Takara Clontech, Japan	634455
Flow cytometry		
APC anti-mouse CD45 Antibody	BioLegend, USA	103112
BD FACSFlow™ Sheath Fluid	Becton Dickinson, USA	342003
BD Pharmingen™ Purified Rat Anti-Mouse CD16/CD32 (Mouse BD Fc Block™)	Becton Dickinson, USA	553142
Collagenase from Clostridium histolyticum	Sigma-Aldrich, Germany	C0130-500MG
DAPI	Sigma-Aldrich, Germany	D9542-1MG
FITC anti-mouse Ly-6G/Ly-6C (Gr-1) Antibody	BioLegend, USA	108406
PE anti-mouse CD11c Antibody	BioLegend, USA	117308

Table 2 - continued

Name	Company, Location	Catalog Number (#)
RPMI 1640 Medium	Thermo Fisher Scientific, USA	11875093
TruStain FcX™ PLUS (anti-mouse CD16/32) Antibody	BioLegend, USA	156604
Single-cell sequencing		
Chromium Next GEM Chip G Single Cell Kit	10X Genomics, USA	PN-1000127
Chromium Next GEM Single Cell 3' Kit v3.1	10X Genomics, USA	PN-1000269
Dual Index Kit TT Set A	10X Genomics, USA	PN-1000215
Real-time PCR		
dNTP Mix	Promega, USA	U1515
GeneAmp™ 10× PCR Buffer	Thermo Fisher Scientific, USA	N8080006
Invitrogen™ Nuclease-Free Water	Thermo Fisher Scientific, USA	10429224
Magnesium Chloride Solution, 25 mM	Promega, USA	A3511
M-MLV Reverse Transcriptase (200 U/µl)	Thermo Fisher Scientific, USA	28025021
peqGOLD Total RNA Kit	VWR, Germany	13-6834-02
Platinum™ SYBR™ Green qPCR SuperMix-UDG	Thermo Fisher Scientific, USA	11733046
Random Hexamers (50 µM)	Thermo Fisher Scientific, USA	N8080127
RNase Inhibitor	Thermo Fisher Scientific, USA	N8080119
RNaseZAP™	Sigma-Aldrich, Germany	R2020-250ML

Table 2 – continued

Name	Company, Location	Catalog Number (#)
General reagents		
Clodronate Liposomes & Control Liposomes (PBS)	Liposoma BV, Netherlands	CP-005-005
Eosin Y solution	Sigma-Aldrich, Germany	318906-500ML
Ethanol	ROTH, Germany	1HPH.1
Mayer's Hematoxylin Solution	Sigma-Aldrich, Germany	MHS1-100ML
Paraformaldehyde	Sigma-Aldrich, Germany	158127-500G
Phosphate-buffered saline	Sigma-Aldrich, Germany	P5493-1L
Tissue-Tek® O.C.T. Compound	Sakura Finetek Inc., USA	4583
Xylol	ROTH, Germany	9713.5

3.1.3. Software

The table (Table 3) below provides a list of the software used in this study.

Table 3 - Software used in the study.

Name	Company, Location
Adobe Illustrator	Adobe, USA
Datanalyst	Emka Technologies, France
Design & Analysis 1 (DA1) software	Thermo Fisher Scientific, USA
Design & Analysis 2 (DA2) software	Thermo Fisher Scientific, USA
FlowJo	Flow LLC, USA
GraphPad Prism 9.5.1	GraphPad, USA
ImageJ	NIH, USA
IOX2 software	Emka Technologies, France
Microsoft Office	Microsoft, USA
NDP.scan	Hamamatsu, Japan
NDP.view2	Hamamatsu, Japan
RStudio	Posit PBC, USA

3.2. Methods

3.2.1. Approval for animal experiments

All animal procedures were conducted according to protocols approved by the local regulatory authorities (*Regierungspräsidium Darmstadt*, Germany; approval number B2/2033, and *Regierungspräsidium Karlsruhe*, Germany; approval numbers G-55/22 and G-49/24) and complied with all relevant institutional and national guidelines for the care and use of laboratory animals.

3.2.2. C57BL/6J wild-type mice

C57BL/6J wild-type mice were bred in-house.

3.2.3. Hyperoxia-based model of bronchopulmonary dysplasia

Newborn mouse pups were randomized into equal-sized litters for each nursing dam. Pups assigned to the normoxic group (21% O_2) were housed in an IVC (Individually ventilated cage) system, while those in the hyperoxic group (85% O_2) were placed in an oxygen chamber (BioSpherix, Ltd., USA) from P1 to P14 to model BPD. Oxygen concentration in the chamber was regulated using a ProOx 110 controller (BioSpherix, Ltd., USA), with constant monitoring of O_2, humidity, and temperature. Nursing dams were rotated every 24 h between the IVC system and the oxygen chamber to mitigate oxygen toxicity in adult mice. All mice were maintained on a 12 h light-dark cycle with food provided *ad libitum*. Mouse pups were killed on postnatal days 4, 5, 7, 10, and 11 by intraperitoneal injection of either ketamine/xylazine (16 mg/kg) or pentobarbital sodium (Narkoren®, 500 mg/kg). All procedures complied with institutional animal care guidelines and approved protocols for humanely terminating experimental animals.

3.2.4. Preparation of pneumonia virus of mice (PVM) strain J3666 viral stocks

The viral stocks of PVM strain J3666 were made using 8-12 week-old BALB/c mice, considered the most permissive strain for this virus. The fully pathogenic PVM strain J3666 was originally acquired from Dr A. J. Easton (University of Warwick, Coventry, UK), with the virus stocks tracing back to the Rockefeller University. Virulence was maintained through serial passage in mice. An aliquot of the virus stock was thawed, briefly centrifuged, and diluted 1:50 in Roswell Park Memorial Institute (RPMI) 1640 medium to ensure a high viral load. Mice were anesthetized using 2-4% isoflurane inhalation. While in a reverse-Trendelenburg position, each mouse received an 80 µl intranasal inoculation using an 18G Surflo® intravenous catheter to ensure consistent droplet formation. Inoculated mice were monitored daily using a modified Cook score (140, 141). This clinical scoring system ranged from 1 (healthy) to 6 (death), with intermediate scores reflecting increasing severity of symptoms such as ruffled fur, hunched posture, lethargy, and abnormal breathing patterns. Peak disease was anticipated at 4-5 days post-inoculation in BALB/c mice. At the peak of infection, mice were euthanized, and the lungs were harvested. Each lung was homogenized in 1 ml of RPMI medium on ice. The homogenates were centrifuged at 13,000 rpm for 5 min at 4 °C. Supernatants from all mice were pooled, aliquoted into 50 µl volumes in

cryogenic vials, rapidly frozen, and stored in liquid nitrogen at -180 °C. This method ensures the production of high-titer, pathogenic PVM stocks for subsequent experimental use, maintaining the virulence of the J3666 strain through *in vivo* passage.

3.2.5. RT-PCR quantification of viral stock J3666

Total RNA was isolated from 49 µl of viral stock supernatant using the peqGOLD Total RNA Kit (VWR) following the manufacturer's standard protocol. The final RNA was eluted in 100 µl of nuclease-free water, yielding a concentration of 49.12 ng/µl. For cDNA production, 18.3 µl of the isolated RNA (900 ng total) was combined with 1.7 µl nuclease-free water to a total volume of 20 µl. The RNA was denatured, followed by reverse transcription using Moloney Murine Leukemia Virus Reverse Transcriptase (M-MLV reverse transcriptase) in a 20 µl reaction. The resulting cDNA was then diluted with 60 µl nuclease-free water to a final volume of 100 µl. Quantitative real-time RT-PCR was performed using 2 µl of the synthesized cDNA. The reaction was carried out using a standard curve for absolute quantification (provided by our collaborator Reinout A. Bem). The mean quantity interpolated from the standard curve was 332,972 copies. A stock solution with a concentration of 7×10^{10} copies SH/µl was used as the starting material. Six standard dilutions were prepared in 2 ml tubes, ranging from 5×10^{8} (highest) to 5×10^{3} (lowest) viral copies. In each well, 23 µl of master mix was combined with 2 µl of the appropriate standard. For the highest concentration standard, this resulted in $(0.5 \times 10^{9}) \times 2 = 1 \times 10^{9}$ copies in 25 µl total volume, with a final concentration of 4×10^{7} copies/µl in the total reaction mixture. Sample quantification was calculated as follows:

Ct sample compared to standard curve = (x copies in 2 µl cDNA) / 2 = x copies / µl sample.

The final concentration of the viral stock J3666 was determined to be 1.86×10^{6} copies/µl or 1.86×10^{9} copies/ml.

3.3. Intranasal infection of the neonatal mice with the pneumonia virus of mice

C57BL/6J mice were exposed to either normoxic (21% O_2) or hyperoxic (85% O_2) conditions from birth. On P4, animals were intranasally inoculated with PVM. The viral stock was thawed and diluted in RPMI medium to achieve the desired concentration.

Each mouse received a 10 µl inoculum of the virus suspension, administered to the nostrils using a mechanical pipette equipped with 10 µl pipette tips. For the control condition, mice were intranasally treated with RPMI medium alone, which served as the diluent for the virus stock. Due to the small size and limited mobility of the 4-day-old neonates, anesthesia was not required for the inoculation procedure. This intranasal inoculation method was chosen to mimic the natural route of respiratory virus transmission and to ensure a more homogeneous distribution of the virus in the upper and lower respiratory tract than intratracheal instillation. Survival of mice was monitored daily post-inoculation. The time from inoculation to death or censoring was recorded for each animal. The survival curve includes mice that were found dead as well as those that were cannibalized within the cages. In accordance with animal ethics guidelines, mice showing signs of severe distress or poor condition were euthanized upon reaching the score threshold to minimize suffering.

3.4. Clodronate liposome treatment of newborn mice

For selective depletion of alveolar macrophages, clodronate-encapsulated liposomes were employed. These artificial spheres consist of concentric phospholipid bilayers encapsulating an aqueous phosphate-buffered saline (PBS) solution containing clodronate. The liposomal particles have a maximum diameter of 3 µm, with a clodronate concentration of approximately 5 mg/ml in the suspension. For intranasal administration (IN), 10 µl of the liposome suspension was administered on postnatal days 3, 6, 9, and 12. Alternatively, intraperitoneal administration (IP) was performed using clodronate liposomes diluted 1:1 with PBS, with a dosing volume of 10 µl per gram of body weight administered at the same time points. This regimen was designed to ensure consistent depletion of alveolar macrophages throughout the critical period of lung development.

3.5. Isolation of the lungs and embedding in paraffin

Following euthanasia, a midsternal thoracotomy was performed to expose the thoracic cavity and provide access to the trachea. The trachea was cannulated using a blunt-tipped needle, and the lungs were fixed by instilling 4% (m/v) paraformaldehyde (PFA) solution under a constant hydrostatic pressure of 20 cm H_2O. This pressure-controlled fixation ensures uniform inflation and preservation of alveolar architecture. After fixation, the lungs were carefully excised and immersed in 4% PFA

at 4 °C for 24 h to ensure complete fixation. The mouse lungs were meticulously dissected to remove residual thymus, heart, and blood clots. The cleaned lung specimens were transferred to labeled tissue cassettes. Tissue processing was performed using a series of graded ethanol baths (70%, 80%, 95%, and 100%) for dehydration, followed by xylene as a clearing agent. The processed lung tissue was then embedded in molten paraffin wax (56–58 °C) using a tissue embedding station. The embedded specimens were rapidly cooled on a cold plate to ensure optimal tissue orientation and block formation. Finally, the resulting paraffin blocks were stored at 4 °C until further use for sectioning and histological analysis.

3.6. Paraffin sectioning

Paraffin-embedded lung tissue blocks were sectioned using a fully automated rotary microtome equipped with disposable Feather microtome blades. Serial sections of 5 µm thickness were obtained and carefully transferred onto Superfrost Plus adhesion microscope slides. To ensure optimal tissue adherence, the slides were placed on a heating plate and dried overnight at 40 °C.

3.7. Lung histology

For staining, slides were deparaffinized in xylene and rehydrated through a graded series of ethanol solutions before being rinsed in distilled water. The sections were then stained with Mayer’s hematoxylin (Sigma-Aldrich, #MHS1-100ML) for 8 min, washed in running tap water for 10 min, and briefly rinsed in distilled water. Counterstaining was performed using eosin Y solution (Sigma-Aldrich, #318906-500ML) for 30 s to 1 min. After staining, the slides were dehydrated in graded alcohols, cleared in xylene, and coverslipped using a resinous mounting medium. The stained slides were scanned using a Hamamatsu NanoZoomer digital slide scanner to assess lung structure.

3.8. Total RNA isolation

Mouse lungs, hearts, livers, and kidneys were homogenized using Precellys tubes (Precellys, Bertin, USA, #P000912-LYSK0-A) and the FastPrep-24™ 5G bead beating grinder and lysis system (MP Biomedicals, Irvine, CA, USA, #116005500). Following the manufacturer's protocol, total RNA was isolated from the homogenized tissues

using the PeqGOLD Total RNA Kit. The extracted RNA was then resuspended in 30 µl of nuclease-free water.

3.9. Complementary DNA synthesis

The concentration and purity of the total RNA were measured using a DeNovix Spectrophotometer. For cDNA synthesis, 750 ng of total RNA from each sample (diluted in nuclease-free water) was reverse transcribed using M-MLV reverse transcriptase and random hexamer oligodeoxyribonucleotides. Initially, 20 µl of RNA was denatured at 70 °C for 10 min, followed by the addition of 20 µl of the reverse transcription mixture as described in Table 4. The reaction was then incubated at 21 °C for 10 min, followed by cDNA synthesis at 43 °C for 1 h and 15 min. Finally, M-MLV reverse transcriptase was inactivated by heating the mixture at 95 °C for 5 min, as detailed in Table 5. After reverse transcription, the cDNA was diluted to a final volume of 60 µl with nuclease-free water.

Table 4 - Components of reverse transcription mixture

Component	Volume in µl for one reaction
Nuclease-free water	2.5
GeneAmp™ 10X PCR Buffer	4
dNTP Mix (10 mM)	2
Random hexamers (50 µM)	2
Magnesium chloride (25 mM)	8
RNAse inhibitor (20 U/µl)	1
Reverse transcriptase (200 U/µl)	0.5
Total volume	20

Table 5 - The reverse transcription reaction steps, including the corresponding temperatures and durations

Reaction	Temperature (°C)	Time (min)
Denaturation	21	10
Extension	43	75
Enzyme Inactivation	95	5
Storage	4	∞

3.10. Quantitative polymerase chain reaction

Quantitative polymerase chain reaction (qPCR) was conducted to analyze changes in gene expression using the QuantStudio™ 5 Real-Time PCR System (Thermo Fisher Scientific, USA, #A28569). The reaction master mix for qPCR was prepared according to the reagent volumes listed in Table 6. Amplification and detection of target sequences were performed with Platinum™ SYBR™ Green qPCR SuperMix-UDG as the fluorescent reporter. The thermal cycling conditions for all qPCR reactions are provided in Table 7. Relative gene expression was determined using the comparative CT (threshold cycle) method for qPCR analysis. The ΔCT values were calculated by subtracting the CT of the reference gene from the CT of the gene of interest, as per the following equation:

ΔCT = CT (reference gene) - CT (gene of interest)

This study employed the RNA polymerase II subunit A (*Polr2a*) gene as an endogenous control for mRNA normalization, owing to stable expression across various experimental conditions. Primer pairs specific to the target mRNA sequences were sourced from previously published studies, the online PrimerBank database (https://pga.mgh.harvard.edu/primerbank/), or designed using the Primer-BLAST software (http://www.ncbi.nlm.nih.gov/tools/primer-blast/). The complete list of primers, including their forward and reverse sequences, is provided in Table 8. Oligonucleotide primers for both target and reference genes were custom-synthesized by Eurofins Scientific to ensure high specificity and efficiency in the amplification of the desired mRNA transcripts.

Table 6 - Master mix used for real-time PCR reaction

Reagent	Volume in µl for one reaction
Nuclease-free water	8
Magnesium chloride	1
Primer mix (forward and reverse; 10 mM each)	1
Platinum™ SYBR™ Green qPCR SuperMix-UDG	13
cDNA	2
Total volume	25

Table 7 - Real-time PCR thermal cycling protocol

		Temperature (°C)	Time
Denaturation		95	5 min
Denaturation	40×	95	5 s
Annealing		59	5 s
Extension		72	30 s
Final Extension		72	5 min
Melting Curve Analysis			30 min
Storage		4	∞

3.11. PVM-SH gene as a target for viral infection with PVM

The small hydrophobic gene of PVM is an effective target for viral detection using real-time PCR due to several key characteristics. First, the SH gene sequence is unique to PVM, which ensures high specificity and enables precise detection and quantification of the virus. Additionally, this gene is well-conserved among different PVM strains, making it a reliable target for detection across various viral isolates. Real-time PCR assays that target the SH gene are highly sensitive and capable of detecting even low levels of viral RNA, allowing for accurate measurement of viral load. Furthermore, the use of the SH gene in these assays facilitates precise

quantification of viral replication, which is crucial for studying virus kinetics and evaluating the efficacy of antiviral treatments (125).

Table 8 - List of primers for real-time PCR

Gene	Forward (5′-3′)	Reverse (5′-3′)
Ccl2	TTAAAAACCTGGATCGGAACCAA	GCATTAGCTTCAGATTTACGGGT
Ccl5	GCTGCTTTGCCTACCTCTCC	TCGAGTGACAAACACGACTGC
CxCl10	CCAAGTGCTGCCGTCATTTTC	GGCTCGCAGGGATGATTTCAA
Ear1	CATGCCTGGGTCAAACCCC	ATTTGTTGCCCGACTGGTGAT
Ccl3	GAAGGATACAAGCAGCAGCG	TTCTCTTAGTCAGGAAAATGACACC
Polr2a	CTAAGGGGCAGCCAAAGAAAC	CCATTCAGCATACAACTCTAGGC
PVM SH	GCCGTCATCAACACAGTGTGT	GCCTGATGTGGCAGTGCTT

3.12. Flow cytometry

Lung tissue from neonatal mice exposed to either normoxic (21% O_2) or hyperoxic (85% O_2) conditions was harvested for flow cytometric analysis. To generate single-cell suspensions, each lung specimen was first mechanically minced into small fragments using sterile surgical scissors and then subjected to enzymatic digestion with a solution containing 0.01% Collagenase (Sigma Aldrich, Germany, #C0130-500MG) in RPMI 1640 medium (Gibco, Germany, #21875034). Digestion was performed under gentle agitation for 20 min at 37 °C. The resulting single-cell suspensions were filtered sequentially through 70 µm and 40 µm cell strainers to remove debris and aggregates, then centrifuged at 1400 rpm for 5 min at 4 °C. The cell pellets were washed with DMEM supplemented with 5% FBS and 1% penicillin/streptomycin to eliminate residual enzymes and support cell viability. Prior to antibody staining, cells were resuspended in BD FACSFlow™ Sheath Fluid to provide optimal conditions for flow cytometric analysis. For immunophenotyping, the cells were incubated with a panel of fluorophore-conjugated antibodies for 20 min at 4 °C under gentle agitation, a protocol designed to minimize non-specific binding and ensure efficient antibody-antigen interactions. Just before acquisition, 4′,6-diamidino-2-phenylindole (DAPI) was added as a viability dye to distinguish live from dead cells, thereby improving the accuracy of downstream analyses by excluding non-viable cells. Pulmonary leukocyte populations were analyzed using a hierarchical,

multiparameter gating strategy. Initially, CD45 was used as a pan-leukocyte marker to identify all immune cells within the lung single-cell suspension. Within the $CD45^+$ population, Ly6G served as an exclusion marker to remove neutrophils from further analysis. TR-AMs were then identified based on dual expression of CD11c and Siglec-F, while ExAMs were distinguished by their $CD11b^+$ $MHCII^-$ phenotype within the remaining myeloid compartment. For lymphoid analysis, T cells were identified within the $CD45^+$ population by CD3 expression, with further subset discrimination using CD4 and CD8 to distinguish helper and cytotoxic T cell populations, respectively. The γδ T cells were identified by TCR γ/δ expression within the $CD3^+$ gate. B cells were identified by CD20 expression within the $CD3^-$ lymphoid population. This comprehensive gating approach enabled precise discrimination between TR-AMs, recruited ExAMs, and distinct T and B cell subsets, facilitating quantitative assessment of these immune populations under different experimental conditions.

Table 9 - Antibodies used for flow cytometry analysis

Antibody	Manufacturer	Catalog number
APC anti-mouse I-A/I-E	BioLegend, USA	107614
APC Anti-mouse TCR γ/δ	BioLegend, USA	118116
APC/Cyanine7 anti-mouse CD3	BioLegend, USA	100222
Brilliant Violet 510™ anti-mouse CD11b	BioLegend, USA	101263
Brilliant Violet™ 605 anti-mouse CD20	BioLegend, USA	150435
FITC anti-mouse CD45	BioLegend, USA	103108
PE anti-mouse CD170 (Siglec-F)	BioLegend, USA	155506
PE anti-mouse CD8a	BioLegend, USA	100708
PE/Cyanine7 anti-mouse CD11c	BioLegend, USA	117318
PE/Cyanine7 anti-mouse CD4	BioLegend, USA	100422
PerCP/Cyanine5.5 anti-mouse Ly-6G	BioLegend, USA	127616

3.13. Respiratory function assessment via whole-body plethysmography

Whole-body plethysmography was performed on neonatal mice at P11 using a system from emka Technologies (France), with plethysmograph chambers equipped with custom inserts specifically designed for neonatal mice. Before each measurement session, the plethysmograph was calibrated to ensure accuracy. For each animal, the procedure consisted of a 2-min acclimation period followed by an 18-min recording period. Mice were placed individually in the chambers, and respiratory parameters were recorded using IOX2 acquisition software and subsequently analyzed with DataAnalyst software (both from emka Technologies, France). This non-invasive approach enabled the assessment of respiratory function in unrestrained neonatal mice, providing valuable insights into breathing patterns and potential respiratory abnormalities during early postnatal development.

3.14. Fluorescence-Activated Cell Sorting of immune cells

Lung tissue was harvested from P10 mice exposed to either normoxia (21% O_2) or hyperoxia (85% O_2). Single-cell suspensions were prepared using standard mechanical and enzymatic dissociation techniques. The resulting cells were stained with fluorochrome-conjugated antibodies against CD45, CD11c, and Gr-1. For flow cytometric analysis, a hierarchical gating strategy was employed to identify pulmonary leukocyte populations while excluding neutrophils. Initially, cells were gated on CD45 positivity to isolate all leukocytes, after which Gr-1 high cells, corresponding to neutrophils, were excluded from the analysis. The remaining $CD45^{+}Gr\text{-}1^{-}$ population was then assessed for CD11c expression to identify specific myeloid cell subsets, such as alveolar macrophages and dendritic cells. Flow cytometric acquisition was performed on a BD FACSAria™ cytometer, and data were analyzed using BD FACSDiva software.

3.15. Bulk RNA-seq

Following fluorescence-activated cell sorting (FACS) of 1×10^{5} immune cells ($CD45^{+}$ $Gr\text{-}1^{-}$ $CD11c^{+}$), total RNA was isolated using the RNeasy Plus Micro Kit (Qiagen, USA, #74034). To eliminate potential genomic DNA contamination, samples were treated with DNase using the RNase-Free DNase Set (Qiagen, USA). RNA integrity and library quality were assessed using the LabChip Gx Touch 24 (Perkin Elmer, USA). For library preparation, 300 pg of total RNA was used as input for the

SMART-Seq HT Kit (Takara Bio, Japan). Sequencing was performed on the Illumina NextSeq 500 platform using v2 chemistry, generating an average of 20 million single-end reads per library (1×75 bp). Raw read quality was evaluated with FastQC, and only reads between 30 and 150 nucleotides in length were retained for downstream analysis. Reads were aligned to the Ensembl mouse genome (version mm10, GRCm38) using STAR 2.6.1d, with a maximum mismatch ratio of 10% (outFilterMismatchNoverLmax 0.1). Gene-level quantification was conducted with featureCounts 1.6.3 from the Subread package, counting only exon-mapped reads and excluding multi-mapping reads. For differential expression analysis, genes exhibiting a minimum fold change of ±1.5 (log_2FC ±0.585) and a maximum Benjamini-Hochberg corrected p-value of 0.05 were considered significant. Ensembl gene annotations were supplemented with information from the UniProt database (release 06.06.2014) based on Ensembl gene identifiers.

3.16. Single-cell RNA sequencing

Single-cell RNA sequencing was performed on sorted cells using the Chromium Next GEM Single Cell 3' v3.1 kit (10x Genomics). For each sample, cells were loaded separately into individual lanes of the Chromium Controller, and gene expression libraries were prepared according to the manufacturer's protocol. This workflow involves the generation of Gel Beads-in-emulsion (GEMs) by combining a master mix containing cells and enzymes with 10x barcoded gel beads and partitioning oil. Within each GEM, mRNA from individual cells is uniquely barcoded, reverse transcribed, and amplified. The resulting cDNA from all cells was then pooled for library construction and subsequent sequencing.

3.17. Protein differences in mouse lung tissue samples

Proteins were extracted from samples using scioExtract buffer (Sciomics) following the manufacturer's standard operating procedures. Total protein concentrations were determined with a BCA assay. To generate a reference, equal volumes from each sample were pooled. Individual samples were adjusted to a uniform protein concentration and labeled for 2 h with scioDye 2 (Sciomics), while the reference pool was labeled with scioDye 1 (Sciomics). Labeling reactions were terminated after 2 h, followed by buffer exchange to PBS. All labeled proteins were stored at –20 °C until further analysis. A total of thirty samples were analyzed using a dual-color,

reference-based design on scioCD antibody microarrays (Sciomics), each targeting a range of CD surface markers and cytokines/chemokines, with four technical replicates per antibody. Arrays were blocked with scioBlock (Sciomics) on a Hybstation 4800 (Tecan, Austria). Subsequently, each sample and the reference were co-incubated on the arrays for three hours. After incubation, arrays were washed with 1× PBSTT, rinsed with 0.1× PBS and water, and dried with nitrogen. Slides were scanned using a Powerscanner (Tecan, Austria) with constant laser power and photomultiplier tube (PMT) settings. Spot segmentation was performed using GenePix Pro 6.0 (Molecular Devices, USA). Median signal intensities were analyzed with the linear models for microarray data (LIMMA) package in R-Bioconductor following upload of the raw data. Data normalization was performed using an invariant Lowess method optimized for this assay.

3.18. SHG imaging and sample preparation

Neonatal mice were exposed to normoxia (21% O_2) or hyperoxia (85% O_2) and intranasally infected with PVM on P4. Control mice received intranasal RPMI medium. On P11, mice were euthanized, and lungs were perfused with PBS via the right ventricle to clear circulating blood. The trachea was cannulated, and lungs were inflated with a 1:1 mixture of 8% PFA and Tissue-Tek® O.C.T.™ Compound (Science Services GmbH, Germany, #4583). After 10 min of fixation, lungs were excised, placed in Peel-A-Way™ embedding molds (Sigma-Aldrich, Germany, #E6032-1CS), and snap frozen on dry ice. Frozen lungs were sectioned at 20 µm thickness using a cryostat, and three consecutive sections were mounted on each Superfrost Plus slide. Slides were stored at –80 °C until imaging. The slides were scanned using a Zeiss NLO LSM780 microscope equipped with a pulsed multiphoton laser. Two-photon excited signals were captured in three separate channels: forwards SHG, backwards SHG, and two-photon excited autofluorescence (2PEA). The forwards SHG signal was detected using a laser blocking filter and a 436/20 nm bandpass filter, while the backwards SHG signal was recorded with internal detectors in a bandwidth of 435-455 nm. The 2PEA signal was collected in a bandwidth of 550-650 nm.

3.19. SHG image analysis

Image analysis of z-stacks, comprising both forwards and backwards SHG channels as well as 2PEA, was performed using a semi-automated pipeline in Fiji (ImageJ),

implemented as a Jython script (142). For each lung tissue section mounted on Superfrost Plus slides, all channels were thresholded, and the area or number of pixels below the threshold (PBT) was quantified for each channel. The integrated intensity of the PBT (Sumintensity) was also calculated per channel. To assess total fibrillar collagen content, the Sumintensity values from the forwards and backwards SHG channels were summed, providing a measure of overall fibrillar collagen. For spatial analysis, a maximum intensity projection was generated by summing the two-dimensional forwards and backwards SHG images. This composite image was subdivided into an 8×8 grid of equally sized regions of interest (ROIs). Each ROI was manually classified as representing either interstitial collagen or non-interstitial regions. Only ROIs identified as interstitial collagen were included in the averaging for each SHG image. For normalization, the Sumintensity of total collagen content (expressed as pixels·ROI^{-1}) was normalized to the mean SHG signal measured in unstimulated (control) lung sections from the same experimental group. A minimum of 20 ROIs were analyzed per SHG z-stack to ensure robust quantification.

4. Results

4.1. Survival outcomes in neonatal mice exposed to normoxia or hyperoxia and infected with PVM

Survival outcomes were assessed in neonatal mice exposed to either normoxia (21% O_2) or hyperoxia (85% O_2) and intranasally infected with PVM at dilutions of 1:1,000, 1:2,500, or 1:5,000 in RPMI medium on P4. Control groups were treated intranasally with RPMI medium alone. Hyperoxia-exposed mice infected with PVM at a dilution of 1:1,000 exhibited 100% mortality by P12. In contrast, the normoxia control group, the normoxia-infected group, and the hyperoxia control group demonstrated 100% survival throughout the observation period (**Figure 3A**). In hyperoxia-exposed mice, PVM infection at 1:2,500 and 1:5,000 dilutions resulted in dose-dependent reductions in survival, with intermediate mortality at 1:2,500 and less severe, but still notable, mortality at 1:5,000 compared to controls. Normoxia-infected mice at 1:2,500 dilution experienced no mortality until P23, when survival decreased to 80%, while normoxia-infected mice at 1:5,000 dilution experienced no mortality (**Figure 3B**). These results demonstrate that hyperoxia exposure, concomitantly with PVM infection, significantly exacerbated PVM-induced lethality in a dose-dependent manner, while normoxic conditions provide substantial protection against mortality.

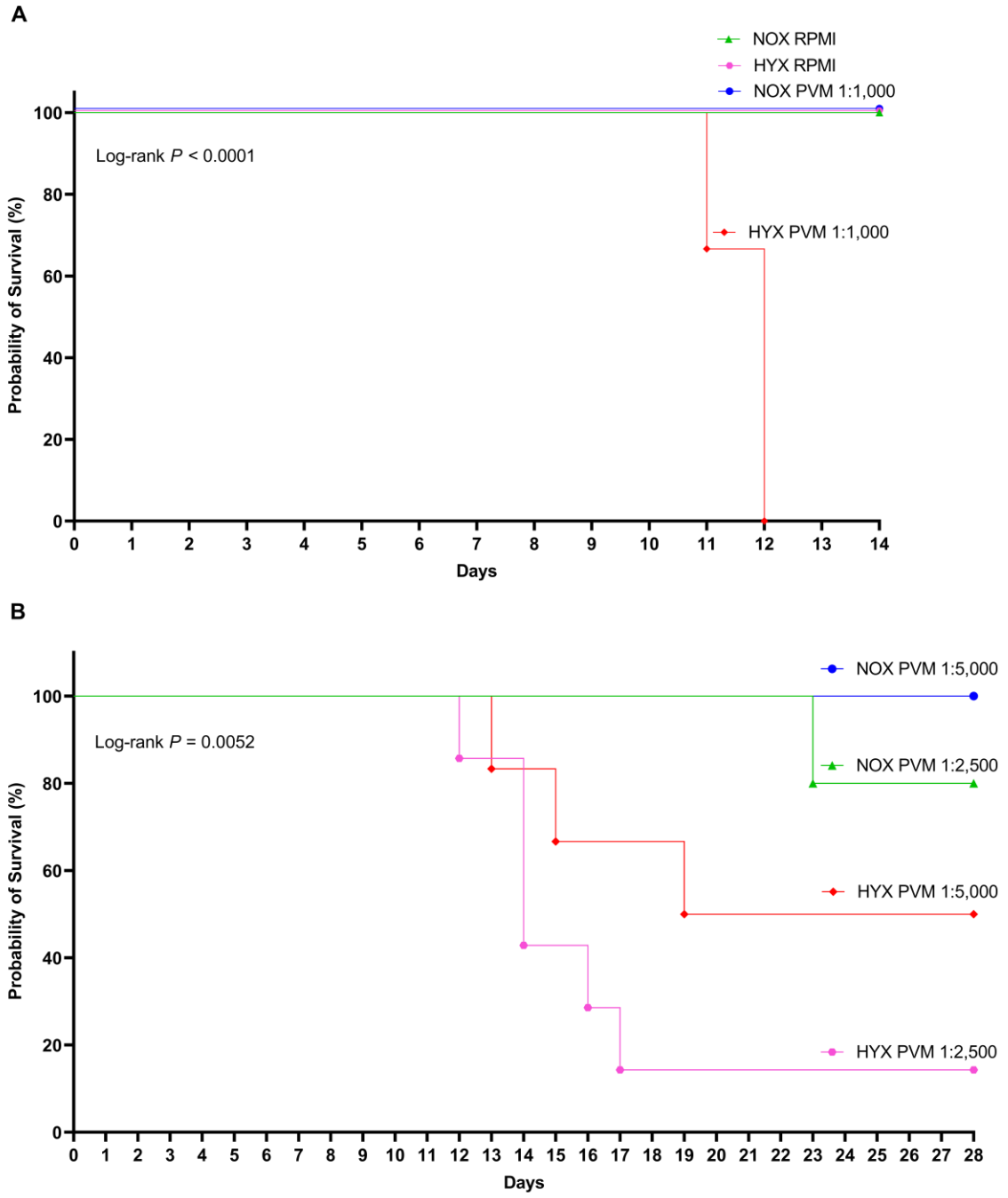

Figure 3. Probability of survival of neonatal mice exposed to normoxia or hyperoxia and infected with PVM.

Kaplan–Meier survival curves of neonatal mice exposed from birth to normoxia (NOX; 21% O_2) or hyperoxia (HYX; 85% O_2) and infected intranasally on postnatal day (P)4 with pneumonia virus of mice (PVM) at different dilutions (1:1,000, 1:2,500, or 1:5,000) in RPMI medium. Control groups received RPMI alone. (A) Survival of mice infected with PVM at 1:1,000 dilution. (B) Survival of mice infected with PVM at 1:2,500 or 1:5,000 dilution. Each line represents an experimental group (n=5-9, per group). The statistical analysis was performed using the Mantel–Cox (log-rank) test to compare survival across all four experimental groups.

4.2. Histological analysis of lung tissue following normoxia or hyperoxia exposure and PVM infection in neonatal mice

Neonatal mouse pups were assigned to either normoxia (21% O_2) or hyperoxia (85% O_2) conditions from birth and intranasally infected with PVM at dilutions of 1:1,000, 1:2,500, or 1:5,000 in RPMI medium on P4. Control groups were treated intranasally with RPMI medium alone. Lungs were collected on P11, fixed, paraffin-embedded, and stained with hematoxylin and eosin (H&E) for histological evaluation. Lung histology revealed that all the groups exposed to hyperoxia (85% O_2), regardless of PVM infection, exhibited marked alveolar simplification, characterized by enlarged alveolar spaces and reduced septation, indicative of impaired lung development. Amongst hyperoxia-exposed groups, mice infected with PVM at the 1:1,000 dilution exhibited more pronounced inflammatory changes, including increased cellular infiltration, compared to both hyperoxia controls and hyperoxia groups infected with higher PVM dilutions (**Figure 4A**). This suggests that PVM infection at the highest viral load exacerbates lung inflammation under hyperoxic conditions. In contrast, all normoxia control and normoxia-infected groups maintained normal alveolar architecture with no significant evidence of inflammation or structural abnormalities (**Figure 4A-B**). These findings indicate that while hyperoxia alone disrupts normal lung development, the combination of hyperoxia and high-dose PVM infection leads to a distinct and synergistic increase in pulmonary inflammation in neonatal mice.

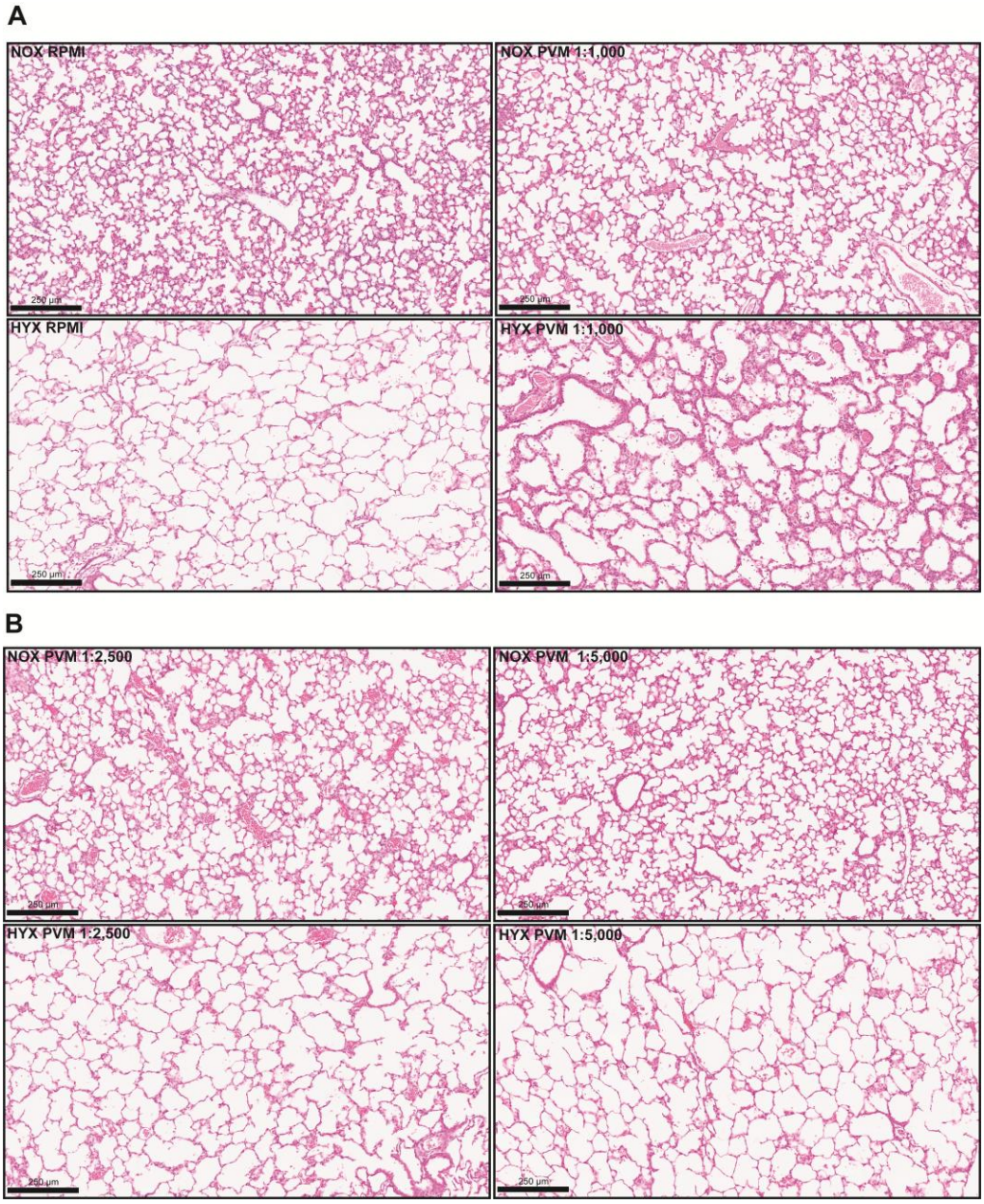

Figure 4. Histological analysis of lung tissue in normoxia- and hyperoxia-exposed mice infected with PVM.

Representative hematoxylin and eosin (H&E)-stained lung sections from neonatal mouse pups exposed to (NOX; 21% O_2) or hyperoxia (HYX; 85% O_2) from birth. On postnatal day (P)4, pups in each group received an intranasal administration of either pneumonia virus of mice (PVM) diluted (A) 1:1,000, (B) 1:2,500, and 1:5,000 in RPMI medium or RPMI medium alone as a control. Lungs were harvested on P11, paraffin-embedded, sectioned, stained with H&E, and scanned. Images were acquired at 10× magnification.

4.3. Impact of hyperoxia and PVM Infection on respiratory physiology in neonatal mice

Neonatal mouse pups were assigned to either normoxia (21% O_2) or hyperoxia (85% O_2) from birth. On P4, pups in each group received intranasal administration of RPMI medium (control) or PVM at dilutions of 1:1,000 or 1:5,000. Lung function was assessed at P11 using whole-body plethysmography. Hyperoxia exposure and PVM infection had significant, and in many cases synergistic, negative effects on lung function in neonatal mice. Normoxic controls exhibited the highest tidal volume (TV), expiratory volume (EV), and minute volume (MV), while PVM infection led to a dose-dependent reduction in these parameters, with the largest decrease observed at the higher viral titer. Hyperoxia alone resulted in an even greater decrease in tidal and expiratory volumes compared to normoxic controls, confirming the harmful effects of high oxygen exposure on lung development. The most pronounced impairments were observed in hyperoxia-exposed, PVM-infected pups, whose TV, EV, and MV were at their lowest across all groups, underscoring a synergistic detrimental effect when neonatal animals experienced both oxygen toxicity and viral infection (**Figure 5A-C**). Breathing frequency was the highest in the NOX RPMI controls and remained relatively elevated in the normoxic PVM groups, but was significantly reduced in all hyperoxia-exposed groups, especially in those also infected with PVM (**Figure 5D**). Inspiratory time and expiratory time revealed marked disturbances in respiratory rhythm across experimental groups, and both parameters were prolonged in hyperoxic pups, with maximal increases seen in those also infected with the virus (**Figure 5E-F**). These results demonstrate that perinatal hyperoxia and PVM infection, both alone and synergistically, substantially disrupt respiratory function in neonatal mice, highlighting the heightened vulnerability of immature lungs to combined oxygen toxicity and viral infection.

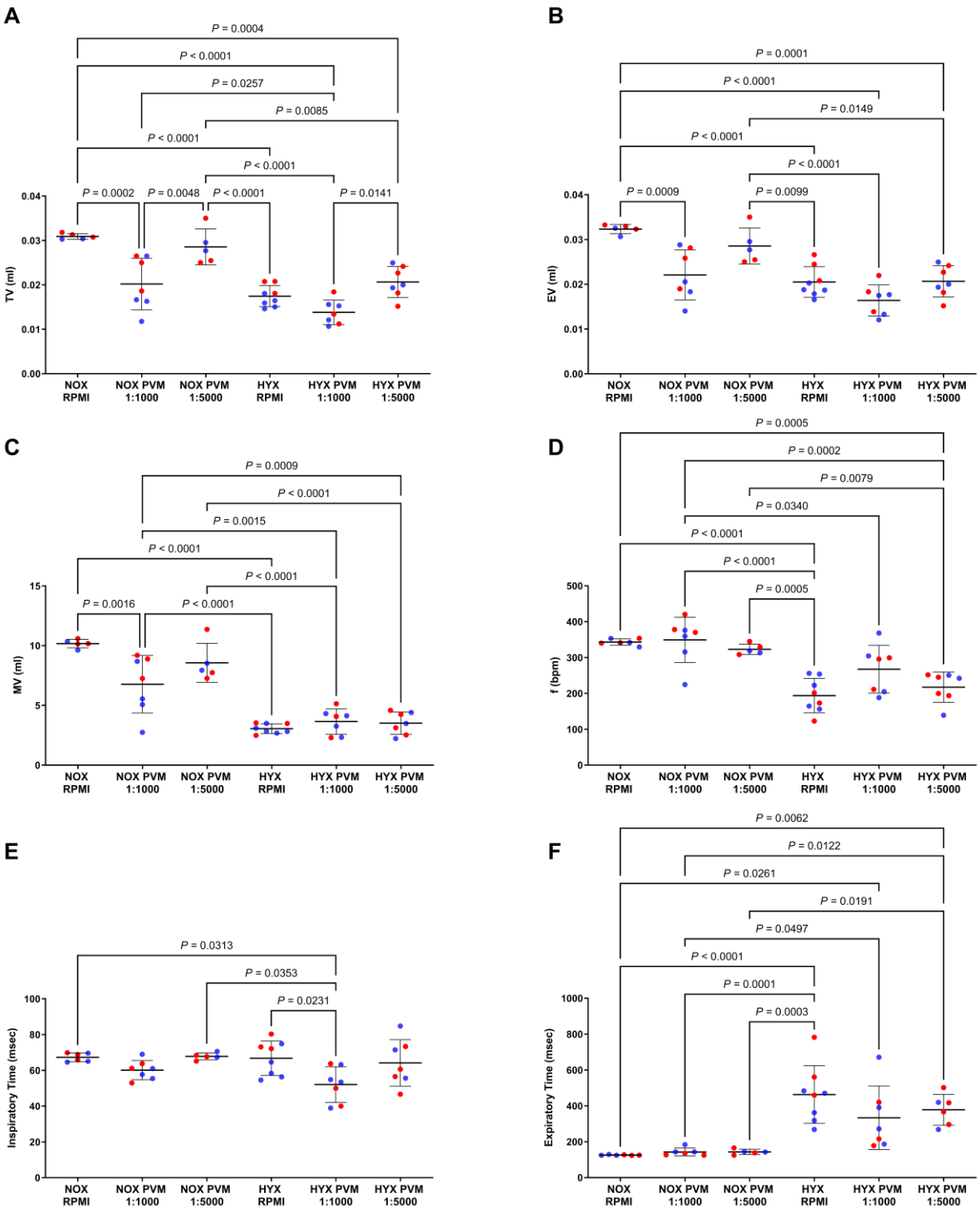

Figure 5. Effect of hyperoxia and PVM infection on lung physiology in neonatal mice.
Mice were exposed to normoxia (NOX; 21% O_2) or hyperoxia (HYX; 85% O_2) from birth, and administered intranasally RPMI, pneumonia virus of mice (PVM) 1:1,000, or PVM 1:5,000 at postnatal day (P)4. At P11, whole-body plethysmography was assessed. Data are presented as mean ± SD (n=5-8, per group). Statistical analysis was performed using one-way ANOVA with Tukey's *post hoc* test. Red dots indicate female mice, and blue dots indicate male mice.

4.4. Viral load dynamics in normoxia- and hyperoxia-exposed mice infected with PVM

The viral load of PVM was assessed in neonatal mice exposed to normoxia (21% O_2) or hyperoxia (85% O_2) from birth and infected intranasally on P4 with PVM diluted 1:1,000 in RPMI medium. Mouse lungs were collected at P4, P5, P7, and P10. The left lung lobe from each animal was used for RNA extraction and subsequent cDNA synthesis. Quantitative analysis revealed no significant differences in viral load between normoxia- and hyperoxia-exposed, PVM-infected mice, at any matched time point, except on P7, when the normoxia group exhibited significantly higher viral load than the hyperoxia group. In both groups, viral load increased significantly over time, with higher levels observed on P7 and P10 compared to P5 (**Figure 6**). These findings indicate that hyperoxia does not substantially alter PVM replication dynamics in the lung, while viral load increases significantly during the early stages of infection in both oxygen conditions.

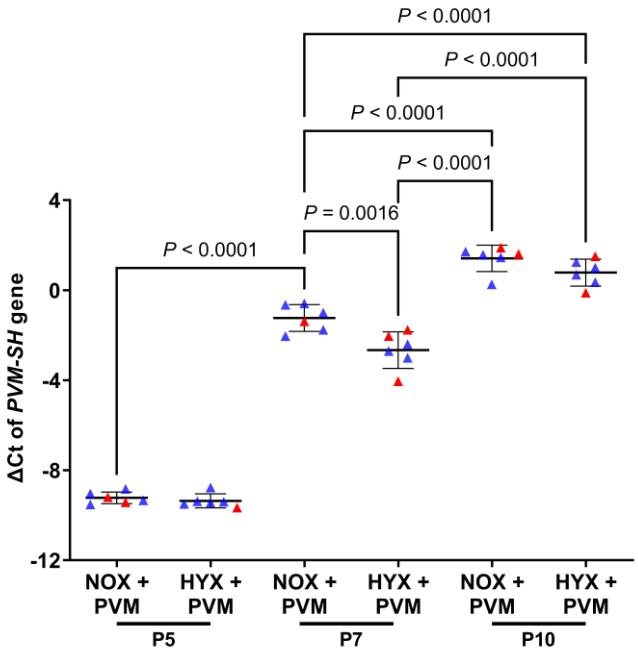

Figure 6. PVM viral load in the lungs of newborn mice exposed to normoxia or hyperoxia.
The viral load of pneumonia virus of mice (PVM) in the lungs of newborn mice exposed to normoxia (NOX; 21% O_2) or hyperoxia (HYX; 85% O_2) was assessed on postnatal day (P)5, P7, and P10 by quantitative polymerase chain reaction (qPCR). The levels of mRNA encoding the PVM small hydrophobic (SH) protein were quantified, with RNA polymerase II mRNA serving as the reference gene. Data are presented as mean ± SD (n=6, per group). Statistical analysis was performed using one-way ANOVA with Tukey's *post hoc* test. Red dots indicate female mice, and blue dots indicate male mice.

4.5. Gene expression analysis in lung homogenates of neonatal mice exposed to normoxia or hyperoxia and treated with RPMI or infected with PVM

The *Ccl5*, *Ear1*, *Ccl2*, *Cxcl10*, and *Ccl3* gene expression levels were analyzed in left lung homogenates from neonatal mice exposed to normoxia (21% O_2) or hyperoxia (85% O_2) from birth. Mice were treated intranasally on P4 with either RPMI medium as a control or PVM (1:1,000 dilution). Gene expression was quantified using qPCR, normalized to RNA polymerase II mRNA as the reference gene, and compared across groups to evaluate the effects of oxygen exposure and viral infection on inflammatory and immune response pathways. At P7, *Ccl5* expression was the highest in normoxia-infected mice, with elevated levels persisting at P10 and P11, while no significant differences in *Ccl5* expression were detected between groups at P5 (**Figure 7A**). In contrast, *Ccl2* and *Cxcl10* revealed increased expression in both hyperoxia control and hyperoxia-infected groups starting from P5. By P10 and P11, normoxia-infected mice exhibited *Cxcl10* expression levels comparable to those of hyperoxia-infected mice (**Figure 7D**), whereas *Ccl2* expression in normoxia-infected mice matched that of hyperoxia-infected mice only at P11 (**Figure 7C**). The *Ccl3* expression was increased in both hyperoxia conditions, with normoxia-infected mice reaching expression levels similar to hyperoxia-infected mice at P11 (**Figure 7E**). The *Ear1* expression revealed a trend of downregulation in both hyperoxia control and hyperoxia-infected groups compared to normoxic conditions (**Figure 7B**). These findings suggest that hyperoxia influences the expression of key inflammatory genes, with specific temporal patterns and interactions between oxygen exposure and viral infection shaping the immune response in neonatal lungs.

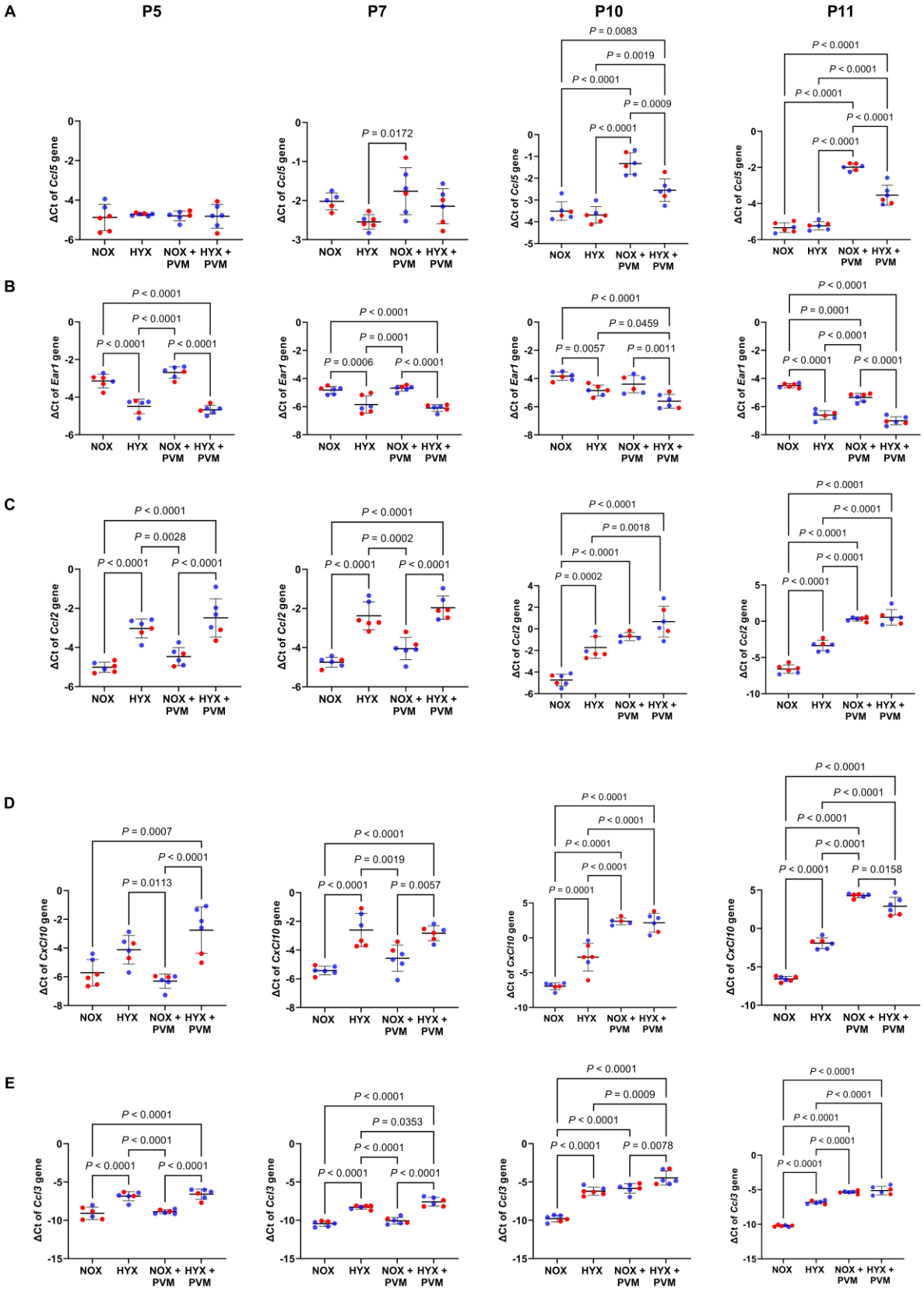

Figure 7. Continued overleaf

4.6. Collagen remodeling revealed by SHG microscopy of neonatal mice exposed to normoxia or hyperoxia and treated with RPMI or infected with PVM

Second harmonic generation (SHG) microscopy was employed to quantify collagen organization and density across four experimental conditions. Neonatal mouse pups were exposed to normoxic (21% O_2) or hyperoxic (85% O_2) conditions from birth. On P4, pups in each group received intranasal administration of either PVM diluted 1:1,000 in RPMI medium or RPMI medium alone as a control. Representative SHG images (**Figure 8**) illustrate qualitative differences in collagen distribution between groups, with the hyperoxia-infected group showing pronounced collagen signal compared to controls. Quantitative analysis of normalized SHG signal intensities (**Figure 9**) revealed significant differences between experimental groups. The hyperoxia-infected group exhibited the highest median SHG intensity, while the normoxia control group had the lowest. Hyperoxia alone significantly increased SHG intensity relative to normoxia in both infected and uninfected animals. These data suggest that hyperoxic exposure promotes collagen reorganization, potentially reflecting early fibrotic changes or compensatory matrix remodeling in response to oxidative stress. Both hyperoxia and PVM infection independently enhanced collagen organization and/or density, and their combined effects were synergistic, driving the most substantial alterations in tissue matrix architecture.

Figure 7. Gene expression analysis in lung homogenates of neonatal mice exposed to normoxia or hyperoxia and infected with PVM.

The *Ccl5*, *Ear1*, *Ccl2*, *Cxcl10,* and *Ccl3* gene expression levels were analyzed in left lung homogenates from mice exposed to normoxia (NOX; 21% O_2) or hyperoxia (HYX; 85% O_2). On postnatal day (P)4, pups in each group received an intranasal administration of either pneumonia virus of mice (PVM) diluted 1:1,000 in RPMI medium or RPMI medium alone as a control. Gene expression was quantified by quantitative polymerase chain reaction (qPCR) with *RNA polymerase II* mRNA as the reference gene, and compared between groups to evaluate the impact of oxygen exposure and viral infection on inflammatory and immune response pathways. Data are presented as mean of ΔCt ± SD (n=5-6, per group), and statistical significance was determined using one-way ANOVA followed by Tukey's *post hoc* test ($P < 0.05$). Red dots indicate female mice, and blue dots indicate male mice.

The increased SHG signal in hyperoxic and infected lungs likely reflects augmented collagen fiber content, modified fiber organization, or increased collagen crosslinking consistent with early fibrogenic remodeling. These results demonstrate that both hyperoxia and PVM infection contribute independently and additively to changes in collagen structure, with the combined treatment producing the most pronounced extracellular matrix remodeling detectable by SHG microscopy.

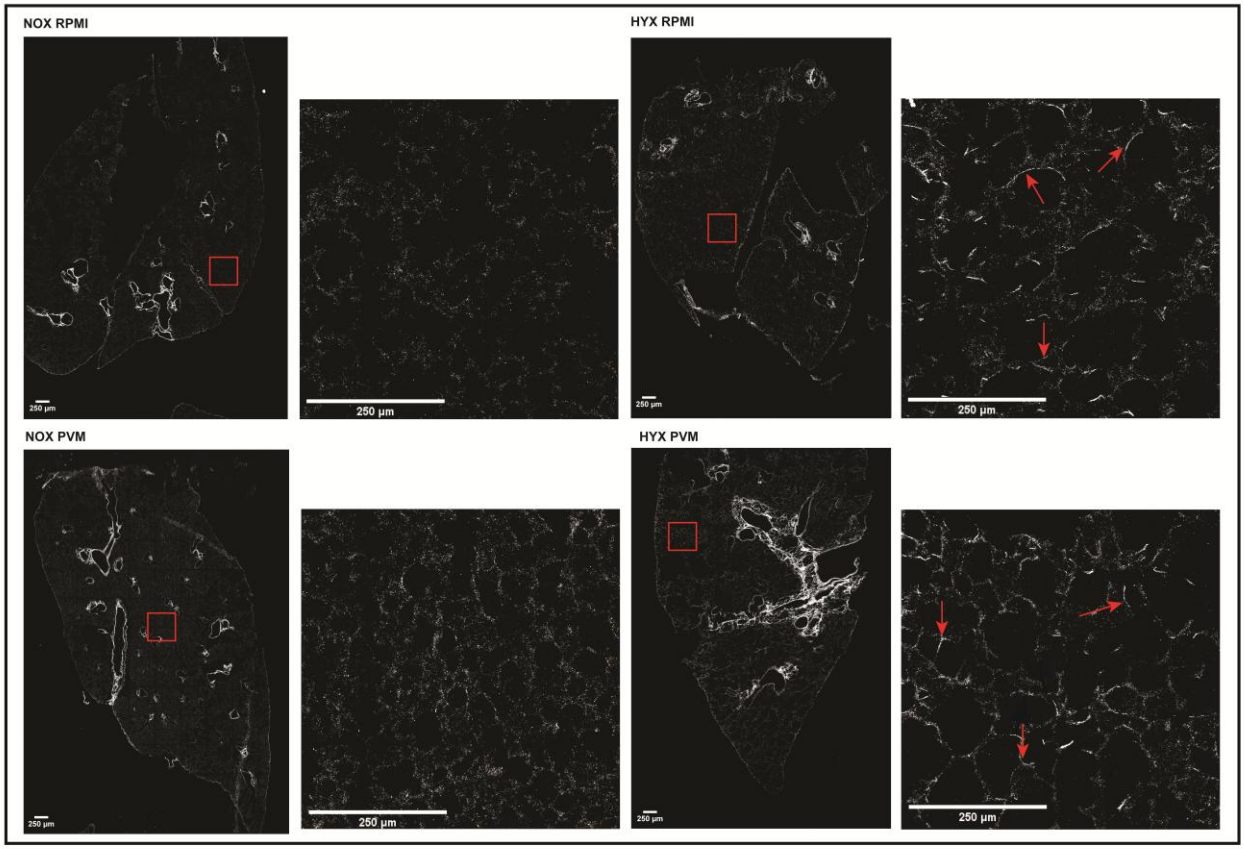

Figure 8. Second harmonic generation microscopy of collagen structures in neonatal mouse lungs following oxygen exposure and PVM infection.

Neonatal mouse pups were exposed to normoxia (NOX; 21% O_2) or hyperoxia (HYX; 85% O_2) from birth and treated intranasally on postnatal day (P)4 with either pneumonia virus of mice (PVM) 1:1,000 dilution or RPMI medium alone as a control. Lungs were collected at P11 and imaged by second harmonic generation (SHG) microscopy to visualize fibrillar collagen. Representative low-magnification images (left panels) and higher-magnification views of boxed regions (right panels) are shown for each condition. Red arrows indicate regions of increased collagen deposition and remodeling in hyperoxia-exposed groups. Scale bars: 250 µm.

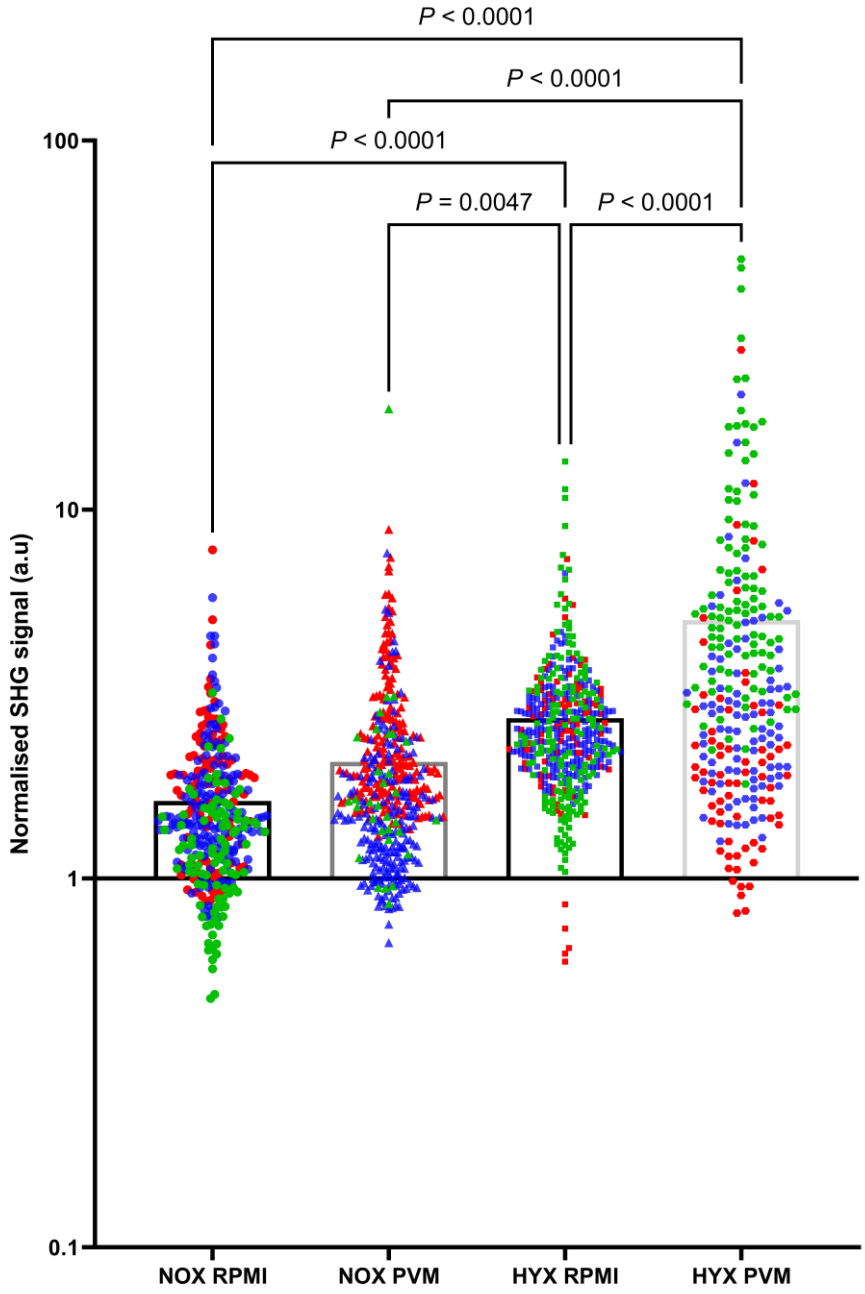

Figure 9. Quantification of collagen organization by second harmonic generation (SHG) microscopy under normoxic and hyperoxic conditions with or without PVM infection.

Neonatal mouse pups were exposed to normoxia (NOX; 21% O_2) or hyperoxia (HYX; 85% O_2) from birth and treated intranasally on postnatal day (P)4 with either pneumonia virus of mice (PVM) 1:1,000 dilution or RPMI medium alone as a control. SHG signal was collected in both forward and backward directions for each field of view, summed (BSHG + FSHG), and normalized to the mean summed SHG intensity of the normoxia control (NOX-RPMI) group. Scatter plots show the full distribution of normalized SHG intensities (a.u., arbitrary units) for each experimental condition; each dot represents a single field of view, and different colors (red, blue, green) denote data from individual animals. Statistical significance was determined using one-way ANOVA followed by Tukey's *post hoc* test ($P < 0.05$).

4.7. Impact of hyperoxia and PVM infection on lung protein expression in neonatal mice

Neonatal mouse pups were assigned to either normoxic (21% O_2) or hyperoxic (85% O_2) conditions from birth. On P4, pups in each group received an intranasal administration of either PVM diluted 1:1,000 in RPMI medium or RPMI medium alone as a control. Lungs were collected on P11 for analysis. Proteins were extracted with scioExtract buffer using the extraction standard operating procedure (SOP). Protein expression profiles in lung tissue samples were assessed using a dual-colour, reference-based design on scioCD antibody microarrays (Sciomics), which target a range of cluster of differentiation (CD) surface markers, cytokines, and chemokines.

Protein profiling of P11 neonatal mouse lungs revealed distinct expression patterns between normoxia control (NOX RPMI) and normoxia PVM-infected (NOX PVM) groups, highlighting the biological impact of viral infection under physiological oxygen conditions. In the NOX RPMI (control) group, the protein signature was characterized by molecules associated with tissue homeostasis, immune surveillance, and epithelial integrity. This included chemokines such as CCL2, CCL7, CCL8, and CCL26, which are involved in baseline leukocyte trafficking, and cytokines like IL-5, IL-9, IL-25, and IL-33, which support type 2 immune responses and tissue maintenance. Adhesion and epithelial markers (VCAM1, EPCAM, NCAM1, MUC1), as well as growth factors (BMP5, BMP6, VEGFC, CSF2), further reflected a balanced, non-inflamed lung environment conducive to normal development and immune readiness.

In contrast, the normoxic infected group exhibited a marked shift toward an inflammatory and reparative protein profile. There was elevated expression of pro-inflammatory cytokines and chemokines, including IL-6, IL-8, IL-13, IL-17C, CCL5, and CXCL13, indicating robust activation of antiviral and inflammatory pathways. Proteins involved in immune cell activation and recruitment (CD70, CD63, CD59, CSF1), as well as tissue remodeling and stress response (TGFB1, TGFB2, TGFB3, ADAM8, VGFR2, P53, EGLN), were upregulated. The presence of multiple TNF superfamily members (TNF10, TNF14, TNFB, TNF18) and regulatory molecules (IL1R2, ITAM) suggests a complex interplay between immune activation, regulation, and tissue adaptation during the response to viral infection.

In summary, PVM infection under normoxic conditions induces a pronounced transition from a homeostatic protein landscape to one dominated by inflammation,

immune cell recruitment, and tissue remodeling. These changes reflect the neonatal lung's dynamic response to viral challenge, balancing effective immune defense with mechanisms to limit tissue injury and promote repair. The results of this statistical analysis are presented in the corresponding volcano plot (**Figure 10**).

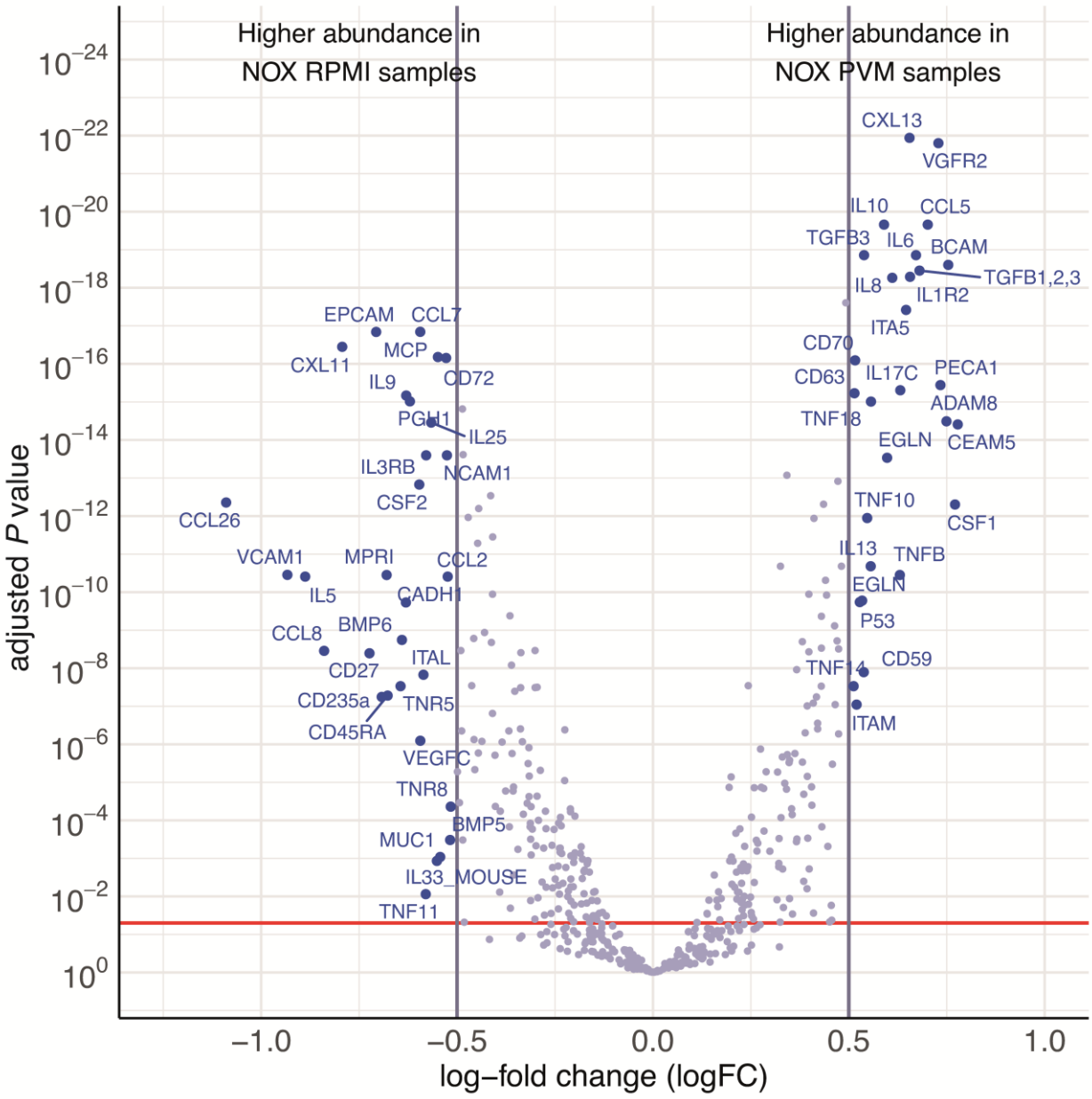

Figure 10. Differential protein expression between NOX RPMI and NOX PVM samples visualized by volcano plot.

Volcano plot visualising the differences in abundance between normoxia (NOX; 21% O_2) RPMI samples and NOX pneumonia virus of mice (PVM) samples as log-fold changes (logFC) and their corresponding *P* values (adjusted for multiple testing). The red line indicates a significance level of adjusted *P* value = 0.05, vertical lines indicate the logFC cutoffs of ±0.5. A positive logFC indicates higher abundance in NOX PVM samples, a negative logFC in NOX RPMI samples. Differential proteins (|logFC| > 0.5, adjusted *P* value < 0.05) are indicated by labeled blue text on the plot. Biological replicates per group: n=5.

Protein profiling of P11 neonatal mouse lungs exposed to hyperoxia also revealed distinct expression patterns between control (HYX RPMI) and PVM-infected (HYX PVM) groups, highlighting the profound impact of high oxygen exposure on the lung proteome.

In the HYX RPMI (hyperoxia control) group, the protein signature included molecules associated with immune surveillance and tissue maintenance, but also reflected features of hyperoxia-induced lung injury and disrupted development. This trend included elevated levels of chemokines (CCL7, CCL8, CCL15, CCL25, CCL26, CCL28, CXCL9), cytokines (IL-25, IL-20, CSF2), and growth factors (HGF, NAMPT), which support leukocyte trafficking and tissue responses to injury. Adhesion and epithelial markers (VCAM1, EPCAM, CADH1, CADH5, CD36), were present, as well as immune cell markers (CD14, CD45RA, CD53, CD72). This pattern is consistent with ongoing immune activation and altered tissue remodeling, representing a molecular signature of hyperoxia-induced lung stress.

In the HYX PVM (hyperoxia + PVM-infected) group, protein expression further shifted away from homeostasis, characterized by heightened inflammation, immune cell recruitment, and tissue remodeling. Compared to hyperoxia controls, there was increased abundance of chemokines and cytokines (CCL5, CCL17, CCL20, IL-4, IL-13, IL-15, SDF1) and markers of T cell activation and antigen presentation (CD8A, CD5, CD45RB, HLA-I, HLAG, LYAM2), indicating robust activation of both innate and adaptive immune responses. Upregulation of proteins involved in tissue remodeling and epithelial function (MUC1, PERM, K1C18, CADH2, ERBB2), as well as the presence of persistent inflammatory mediators (TNF14), further suggest maladaptive repair and chronic inflammation. Collectively, these findings highlight the synergistic and detrimental effects of combined oxygen toxicity and viral infection, resulting in chronic inflammation, impaired tissue development, and greater susceptibility to long-term lung disease. These findings are also summarized in a volcano plot (**Figure 11**).

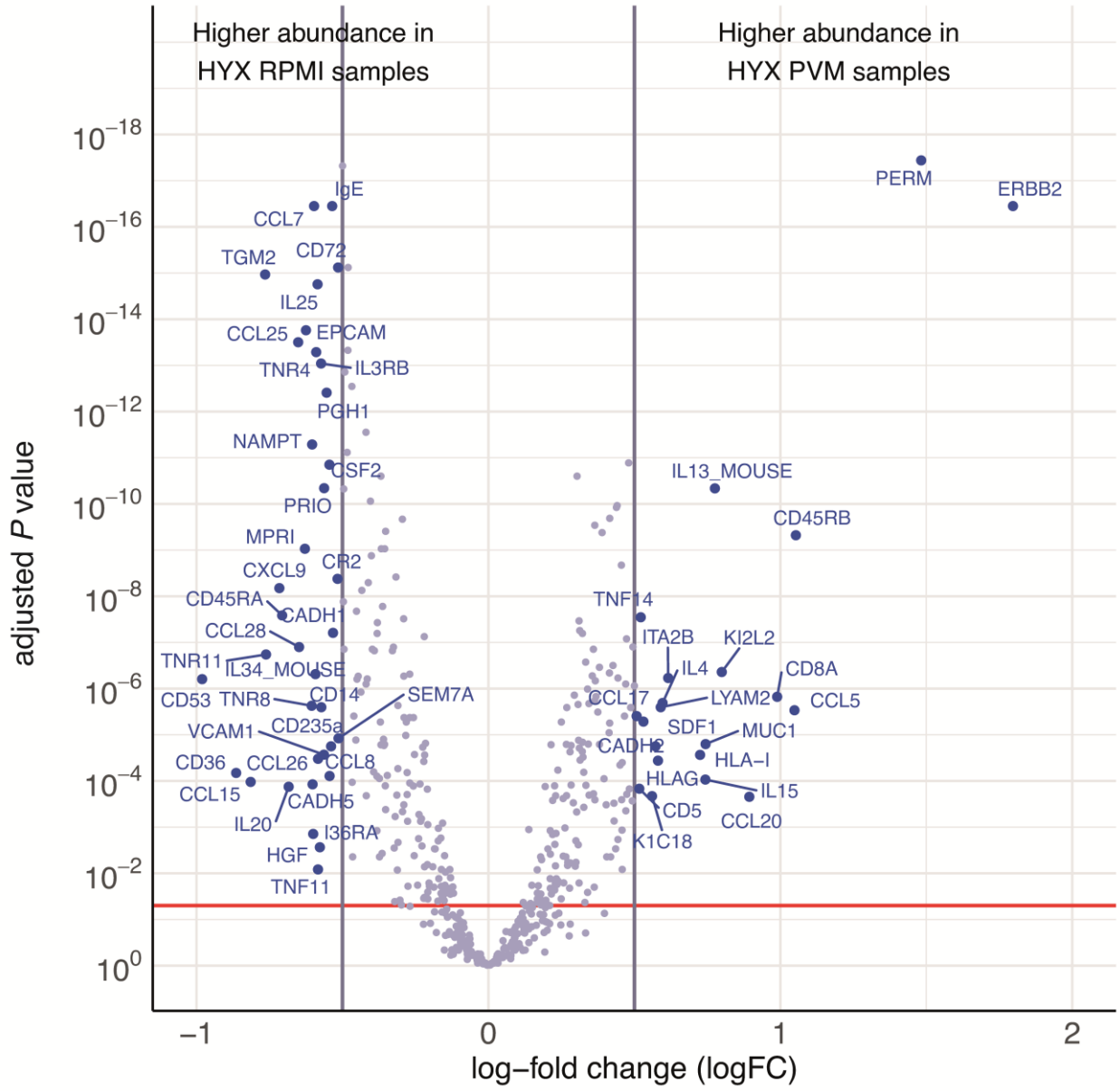

Figure 11. Differential protein expression between HYX RPMI and HYX PVM samples visualized by volcano plot.

Volcano plot visualising the differences in abundance between hyperoxia (HYX; 85% O_2) RPMI samples and HYX pneumonia virus of mice (PVM) samples as log-fold changes (logFC) and their corresponding *P* values (adjusted for multiple testing). The red line indicates a significance level of adjusted *P* value = 0.05, vertical lines indicate the logFC cutoffs of ±0.5. A positive logFC indicates higher abundance in HYX PVM samples, a negative logFC in HYX RPMI samples. Differential proteins (|logFC| > 0.5, adjusted *P* value < 0.05) are indicated by labeled blue text on the plot. Biological replicates per group: n=5.

4.8. Pathway enrichment analysis of differentially expressed proteins reveals distinct biological processes under hyperoxic and viral challenge conditions

To better interpret the biological significance of the observed protein expression changes across oxygen and infection conditions, functional pathway enrichment analysis was performed using Metascape. The resulting analyses provide insight into the cellular and molecular processes underlying the proteomic shifts described above.

Metascape enrichment analysis comparing NOX RPMI (uninfected control) and NOX PVM (PVM-infected) groups highlighted divergent biological processes underlying homeostasis versus infection-driven lung remodeling. In NOX RPMI lungs, proteins more abundantly expressed in the absence of infection were enriched in pathways reflecting immune homeostasis, tissue maintenance, and postnatal lung development. These included regulation of extracellular matrix (ECM) organization, epithelial cell differentiation, lung development, and negative regulation of inflammatory response, underlining a stable and low-inflammation environment. Further enrichment in cell–cell adhesion, immune surveillance without overt activation, and growth factor signaling pathways indicates tightly regulated immune and structural processes supporting healthy lung development.

Conversely, proteins elevated in the NOX PVM group pointed to a transition into an activated immune and inflammatory state. The most significantly enriched pathway was cytokine–cytokine receptor interaction, indicating strong activation of immune signaling networks in response to PVM infection. Additional overrepresented pathways included inflammatory response, cytokine-mediated signaling, and positive regulation of lymphocyte apoptotic process, reflecting increased immune activation, communication, and regulation of lymphocyte populations. Enrichment of viral protein interaction pathways, IL-17A signaling, and adaptive/humoral immunity, as well as pathways involved in cell-matrix adhesion and regulation of cellular response to growth factor stimulus, further illustrate the breadth of the lung's rapid defense mechanisms against viral challenge. These findings demonstrate that, under normoxia, the neonatal lung protein landscape can transition rapidly from homeostasis to a pro-inflammatory, remodeling state upon viral infection (**Figure 12**).

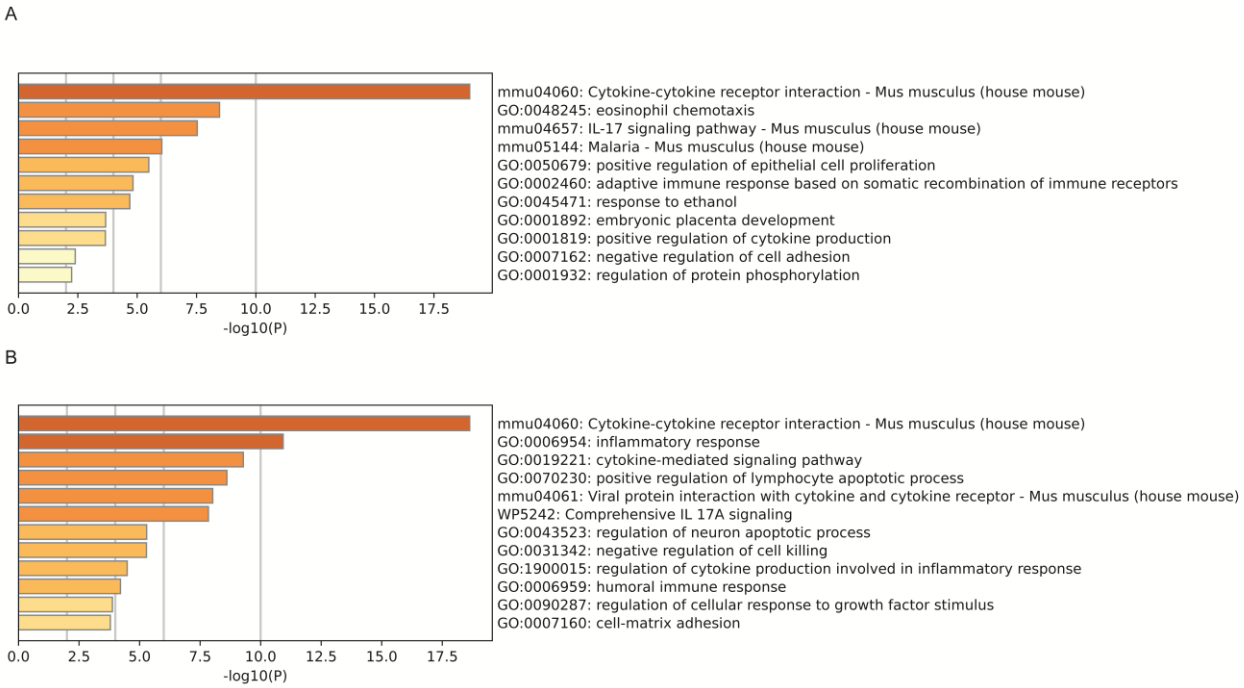

Figure 12. Pathway enrichment analysis of differentially abundant proteins in normoxic neonatal mouse lungs with and without PVM infection.

Bar plots display the top enriched pathways and biological processes identified by Metascape, based on proteins more highly expressed between (A) normoxia (NOX; 21% O_2) RPMI and (B) NOX pneumonia virus of mice (PVM) groups at postnatal day (P)11. The x-axis represents statistical significance as $\log_{10}$(adjusted *P* value). The most significantly enriched terms are shown in darker orange.

Under hyperoxic conditions, enrichment analyses (HYX RPMI vs. HYX PVM) revealed pervasive alterations in immune signaling and cell function. In the HYX RPMI group (hyperoxia control), the most significantly enriched pathway was cytokine–cytokine receptor interaction, suggestive of pronounced immune signaling network activation even without infectious challenge. Additional enriched pathways included cytokine-mediated signaling, hematopoietic cell lineage, positive regulation of myoblast fusion, and cellular response to lipopolysaccharide, all hinting at tissue remodeling and innate immune activation prompted by oxidative stress. Pathways supporting leukocyte proliferation and IL-17 signaling were also prominent, demonstrating a persistent pro-inflammatory environment. Notably, enrichment of lymphocyte-mediated immunity suggests that hyperoxia alone primes the developing lung for enhanced adaptive immune responses and a sustained non-homeostatic state.

Upon combined exposure to hyperoxia and PVM infection (HYX PVM), many of the above immune-related pathways remained significantly enriched but displayed greater complexity and amplification. Cytokine–cytokine receptor interaction remained the most prominent, with additional overrepresentation of pathways related to lymphocyte migration, leukocyte cell–cell adhesion regulation, and fibrotic tissue remodeling, most notably, heightened enrichment of the lung fibrosis pathway. These findings are reinforced by enrichment of pathways tied to hematopoietic cell lineage and negative regulation of cell adhesion, suggesting changes in immune cell populations and disruption of epithelial structure. Collectively, these analyses demonstrate that hyperoxia and viral infection each drive broad immune activation and tissue remodeling. However, their combination intensifies immune dysregulation and fibrotic responses, contributing to exacerbated lung injury and compromised postnatal lung development in neonates (**Figure 13**).

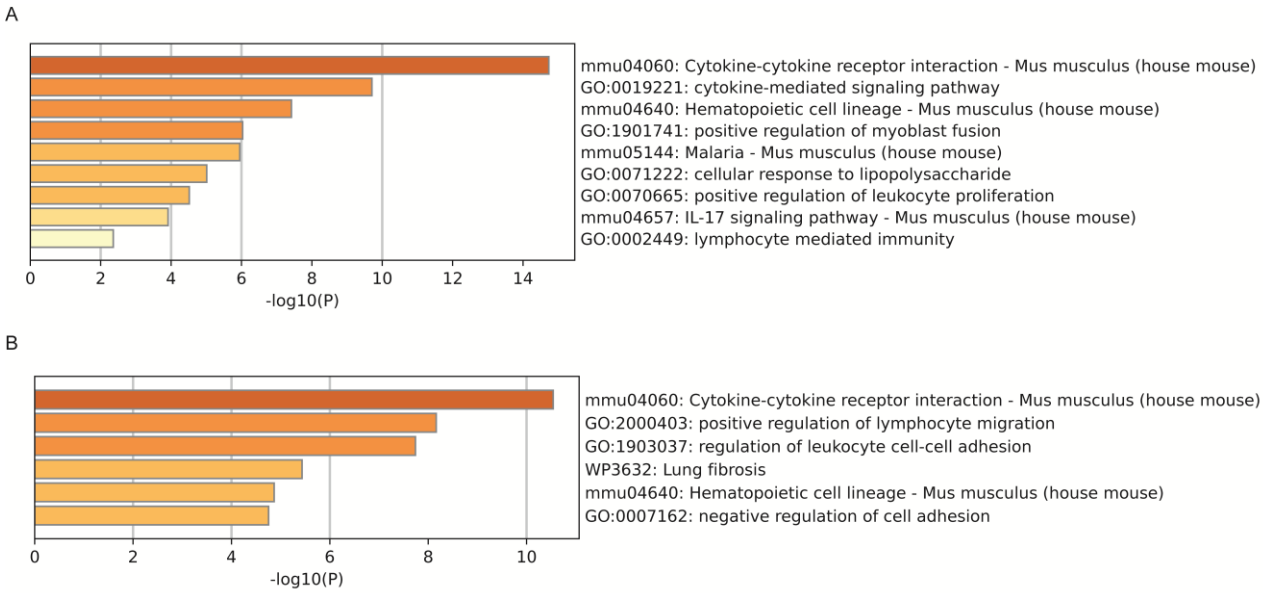

Figure 13. Pathway enrichment analysis of differentially abundant proteins in hyperoxic neonatal mouse lungs.

Bar plots display the top enriched pathways and biological processes identified by Metascape, based on proteins more highly expressed between (A) hyperoxia (HYX; 85% O_2) RPMI and (B) HYX pneumonia virus of mice (PVM) groups at postnatal day (P)11. The x-axis represents statistical significance as $\log_{10}$(adjusted *P* value). The most significantly enriched terms are shown in darker orange.

4.9. Immune cell population dynamics in the neonatal lung following hyperoxia and PVM infection

To evaluate the effects of hyperoxia and PVM infection on major lung immune cell populations, including macrophages, neutrophils, and dendritic cells, neonatal mouse pups were exposed to either normoxia (21% O_2) or hyperoxia (85% O_2) from birth. On P4, pups received an intranasal administration of either RPMI medium alone as a control or PVM diluted 1:1,000 in RPMI. Lungs were harvested on P10, enzymatically digested to generate single-cell suspensions, and analyzed via flow cytometry. CD45 was used as a pan-leukocyte marker to identify all immune cells within the lung single-cell suspension. Within the $CD45^+$ population, Ly6G served as an exclusion marker to remove neutrophils from further analysis. TR-AMs were then identified based on dual expression of CD11c and Siglec-F, while exudate macrophages were distinguished by their $CD11b^+$ $MHCII^-$ phenotype within the remaining myeloid compartment. Hyperoxia exposure significantly reduced the abundance of tissue-resident alveolar macrophages compared to normoxic controls, with this reduction being even more pronounced in hyperoxia-infected mice. This finding indicates that PVM infection exacerbates the depletion of tissue-resident alveolar macrophages under hyperoxic conditions. In contrast, the number of exudate macrophages increased significantly in both hyperoxia control and hyperoxia-infected groups compared to normoxia conditions, reflecting a shift toward inflammatory macrophage recruitment or expansion. Notably, normoxia-infected mice did not exhibit significant changes in the abundance of either macrophage population relative to normoxia controls. Dendritic cells were increased in number under both hyperoxia conditions, aligning with findings that hyperoxia selectively expands lung dendritic cell populations in neonates. Neutrophils also increased significantly in number in the hyperoxia control group and were further elevated in hyperoxia-infected mice, indicating an amplified inflammatory response (**Figure 14**). These results demonstrate that hyperoxia disrupts tissue-resident alveolar macrophage populations while promoting the recruitment or expansion of exudate macrophages, dendritic cells, and neutrophils. The combination of hyperoxia and PVM infection further amplifies these effects, suggesting a synergistic impact on lung immune cell dynamics in neonatal mice.

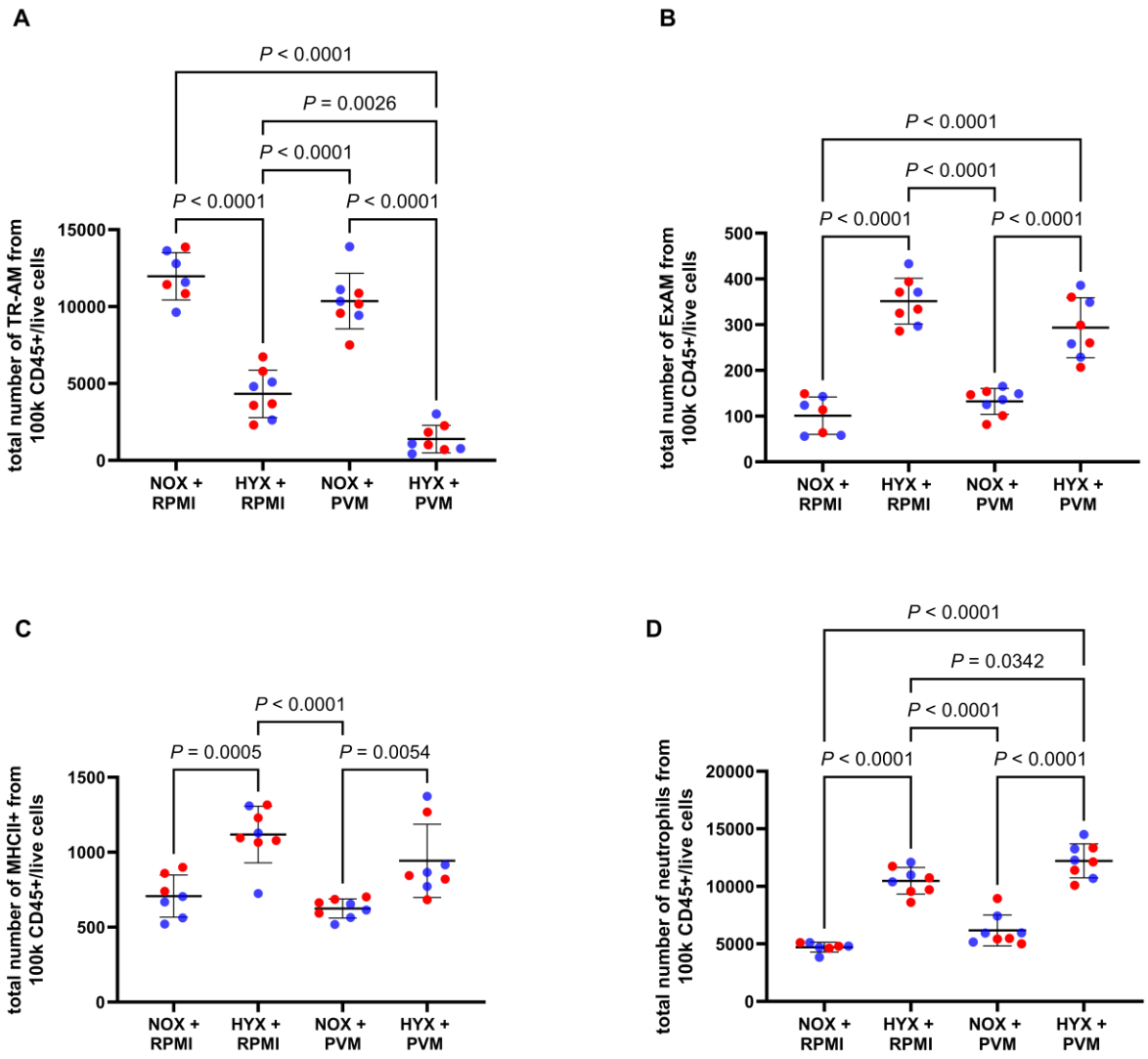

Figure 14. Immune cell dynamics in the lungs of neonatal mice exposed to normoxia or hyperoxia and infected with PVM.

Flow cytometric analysis of lung immune cell populations in neonatal mice exposed to normoxia (NOX; 21% O_2) or hyperoxia (HYX; 85% O_2) from birth and treated intranasally on postnatal day (P)4 with either pneumonia virus of mice (PVM) (1:1,000 dilution) or RPMI medium. Lungs were collected on P10, processed into single-cell suspensions, and stained for Ly6G, CD45, CD11c, Siglec-F, CD11b, and I-A/I-E. DAPI was used as a live/dead discriminator to exclude non-viable cells. Immune cell populations were quantified from 100,000 (100k) $CD45^+$/live cells per sample using FlowJo software. Each data point represents one mouse. Data reflect the abundance of each cell population per group. Statistical comparisons were performed using one-way ANOVA with Tukey's *post hoc* test; *P*-values are indicated above the relevant data points by horizontal black brackets. Data are presented as mean ± SD (n=7-8 per group).

4.10. Flow cytometric analysis of $CD4^+$, $CD8^+$ and γδ T cell populations in the neonatal lung across postnatal development

To examine the effects of hyperoxia and PVM infection on adaptive immune cell populations during early postnatal lung development, flow cytometry was performed to quantify $CD4^+$, $CD8^+$, and γδ T cells in lung tissue collected on P4, P7, and P10. Neonatal mice were continuously exposed to either normoxia (21% O_2) or hyperoxia (85% O_2) from birth. On P4, pups received an intranasal dose of either RPMI medium or PVM diluted 1:1,000 in RPMI. As infection was initiated on P4, samples collected at that time represent only baseline, pre-infection differences. At P4, there were no significant differences in total $CD4^+$, $CD8^+$, or γδ T cell numbers between groups, indicating that early T cell populations are relatively unaffected by oxygen exposure at this stage. By P7, however, PVM infection under normoxic conditions led to a significant increase in both $CD4^+$ and $CD8^+$ T cells compared to uninfected controls, reflecting rapid T cell recruitment or expansion in response to viral challenge. This expansion was absent in hyperoxia-infected animals, suggesting that hyperoxic injury impairs or limits T cell accumulation in the lung following infection. In contrast, γδ T cells displayed a distinct pattern: at P7, hyperoxia-infected animals exhibited the highest total γδ T cell counts across all 4 groups, indicating preferential expansion or recruitment under hyperoxic stress. By P10, $CD4^+$ and $CD8^+$ T cell numbers remained elevated in normoxia-infected group, but were significantly lower in hyperoxia-exposed and hyperoxia-infected groups, confirming a dampened adaptive response in hyperoxia. Notably, γδ T cells in hyperoxia-infected animals continued to exceed those in normoxia-infected group, underscoring a robust or compensatory innate-like γδ T cell response in the injured lung environment (**Figure 15**). Together, these data demonstrate that hyperoxia selectively impairs conventional $CD4^+$ and $CD8^+$ T cell responses to PVM infection while augmenting γδ T cell accumulation during early postnatal lung development.

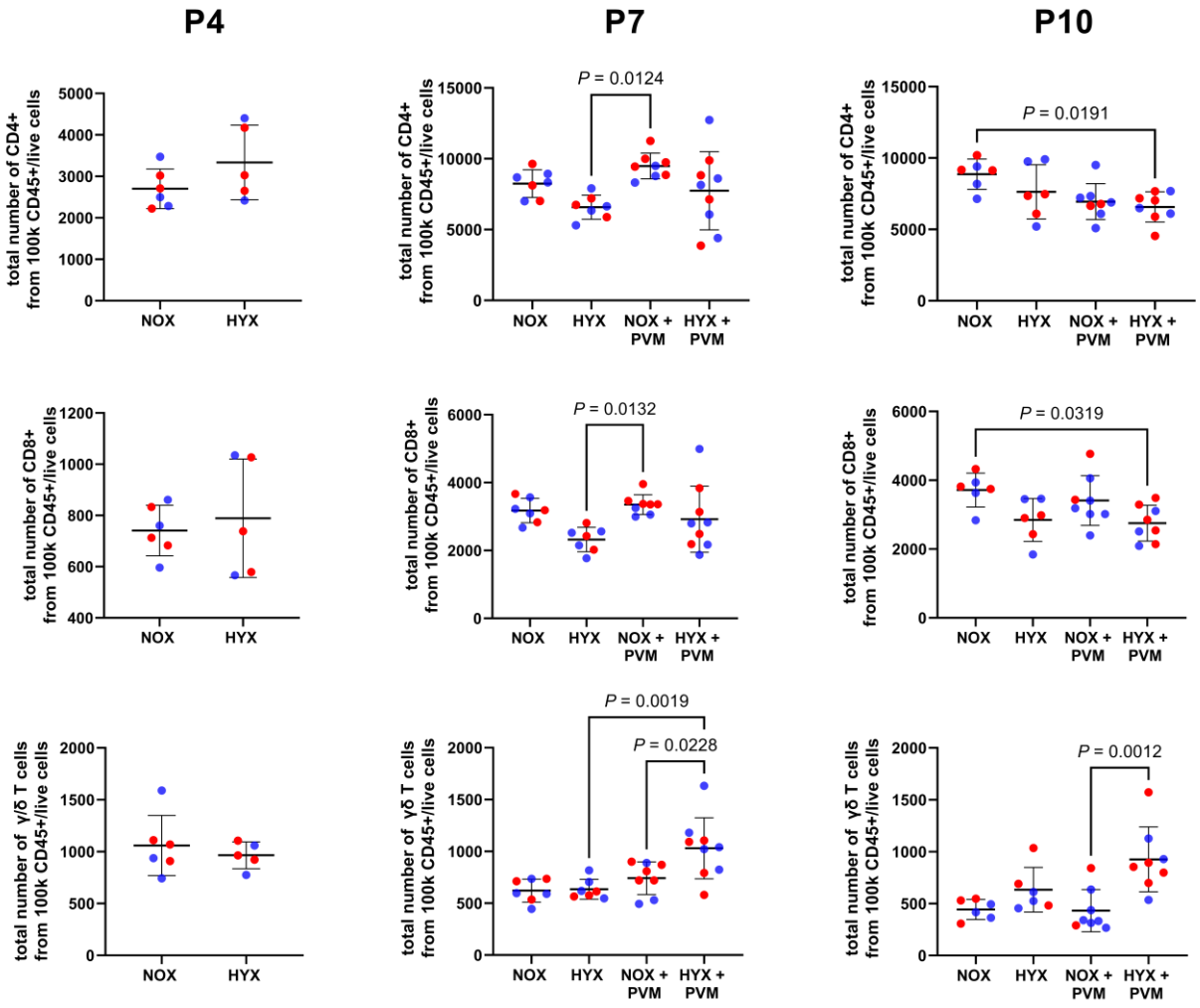

Figure 15. Dynamics of lung T cell populations in neonatal mice following exposure to hyperoxia and PVM infection.

Flow cytometric analysis of lung single-cell suspensions was performed to quantify T cell populations in neonatal mice exposed to either normoxia (21% O_2; NOX) or hyperoxia (85% O_2; HYX) from birth. On postnatal day (P)4, pups received intranasal PVM 1:1,000 dilution or RPMI medium (control). Lungs were collected at P4, P7, and P10, processed to single-cell suspensions, and stained for CD45, CD3, CD20, CD4, CD8, and TCR γ/δ surface markers; DAPI was used to exclude non-viable cells. T cell subsets were quantified from 100,000 (100k) $CD45^+$/live cells per sample using FlowJo software. Each data point represents an individual mouse; red dots indicate female mice, blue dots indicate male mice. Statistical analysis was conducted using one-way ANOVA with Tukey's *post hoc* test for data at P7 and P10, and unpaired Student's t-test for P4; exact *P*-values are indicated above comparisons by horizontal black brackets. Data are presented as mean ± SD (n=5-9, per group).

4.11. Hyperoxia induces distinct gene expression changes in lung inflammatory cells excluding neutrophils

Bulk RNA sequencing of $CD45^{+}CD11c^{+}Gr\text{-}1^{-}$ lung cells sorted from P10 mice exposed from birth to normoxia or hyperoxia revealed distinct gene expression programs induced by oxygen stress. Under normoxic conditions, genes such as *Ear1* and *Ear2*, markers of macrophage plasticity and homeostasis, were robustly expressed, mirroring the presence of tissue-resident alveolar macrophages and an immune environment primed for tissue maintenance, efficient extracellular RNA clearance, and antiviral defense. With hyperoxia exposure, expression of *Ear1* and *Ear2* was dramatically reduced, reflecting the depletion of tissue-resident alveolar macrophages under high oxygen. Instead, hyperoxia led to prominent upregulation of genes including *Itgam*, *Ccl9*, *Cd63*, *Cd68*, and *Rgcc*, all associated with myeloid cell activation, chemotaxis, proliferation, and pro-inflammatory adaptation (**Figure 16**). This gene expression shift signifies a loss of alveolar macrophage plasticity and a transition toward a more activated, inflammatory myeloid phenotype in the neonatal lung. These data support the conclusion that hyperoxia depletes the tissue-resident alveolar macrophage pool and reprograms remaining inflammatory cells toward activation and recruitment, likely compromising pulmonary immune homeostasis and repair in the developing lung.

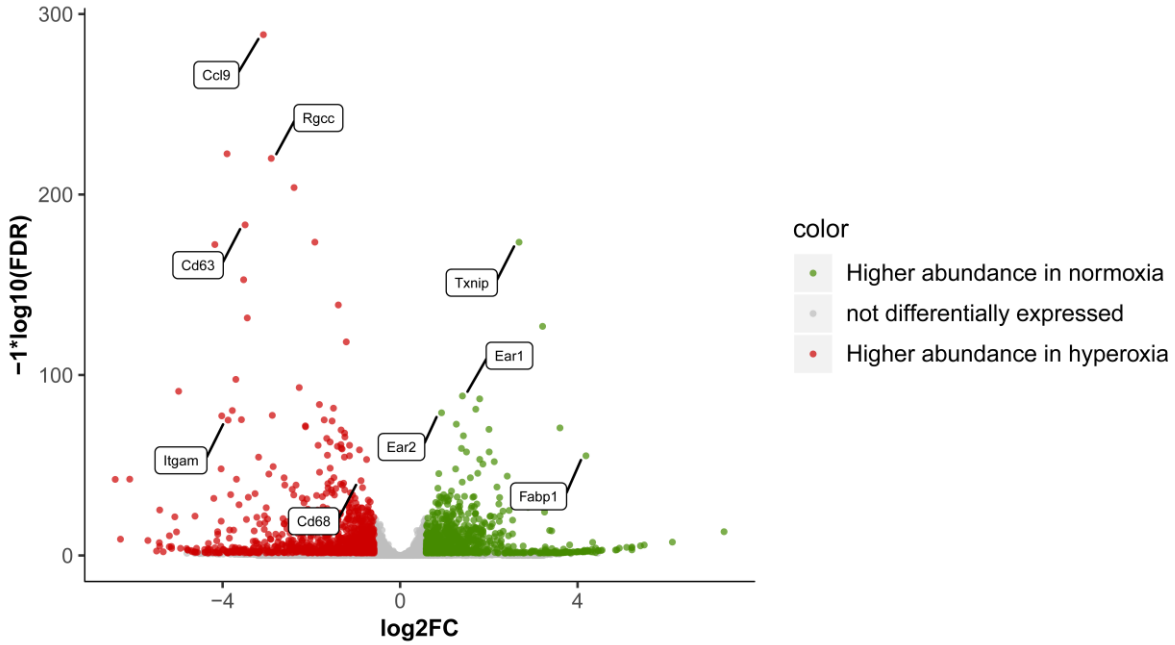

Figure 16. Volcano plot displaying differential gene expression in lung CD45⁺CD11c⁺Gr-1⁻ cells from P10 mice exposed to normoxia or hyperoxia.

Each point represents a gene, plotted by $\log_2$ fold change ($\log_2$FC) versus statistical significance ($-\log_{10}$ false discovery rate (FDR)). Red dots indicate genes significantly upregulated in hyperoxia, green dots represent genes upregulated in normoxia, and grey dots mark non-regulated genes. The most significantly regulated genes are annotated. Thresholds for significance (adjusted *P* value = 0.05) and biological relevance ($\log_2$FC ±0.5) are indicated by a horizontal red line and vertical lines, respectively.

4.12. Single-cell RNA sequencing reveals immune cell population shifts in neonatal mouse lungs following hyperoxia and PVM infection

Neonatal mouse pups were exposed to either normoxia (21% O_2) or hyperoxia (85% O_2) from birth. On P4, mice received either intranasal administration of RPMI medium alone as a control or PVM diluted 1:1,000 in RPMI medium. Lungs were harvested from neonatal mice on P10, digested to generate single-cell suspensions, and stained with antibodies against CD45, CD11c, and Gr-1. CD45⁺CD11c⁺Gr-1⁻ cells were sorted using a BD FACSAria™ III Cell Sorter, enriching for lung myeloid antigen-presenting cells, namely alveolar and interstitial macrophages as well as dendritic cells, while excluding neutrophils. Sorted cells were then subjected to single-cell RNA sequencing using the 10x Genomics platform. Single-cell RNA sequencing analysis revealed distinct shifts in immune cell populations across the four

experimental conditions, reflecting differential responses to hyperoxia exposure and viral infection (**Figure 17**).

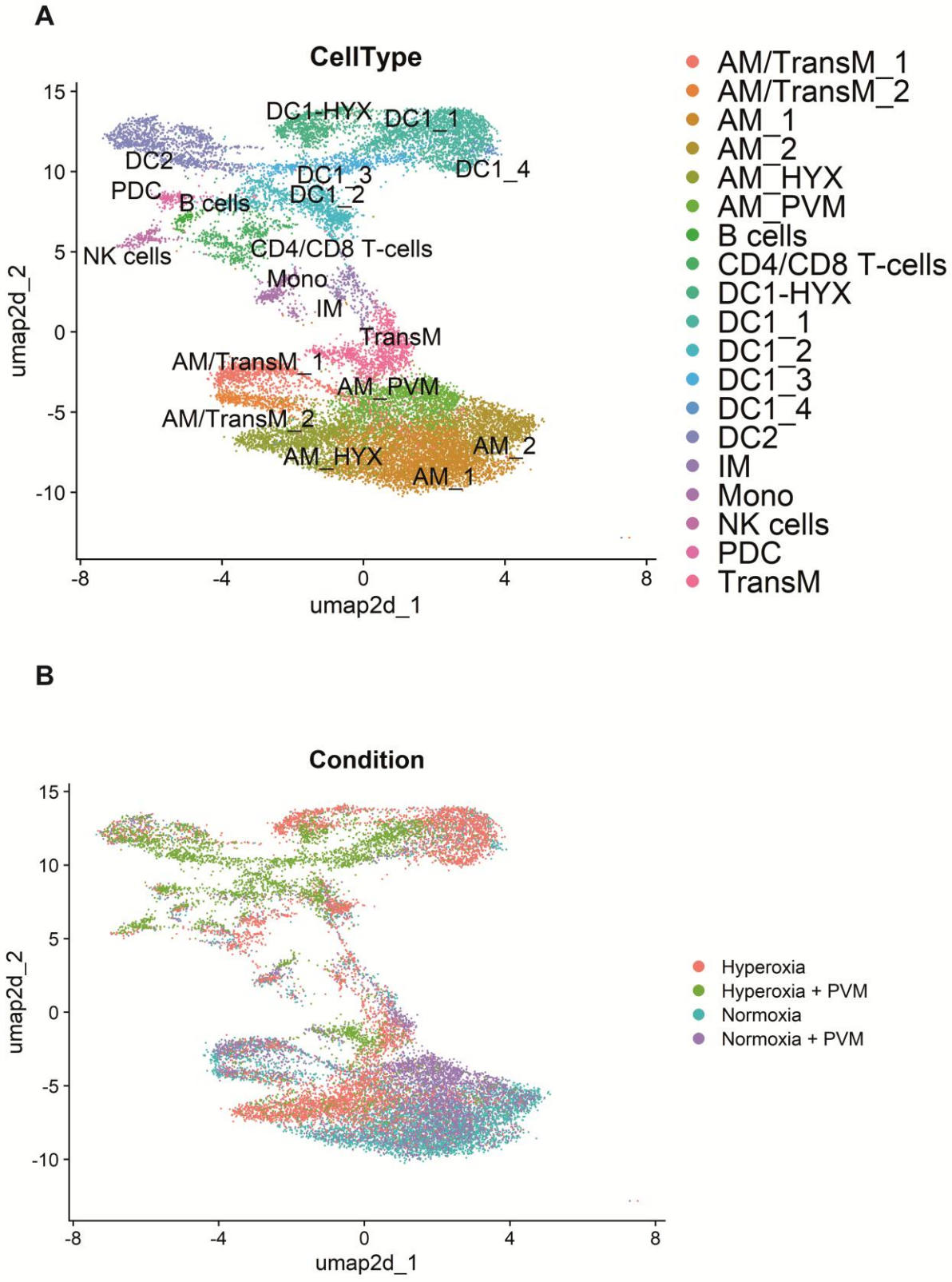

Figure 17. Continued overleaf

Figure 17. Single-cell transcriptomic profiling of neonatal mouse lungs under four experimental conditions at P10.

Uniform Manifold Approximation and Projection (UMAP) plots of single-cell RNA sequencing data from neonatal mouse lungs collected at postnatal day (P)10. Mice were exposed from birth to either normoxia (21% O_2) or hyperoxia (85% O_2) and received intranasal administration of either PVM 1:1,000 dilution in RPMI or RPMI medium alone as a control. (A) Cells are annotated by cell type according to transcriptional clustering and canonical marker gene expression. (B) The distribution of cells from each experimental condition is projected onto the same UMAP, illustrating the impact of hyperoxia and PVM infection on lung cellular composition and transcriptomic diversity. Each point represents a single cell; colors indicate either cell type (A) or experimental condition (B). AM/TransM_1, alveolar macrophage/transition macrophage subsets 1; AM/TransM_2, alveolar macrophage/transition macrophage subsets 2; AM_1, alveolar macrophages 1; AM_2, alveolar macrophages 2; AM_HYX, alveolar macrophages in hyperoxia-exposed samples; AM_PVM, alveolar macrophages from PVM-infected conditions; B cells, B lymphocytes; CD4/CD8 T-cells, $CD4^+$ and $CD8^+$ T lymphocytes. DC1_HYX, dendritic cell 1 in hyperoxia; DC1_1, DC1_2, DC1_3, and DC1_4, dendritic cell 1 subsets 1 through 4; DC2, dendritic cell 2; IM, interstitial macrophages; Mono, monocytes; NK cells, natural killer cells; PDC, plasmacytoid dendritic cells; TransM, transitional macrophages.

Under normoxic control conditions, the lung immune landscape was predominantly composed of alveolar macrophages, with AM_1 representing the most abundant population, followed by AM_2 and AM/TransM_1. This distribution reflects the homeostatic state of the neonatal lung, where TR-AMs maintain pulmonary homeostasis and surveillance functions. PVM infection under normoxic conditions (Normoxia + PVM) resulted in a notable redistribution of macrophage populations. AM_1 remained prominent, but there was a substantial emergence of AM_PVM, indicating viral-responsive macrophage activation. Additionally, the presence of transitional macrophages (TransM), suggested active macrophage polarization and recruitment in response to viral challenge. This balanced macrophage response correlated with the preserved lung architecture and improved survival observed in this group. Hyperoxia exposure alone dramatically altered the cellular composition, with a marked shift toward specialized stress-responsive populations. AM_HYX became prominent, representing hyperoxia-adapted alveolar macrophages, while DC1_1 also expanded significantly. The reduction in AM_1 compared to normoxic conditions indicated a transition from homeostatic to stress-adapted macrophage phenotypes. The combination of hyperoxia and PVM infection (Hyperoxia + PVM) produced the most dramatic cellular reprogramming, characterized by extensive dendritic cell expansion. DC2 emerged as a major population, accompanied by substantial

increases in DC1_2 , DC1_3, and other DC subsets (**Figure 18**). This profound shift toward inflammatory dendritic cell subtypes paralleled the severe mortality and exacerbated lung pathology observed in this experimental group. The absence of AM_HYX cells in the hyperoxia-infected group, despite the presence of these cells in hyperoxia controls, suggests that these macrophages are either depleted, functionally altered, or replaced by recruited monocytes and dendritic cells during viral infection under hyperoxic stress. Without AM_HYX cells, the lung is dominated by inflammatory myeloid cells, which are less effective at maintaining tissue integrity and more prone to driving damaging inflammation. The inability to control inflammation and repair tissue likely underlies the high mortality and severe lung pathology observed in hyperoxia-infected neonates.

In summary, the selective enrichment of AM_PVM in normoxia-infected mice coincides with robust survival and preserved lung architecture, underscoring its critical protective role during respiratory viral infection. Conversely, the loss of AM_PVM and AM_HYX in hyperoxic conditions is associated with heightened inflammation and mortality.

Collectively, these data indicate that while normoxic conditions support a protective macrophage landscape during infection, hyperoxia disrupts this balance and, when combined with viral infection, drives a maladaptive immune response characterized by loss of alveolar macrophages and expansion of inflammatory myeloid cells, which may underlie the poor survival outcomes observed in hyperoxia-infected neonates.

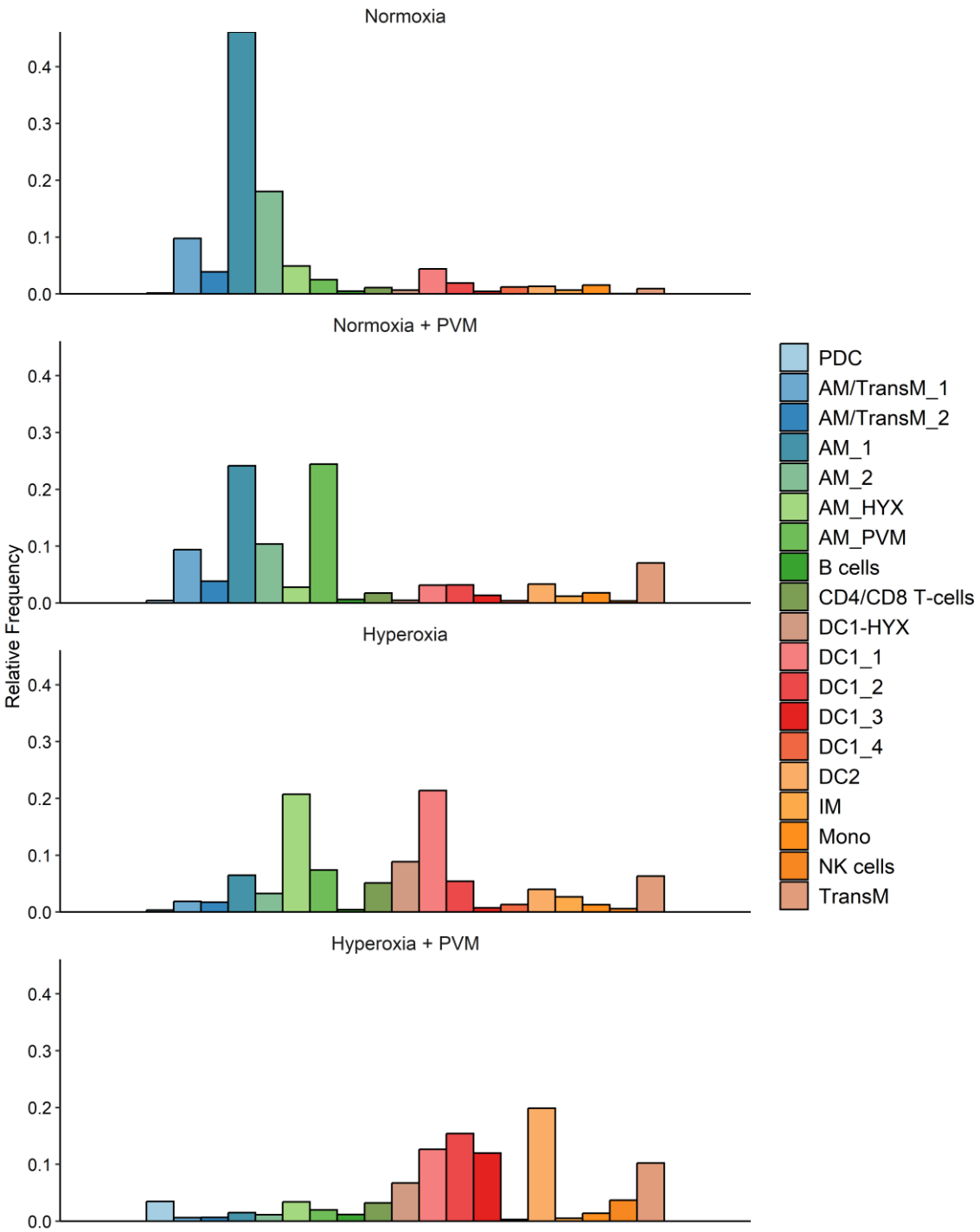

Figure 18. Relative frequency of lung immune cell populations across oxygen and infection conditions at P10, determined by single-cell RNA sequencing.

Bar plots show the relative abundance of major cell types identified in neonatal mouse lungs exposed from birth to one of four conditions: normoxia (normoxia), normoxia with PVM infection (normoxia + PVM), hyperoxia (hyperoxia), and hyperoxia with PVM infection (hyperoxia + PVM). Cell identity was assigned by transcriptional clustering and canonical marker gene expression. Each bar represents the mean relative frequency of each cell type within the indicated condition. Colors correspond to individual cell types, as indicated in the legend. Continued overleaf.

Figure 18. Continued

AM/TransM_1, alveolar macrophage/transition macrophage subsets 1; AM/TransM_2, alveolar macrophage/transition macrophage subsets 2; AM_1, alveolar macrophages 1; AM_2, alveolar macrophages 2; AM_HYX, alveolar macrophages in hyperoxia-exposed samples; AM_PVM, alveolar macrophages from PVM-infected conditions; B cells, B lymphocytes; CD4/CD8 T-cells, $CD4^+$ and $CD8^+$ T lymphocytes. DC1_HYX, dendritic cell 1 in hyperoxia; DC1_1, DC1_2, DC1_3, and DC1_4, to dendritic cell 1 subsets 1 through 4; DC2, dendritic cell 2; IM, interstitial macrophages; Mono, monocytes; NK cells, natural killer cells; PDC, plasmacytoid dendritic cells; TransM, transition macrophages.

4.13. Tissue-resident alveolar macrophage depletion using clodronate liposomes via different administration routes

To deplete alveolar macrophages, neonatal mice were treated with clodronate liposomes administered either IP or IN on P3, P6, and P9. Control liposomes were administered via both routes to the respective control groups. Lungs were harvested on P10, and flow cytometry was performed to quantify tissue-resident alveolar macrophages, exudate macrophages, and neutrophils. Intraperitoneal administration of clodronate liposomes did not reduce the number of tissue-resident alveolar macrophages compared to controls but led to an increase in exudate macrophage numbers. In contrast, intranasal administration resulted in effective depletion of tissue-resident alveolar macrophages without affecting exudate macrophages. Neutrophil numbers increased following both routes of administration, but were significantly higher after intranasal delivery (**Figure 19**).

These results indicate that intranasal administration is a more effective route for depleting tissue-resident alveolar macrophages in neonatal mice, while minimizing unintended effects on other lung immune cell populations. This method offers a targeted approach for investigating the functional role of tissue-resident alveolar macrophages in neonatal lung immune responses.

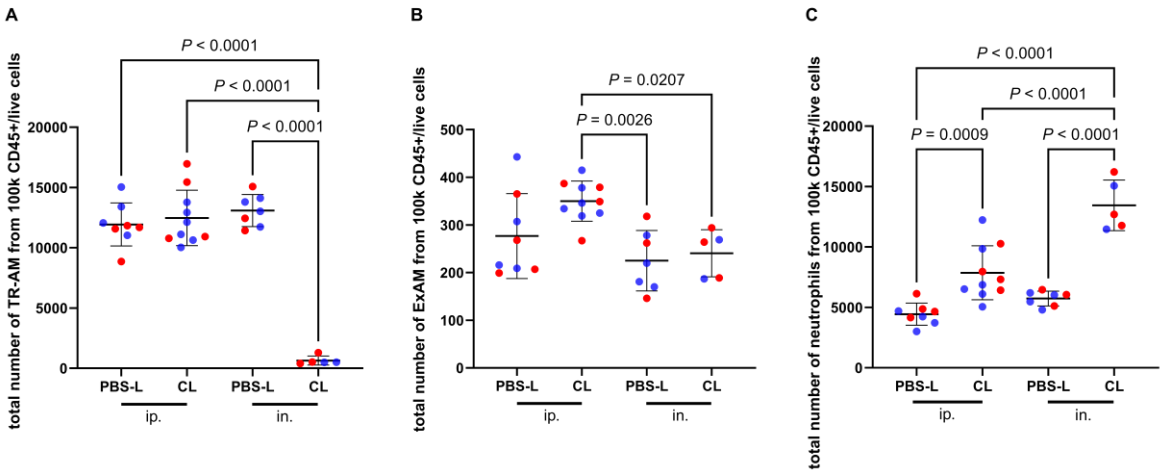

Figure 19. Intranasal administration of clodronate liposomes effectively depletes tissue-resident alveolar macrophages in neonatal lungs.

Neonatal mice were treated with either clodronate liposomes (CL) or control PBS-liposomes (PBS-L) via intraperitoneal (IP) or intranasal (IN) routes on postnatal day (P)3, P6, and P9. Lungs were harvested on P10, and flow cytometry was used to quantify (A) tissue-resident alveolar macrophages (TR-AM), (B) exudate macrophages (ExAM), and (C) neutrophils. Immune cell populations were quantified from 100,000 (100k) $CD45^+$/live cells per sample using FlowJo software. Each dot represents an individual animal, with red indicating females and blue indicating males. Data were analyzed using one-way ANOVA with Tukey's *post hoc* test. Data are presented as mean ± SD (n=5-10, per group).

4.14. Lung $CD103^+$ dendritic cell counts in neonatal mice after clodronate liposome or hyperoxia exposure

To evaluate whether intranasal administration of clodronate liposomes affects lung dendritic cell populations, neonatal mice were treated intranasally with control liposomes (PBS-L) or clodronate liposomes (CL) on postnatal days 3, 6, and 9. Hyperoxia-exposed mice from birth to P10 served as a positive control, as hyperoxia is known to increase dendritic cell numbers. Flow cytometric analysis conducted on lungs harvested at P10 quantified the total number of $CD103^+$ dendritic cells among 100,000 $CD45^+$ live cells. The results show that intranasal clodronate treatment did not reduce the number of $CD103^+$ dendritic cells compared to control liposome-treated animals (PBS-L). As expected, an increase was observed in the hyperoxia group, with $CD103^+$ cell counts significantly higher compared to both PBS-L and CL groups (**Figure 20**). These data indicate that intranasal clodronate treatment selectively depletes alveolar macrophages without substantially affecting lung $CD103^+$ dendritic

cell populations, ensuring the specificity of this macrophage depletion strategy in neonatal mice.

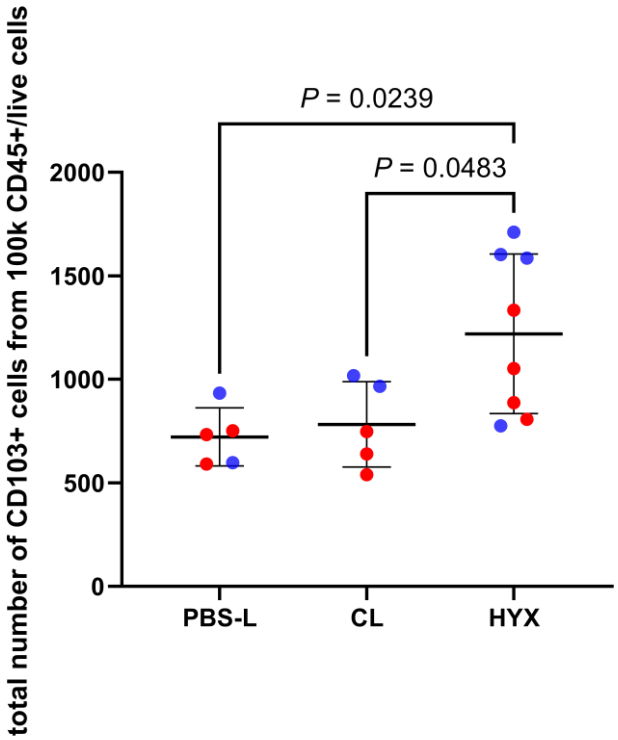

Figure 20. Effect of intranasal clodronate liposomes and hyperoxia on lung CD103⁺ dendritic cell numbers in neonatal mice.

Neonatal mice were treated intranasally on postnatal day (P)3, P6, and P9 with either control liposomes (PBS-L) or clodronate liposomes (CL) to evaluate the impact on lung dendritic cells. A separate group was exposed to hyperoxia (HYX; 85% O_2) from birth to P10 as a positive control known to increase dendritic cell numbers. Lungs harvested at P10 were analyzed by flow cytometry to quantify the absolute number of CD103⁺ dendritic cells among 100,000 (100k) CD45⁺ live cells. Each dot represents an individual animal, with red indicating females and blue indicating males. Data are presented as mean ± SD (n = 5-8, per group). Statistical differences were determined by one-way ANOVA with Tukey's *post hoc* test.

4.15. Survival analysis of mice treated with clodronate liposomes and infected with PVM

To determine the role of macrophages in survival following PVM infection, neonatal mice were exposed from birth to either normoxia (21% O_2) or hyperoxia (85% O_2). Tissue-resident alveolar macrophages were depleted by intranasal administration of clodronate liposomes on P3, P6, P9, P12, and P15. On P4, mice were infected intranasally with PVM 1:1,000 dilution, while control groups received RPMI alone.

Survival was monitored daily. Clodronate liposome-mediated depletion of macrophages resulted in dramatically reduced survival of PVM-infected mice under both normoxic and hyperoxic conditions, with 100% mortality observed by P15 and P16, respectively. However, all control mice survived throughout the observation period. Strikingly, the complete loss of survival in the normoxic, PVM-infected group with clodronate treatment phenocopied the outcome seen in our previous survival study in which hyperoxia-exposed, PVM-infected neonates died by P12 in the absence of macrophage depletion (**Figure 21**). Thus, elimination of macrophages in normoxia was sufficient to replicate the increased vulnerability typically associated with hyperoxia and viral infection. These findings highlight a critical protective role for macrophages in neonatal survival during PVM infection.

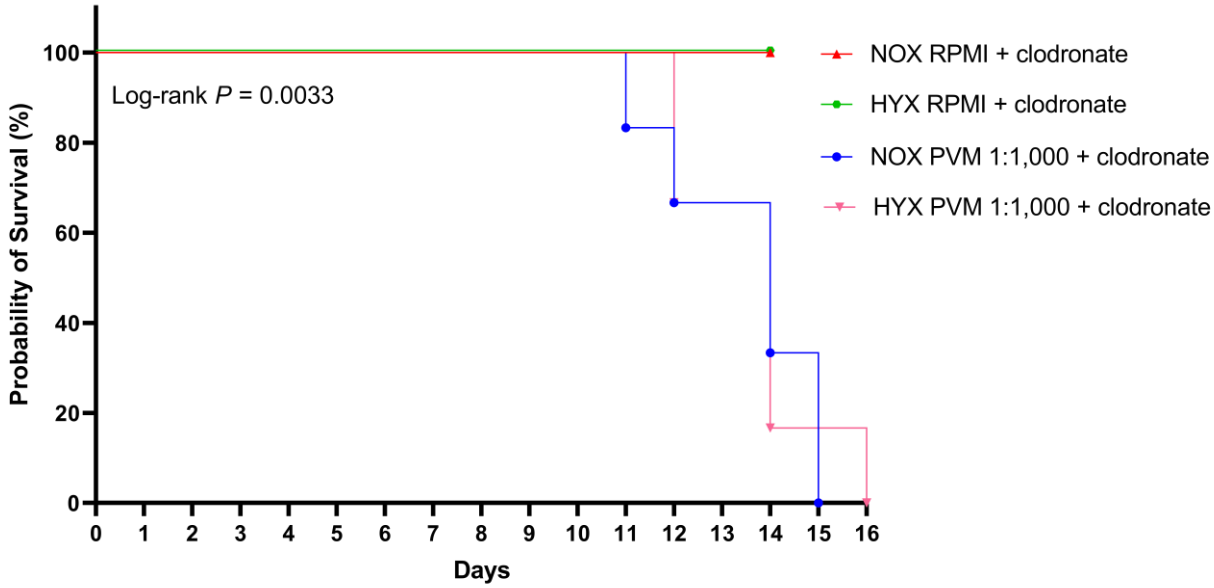

Figure 21. Probability of survival of neonatal mice treated with clodronate liposomes under normoxic and hyperoxic conditions following PVM or RPMI administration.

Kaplan–Meier survival curves for neonatal mice exposed from birth to normoxia (NOX; 21% O_2) or hyperoxia (HYX; 85% O_2). Tissue-resident alveolar macrophages were depleted via intranasal administration of clodronate liposomes on postnatal day (P)3, P6, P9, P12, and P15. On P4, mice were infected intranasally with pneumonia virus of mice (PVM) 1:1,000 dilution in RPMI or received RPMI alone as a control. Each line represents an experimental group (n = 6, per group). The statistical analysis was performed using the Mantel–Cox (log-rank) test to compare survival across all four experimental groups.

4.16. Histological analysis of lung tissue following macrophage depletion, normoxia or hyperoxia exposure, and PVM infection in neonatal mice

Detailed histological evaluation of H&E-stained lung sections revealed distinct structural alterations across experimental conditions involving macrophage depletion, oxygen exposure, and PVM infection. In the normoxia-exposed, macrophage-depleted group, alveolar architecture was largely preserved, with thin, regular septa, open airspaces, and minimal inflammatory infiltrate, indicating intact lung structure in the absence of infection or oxygen stress. Hyperoxia-exposed lungs with macrophage depletion exhibited mild alveolar simplification, characterized by enlarged airspaces, thinning of alveolar walls, and modest reduction in alveolar complexity, consistent with hyperoxic injury that appeared partially attenuated by the absence of macrophages. In contrast, both PVM-infected groups with macrophage depletion showed markedly increased histopathological damage. These lungs displayed substantial thickening of the alveolar septa, perivascular and interstitial inflammatory cell infiltration. The most pronounced injury occurred in the hyperoxia-infected, clodronate-treated group, where widespread architectural disruption, diffuse alveolar damage, pronounced inflammatory cell infiltration within the interstitium, and around blood vessels were observed (**Figure 22**). These findings indicate that while macrophage depletion under sterile conditions may protect to some extent against hyperoxic structural injury, it leads to overwhelming, uncontrolled inflammation and tissue destruction upon PVM infection, particularly in combination with hyperoxic stress.

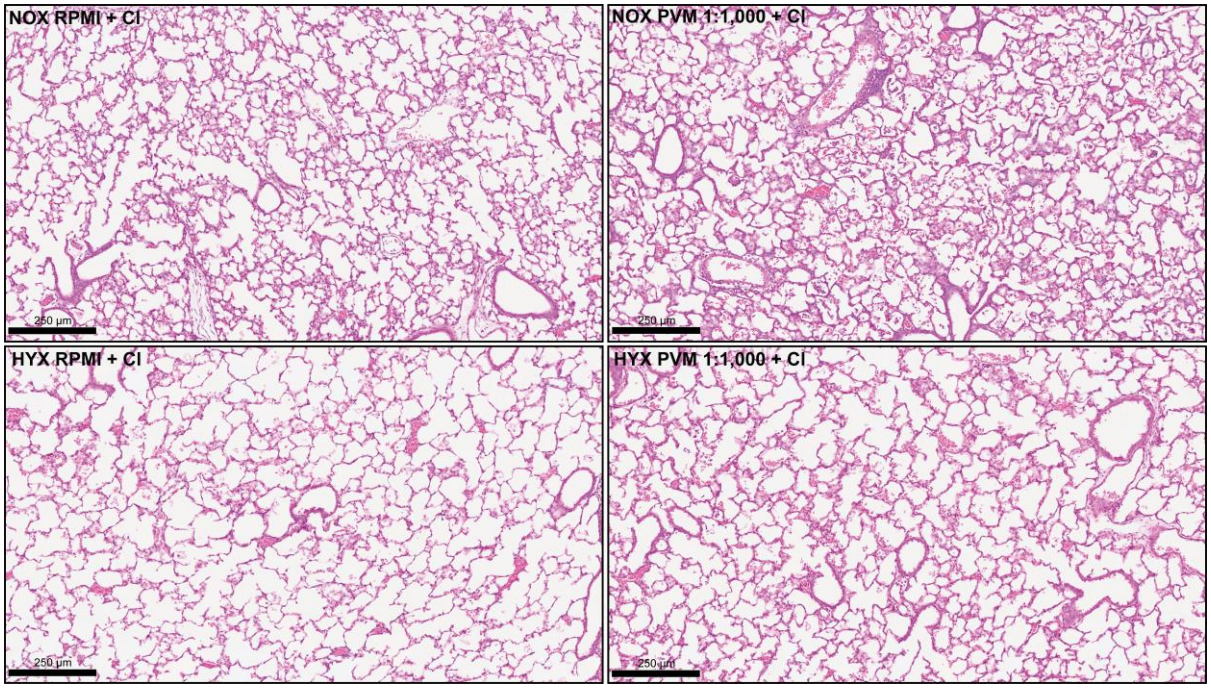

Figure 22. Histological analysis of lung tissue treated with clodronate liposomes under normoxic and hyperoxic conditions following PVM or RPMI administration.

Representative hematoxylin and eosin (H&E)-stained lung sections from neonatal mouse pups exposed to (NOX; 21% O_2) or hyperoxia (HYX; 85% O_2) from birth. All groups received intranasal clodronate liposomes (Cl) administration on postnatal days (P)3, P6, and P9. On P4, pups were intranasally administered either pneumonia virus of mice (PVM) diluted 1:1,000 in RPMI medium or RPMI medium alone as a control. Lungs were harvested on P11, paraffin-embedded, sectioned, stained with H&E, and scanned. Images were acquired at 10× magnification.

4.17. Effect of macrophage depletion combined with PVM infection on hyperoxia- and normoxia-induced respiratory dysfunction in neonatal mice

Neonatal mice were exposed from birth to either normoxia (21% O_2) or hyperoxia (85% O_2). Tissue-resident alveolar macrophages were depleted by intranasal administration of clodronate liposomes on P3, P6, and P9. On P4, mice were infected intranasally with PVM 1:1,000 dilution, and lung function was assessed on P11 using whole-body plethysmography.

Whole-body plethysmography revealed that neonatal mice treated with both PVM infection and macrophage depletion exhibited a significant exacerbation of lung function impairment under hyperoxic conditions compared to normoxia. Specifically, tidal volume, expiratory volume, and minute volume were all significantly lower in the

hyperoxia-infected and clodronate-treated group (HYX PVM 1:1000 + Cl) compared to the normoxia-infected and clodronate-treated group (NOX PVM 1:1000 + Cl), indicating that macrophage depletion further amplifies the deleterious effects of hyperoxia during viral infection (**Figure 23A-C**). Breathing frequency was significantly reduced in the hyperoxia group (**Figure 23D**). Expiratory time was markedly prolonged under hyperoxia compared to normoxia, while inspiratory time showed a trend toward prolongation in the hyperoxic group, though this did not reach statistical significance (**Figure 23E-F**). Together, these findings demonstrate that macrophage depletion in the context of PVM infection leads to notable lung function decline, with hyperoxia exacerbating these effects on both ventilatory volumes and respiratory timing. This highlights a critical protective role of tissue-resident alveolar macrophages in preserving respiratory function and rhythm during early-life viral infection, particularly under hyperoxic stress.

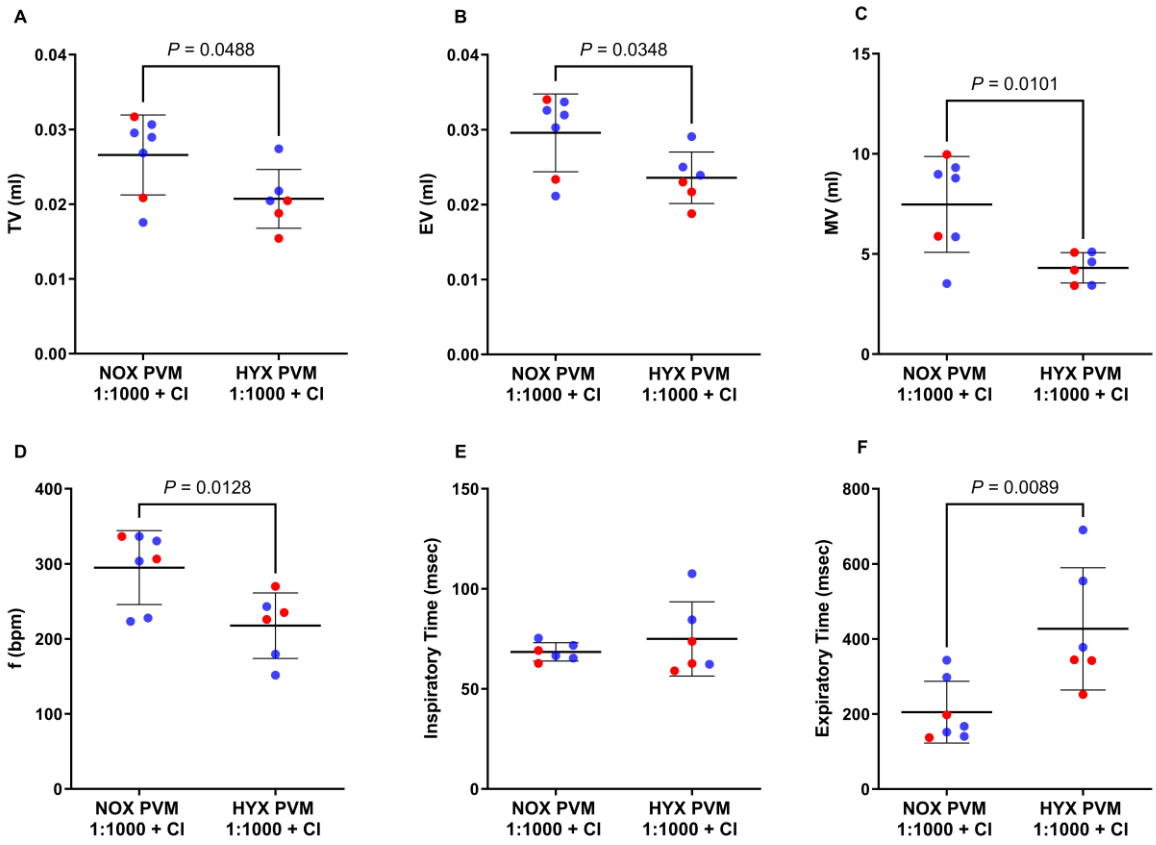

Figure 23. Effect of PVM infection in combination with macrophage depletion on lung physiology in neonatal mice.

Mice were exposed to normoxia (NOX; 21% O_2) or hyperoxia (HYX; 85% O_2) from birth, and administered intranasally pneumonia virus of mice (PVM) 1:1,000 at postnatal day (P)4. Tissue-resident alveolar macrophages were depleted by intranasal administration of clodronate liposomes (Cl) on P3, P6, and P9. At P11, whole-body plethysmography was assessed. Data are presented as mean ± SD (n=6-7, per group). Statistical analysis was performed using one-way ANOVA with Tukey's post hoc test. Red dots indicate female mice, and blue dots indicate male mice.

4.18. Viral load dynamics in normoxia- and hyperoxia-exposed mice infected with PVM with and without macrophage depletion

The viral load of PVM was assessed in neonatal mice exposed from birth to either normoxia (21% O_2) or hyperoxia (85% O_2), and infected intranasally on P4 with PVM at a 1:1,000 dilution. Tissue-resident alveolar macrophages were depleted by intranasal administration of clodronate liposomes on P3, P6, and P9. On P11, the left lung lobe was harvested for RNA extraction and cDNA synthesis. Quantitative analysis revealed no significant differences in viral load between normoxia- and hyperoxia-exposed, PVM-infected mice at P11. However, macrophage depletion led to a significant reduction in viral load in both normoxia and hyperoxia-infected and

clodronate-treated groups. The greatest reduction in viral load was observed in the hyperoxia-infected, clodronate-treated group. Notably, a significant difference was observed between normoxia infected group and normoxia infected, clodronate-treated group (**Figure 24**). The reduced viral load observed in clodronate-treated mice may be explained by the depletion of tissue-resident alveolar macrophages, which likely serve as a reservoir for PVM replication in the neonatal lung.

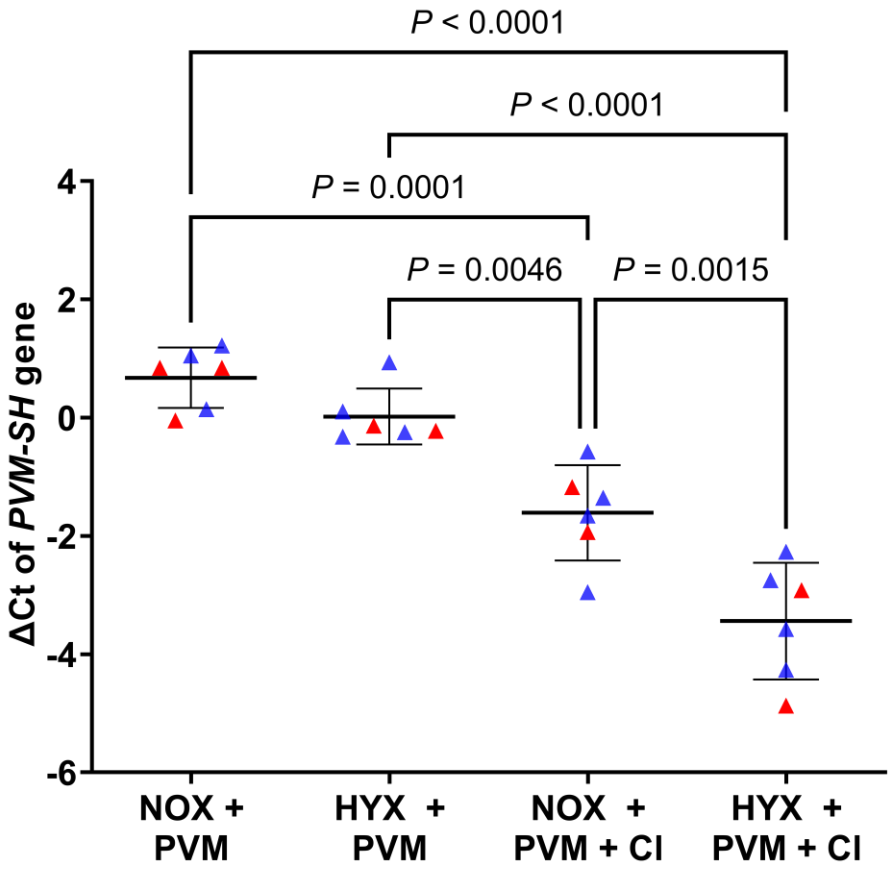

Figure 24. Effect of macrophage depletion on PVM viral load in normoxia- and hyperoxia-exposed neonatal mice.

Newborn mice were exposed from birth to either normoxia (NOX; 21% O_2) or hyperoxia (HYX; 85% O_2), and infected intranasally with pneumonia virus of mice (PVM) 1:1,000 dilution on postnatal day (P)4. Two groups received intranasal clodronate liposomes (Cl) on P3, P6, and P9 to deplete tissue-resident alveolar macrophages. Expression of the *PVM-SH* protein gene was quantified, with *PolR2a* used as the reference gene. Data represent mean ± SD (n=6, per group). Each dot represents an individual animal, with red indicating females and blue indicating males. Statistical significance between groups was determined using one-way ANOVA followed by Tukey's *post hoc* test.

4.19. Impact of PVM Infection in combination with macrophage depletion on lung protein expression in neonatal mice

To investigate the impact of hyperoxia on lung protein expression during PVM infection with tissue-resident alveolar macrophage depletion, neonatal mice were exposed from birth to normoxia (21% O_2) or hyperoxia (85% O_2), or infected with PVM, and treated with clodronate liposomes. Lung tissue collected at P11 was analyzed by antibody microarray. Compared to normoxic, infected, and macrophage-depleted controls, hyperoxia-exposed, infected mice displayed pronounced changes in proteins involved in immune activation (for example, upregulation of CCL25, CD53, CD27), tissue remodeling and epithelial barrier function (elevated BMP5, BMP6, and MUC1), metabolic or anti-inflammatory adaptation (increased adiponectin), and modulation of factors involved in growth signaling and innate immunity (INHBA, IL5, CD14, CD69). Notably, the reverse comparison, normoxia versus hyperoxia in the context of infection and clodronate-mediated macrophage depletion, showed no differentially abundant proteins, highlighting the uniquely profound proteomic reprogramming induced by hyperoxic stress (**Figure 25**). Importantly, both normoxia-infected, clodronate-treated, and hyperoxia-infected and clodronate-treated groups exhibited complete mortality by P15 and P16, respectively, indicating that depletion of tissue-resident alveolar macrophages is sufficient to phenocopy the lethal effect of hyperoxia during viral infection. Thus, the proteomic signatures observed at P11 capture molecular changes preceding terminal lung injury and demonstrate that, while hyperoxia drives unique lung remodeling and immune activation, loss of alveolar macrophages alone under normoxic conditions can recapitulate the severe, fatal phenotype seen with hyperoxia during PVM infection.

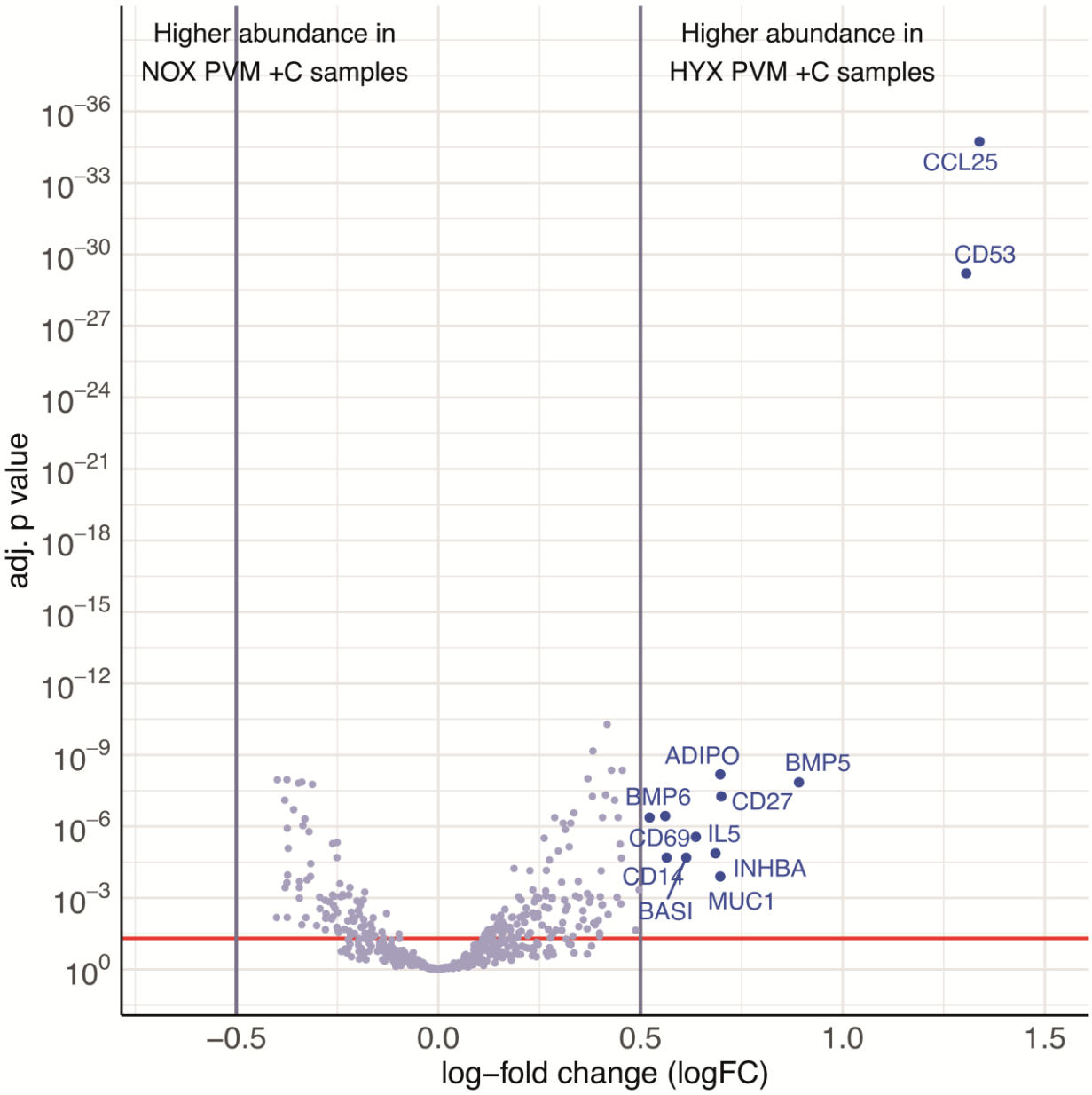

Figure 25. Differential protein expression between NOX PVM + clodronate and HYX PVM + clodronate samples visualized by volcano plot.

Volcano plot visualising the differences in abundance between normoxia (NOX; 21% O_2), pneumonia virus of mice (PVM) infected and clodronate (C)-treated or hyperoxia (HYX; 85% O_2), PVM-infected and C-treated samples as log-fold changes (logFC) and their corresponding *P* values (adj. for multiple testing). The red line indicates a significance level of adjusted *P* value = 0.05, vertical lines indicate the logFC cutoffs of ±0.5. A positive logFC indicates higher abundance in HYX PVM +C samples, a negative logFC in NOX PVM +C samples. Differential proteins (|logFC| > 0.5, adjusted *P* value < 0.05) are indicated by labeled blue text on the plot.

4.20. Differential protein expression in normoxic neonatal mouse lungs following PVM infection and macrophage depletion

To investigate how PVM infection alters lung protein expression in the absence of alveolar macrophages, neonatal mice were maintained under normoxic conditions and administered either PVM or RPMI medium intranasally on P4. To deplete tissue-resident alveolar macrophages, pups in the infected group received clodronate liposome treatment on P3, P6, and P9. Lung tissues were collected on P11, and protein expression profiles were assessed using antibody microarrays, as previously described.

Analysis revealed that uninfected control lungs (NOX RPMI) showed higher abundance of proteins involved in homeostasis and immune regulation, including CD4, CD3δ, IL1β, IL9, IL25, VEGFC, FGF2, and an array of chemokines such as CCL7, CCL8, CCL25, MCP, CCL15, and CCL26. This protein signature indicates a coordinated, balanced immune response where both innate and adaptive mechanisms contribute to tissue protection and repair, aligning with the observed full survival in this group. In contrast, PVM-infected, macrophage-depleted lungs (NOX PVM + C), which exhibited complete mortality by P15, exhibited substantial upregulation of pro-inflammatory and cytotoxic mediators. These included CCL5, CCL20, IL8, IL15, CD8A, CD28, ADAM8, VEGFR2, ITGA5, CD44, HLA molecules, and SDF1. Proteins associated with Th17-skewed immunity, cytotoxic T cell activation, and tissue fibrosis were notably increased, along with elevated anti-inflammatory mediators such as IL10 and TGFβ isoforms (**Figure 26**). This expression pattern points to a state of unresolved inflammation, immune dysregulation, and progressive tissue damage, underscoring the pathological consequences of macrophage depletion during early-life viral infection.

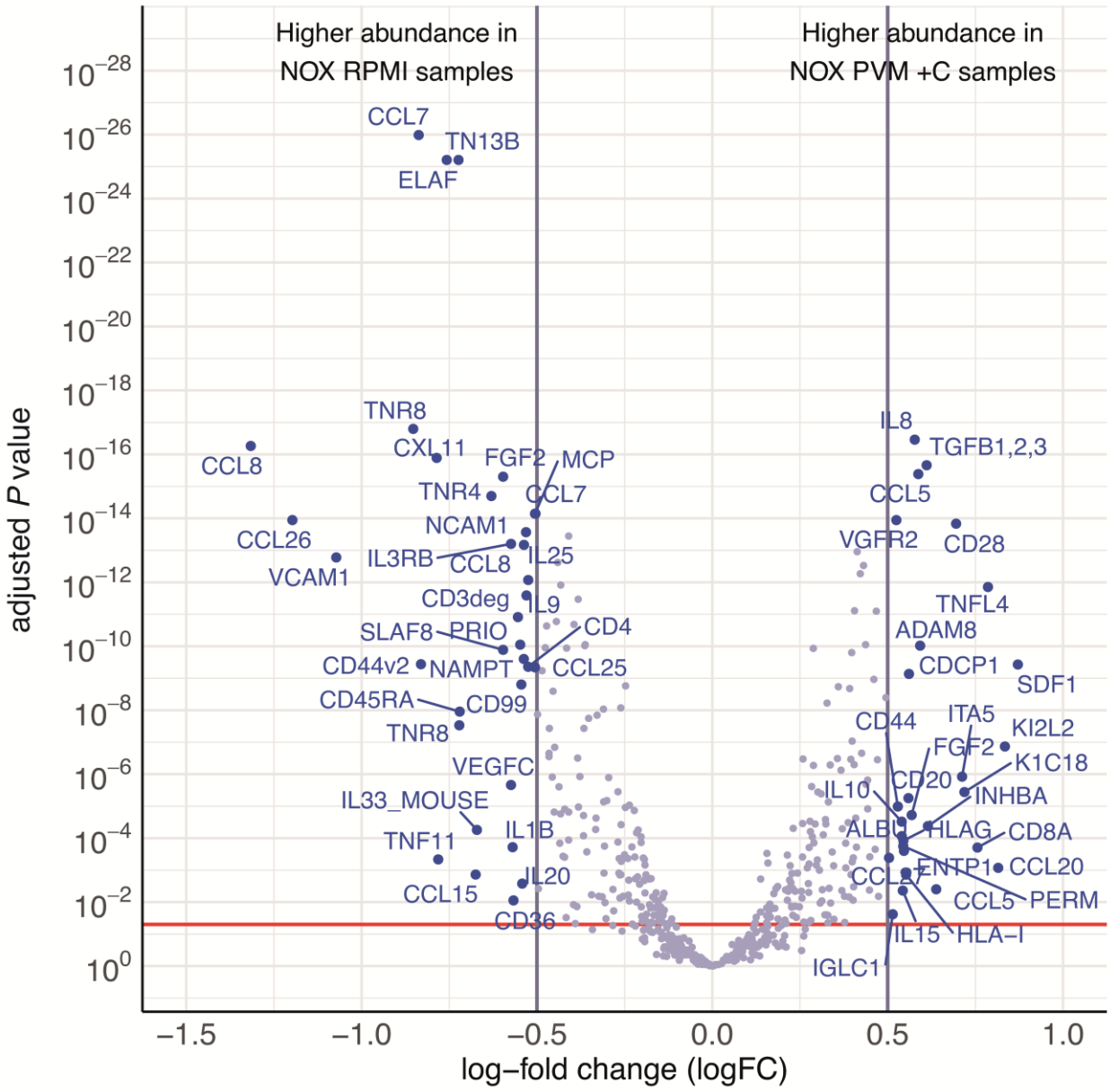

Figure 26. Differential protein expression between NOX RPMI and NOX PVM + CI samples visualized by volcano plot.

Volcano plot visualising the differences in abundance between NOX PVM + C samples and NOX RPMI samples as log-fold changes (logFC) and their corresponding *P* values (adjusted for multiple testing). The red line indicates a significance level of adjusted *P* value = 0.05, vertical lines indicate the logFC cutoffs of ±0.5. A positive logFC indicates higher abundance in NOX PVM +C samples, a negative logFC in NOX RPMI samples. Differential proteins (|logFC| > 0.5, adjusted *P* value < 0.05) are indicated by labeled blue text on the plot.

4.21. Pathway enrichment analysis highlights distinct immune regulation in neonatal lungs after PVM Infection and macrophage depletion

To better understand the functional implications of the observed protein expression differences, a Metascape pathway enrichment analysis was performed on proteins that were differentially abundant between the NOX RPMI and NOX PVM + C groups. In the NOX RPMI group, proteins more abundantly expressed in the absence of infection were enriched in biological pathways related to immune regulation, tissue stability, and postnatal lung development. Prominent enriched terms included cytokine-cytokine receptor interaction, leukocyte migration regulation, interleukin signaling, positive regulation of the ERK1/ERK2 cascade, glial cell activation, and adaptive immune responses. These findings suggest a well-organized immune environment that supports tissue integrity and effective host defense without excessive immune activation. Additional enrichment in processes such as regulation of wound response, blood pressure, and protein complex assembly further reflects established homeostasis in the neonatal lung under normoxic conditions. In contrast, proteins upregulated in the NOX PVM + C group revealed enrichment in pathways characteristic of heightened inflammation, immune cell recruitment, and fibrotic remodeling. Key pathways included cytokine-cytokine receptor interaction, chemotaxis, and rheumatoid arthritis, reflecting strong immune activation in the absence of alveolar macrophages during PVM infection. Processes such as hyaluronan metabolism, positive regulation of leukocyte apoptotic process, and cell development indicated ongoing tissue remodeling and immune dysregulation. Enhanced signaling via TGFBR3, hematopoietic lineage pathways, and somatic recombination-based adaptive responses reflected an activated immune landscape coupled with tissue remodeling and fibrosis-like responses (**Figure 27**). These findings are consistent with the histopathological indicators of inflammation and lung injury observed in this group. Together, these contrasting enrichment profiles highlight the critical role of alveolar macrophages in regulating immune responses during early-life viral infection. In their presence, immune signaling remains balanced and tissue integrity is preserved. In contrast, the absence of alveolar macrophages leads to heightened immune activation, inflammatory tissue remodeling, and an overall increase in disease severity and mortality following PVM infection.

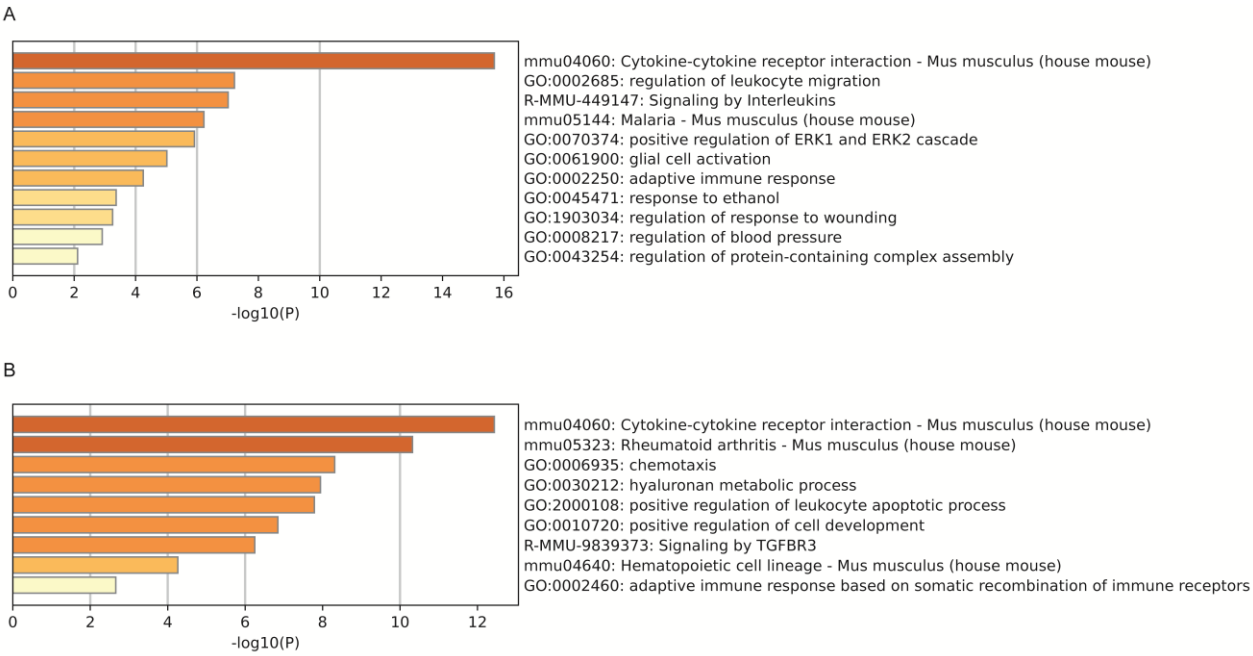

Figure 27. Pathway enrichment analysis of differentially abundant proteins in normoxic neonatal mouse lungs following PVM infection and macrophage depletion.

Bar plots display the top enriched pathways and biological processes identified by Metascape, based on proteins more highly expressed between (A) normoxia (NOX; 21% O_2) RPMI and (B) NOX pneumonia virus of mice (PVM) + clodronate (Cl) groups at postnatal day (P)11. The x-axis represents statistical significance as $-\log_{10}$(adjusted *P* value). The most significantly enriched terms are shown in darker orange. NOX RPMI (upper panel) and NOX PVM + Cl (lower panel).

4.22. Principal component analysis of differentially expressed lung proteins

Principal component analysis (PCA) of differential lung protein expression across all six experimental groups revealed that normoxic PVM infection with tissue-resident alveolar macrophage depletion (NOX_PVM_C) generates a lung proteome profile that is markedly distinct from other normoxic conditions and is positioned much closer to the hyperoxic PVM-infected (HYX_PVM) group in PCA space. This spatial proximity in the PCA plot indicates that NOX_PVM_C phenocopies HYX_PVM at the proteomic level, with both groups displaying similarly altered protein expression patterns not observed in control or less severely affected groups (**Figure 28**). The functional significance of this phenocopy is emphasized by the fact that all mice in both NOX_PVM_C and HYX_PVM groups succumbed by the end of the observation period, underscoring equivalent and severe disruption of pulmonary homeostasis.

Despite the partial phenotypic overlap, each experimental group remains molecularly distinct, as evident from their discrete PCA clustering. This demonstrates that while

hyperoxic stress and macrophage depletion during viral infection can independently drive the lung into a vulnerable state, the underlying molecular responses retain unique elements specific to each insult. These PCA results, together with the volcano plot and pathway enrichment data, highlight that alveolar macrophage depletion in normoxic, PVM-infected neonatal mice is sufficient to recapitulate key features of the hyperoxic infection response, supporting a model in which either stressor disrupts critical defense and repair pathways, leading to lethality.

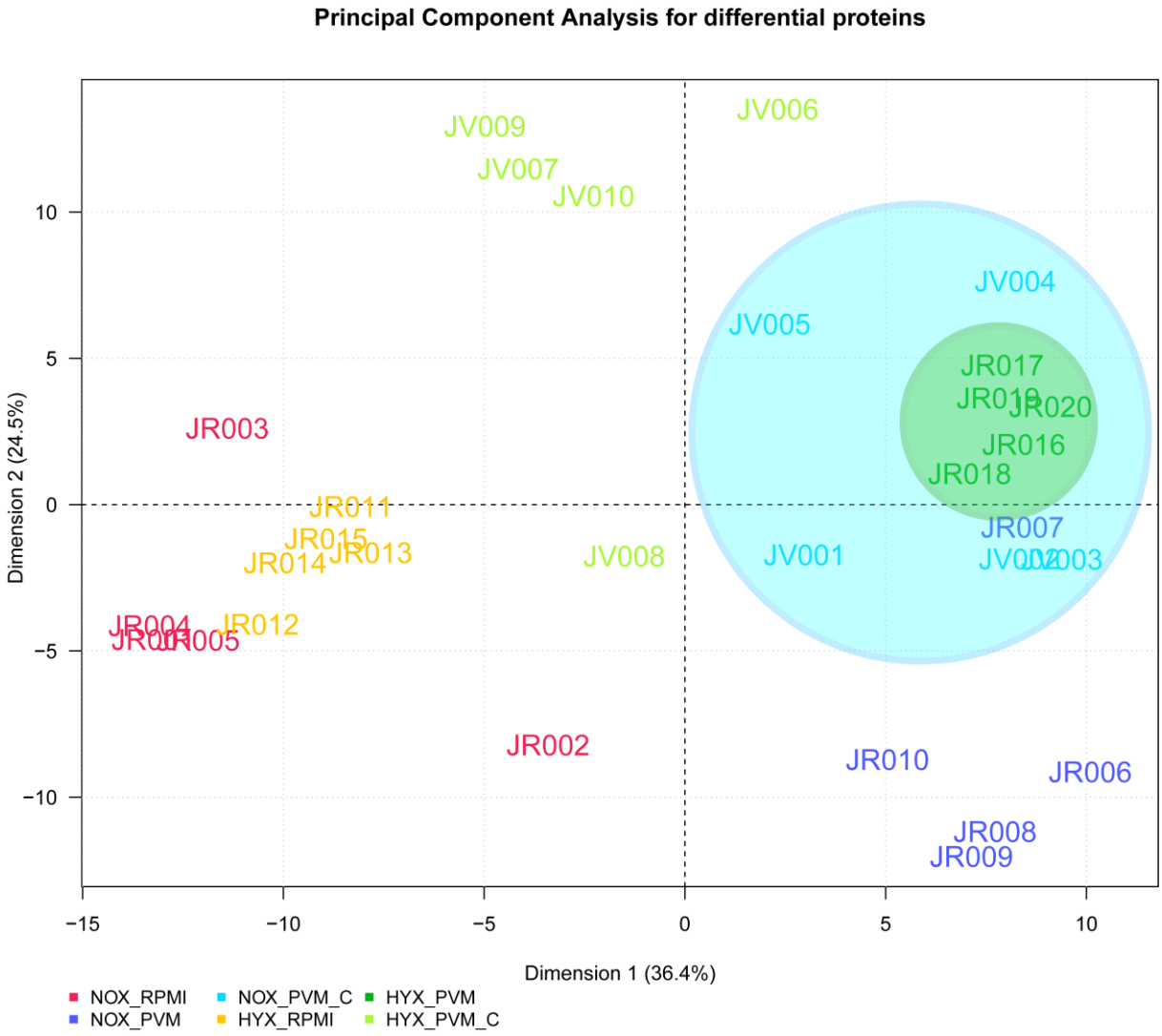

Figure 28. Continued overleaf

Figure 28. Principal Component Analysis for differential proteins.

Neonatal mice were exposed from birth to either normoxia (NOX; 21% O_2) or hyperoxia (HYX; 85% O_2). Tissue-resident alveolar macrophages were depleted by intranasal administration of clodronate liposomes on postnatal day (P)3, P6, and P9. On P4, pups were intranasally administered either pneumonia virus of mice (PVM) diluted 1:1,000 in RPMI medium or RPMI medium alone as a control. Scatter plot displays the first two principal components of the samples' protein signal data based on differentially abundant proteins. The percentages given in the axis labels describe the ratio of total variance explained by the respective principal component. Samples are color-coded by experimental condition: red, NOX RPMI control (NOX_RPMI); light blue, NOX, pneumonia virus of mice (PVM)-infected, clodronate (C)-treated (NOX_PVM_C); dark green, HYX, PVM-infected (HYX_PVM); dark blue, NOX, PVM-infected (NOX_PVM); yellow, HYX, RPMI control (HYX_RPMI); light green, HYX PVM-infected, C-treated (HYX_PVM_C). The circles highlight the spatial proximity and similarity between the NOX_PVM_C and HYX_PVM sample groups; the dark green circle encompasses HYX_PVM samples, and the light blue circle encompasses NOX_PVM_C samples. The overlap and closeness of these circles in principal component space indicate that these two groups share similar overall protein expression profiles.

5. Discussion

Preterm birth remains a dominant contributor to global neonatal morbidity and mortality. Affecting approximately 13.4 million infants annually worldwide, complication of preterm birth remain the leading cause of death in children younger than 5 years, accounting for nearly 1 million deaths each year (143). Among these vulnerable neonates, those born extremely preterm (<28 weeks of gestation) during the late canalicular or early saccular stage of lung development face the greatest burden of BPD. Preterm infants commonly require respiratory interventions after birth, including supplemental oxygen therapy, mechanical ventilation, and CPAP. While these interventions are essential for survival, they contribute to the development of chronic respiratory disease and its lifelong effects (144). Preterm birth severely impairs lung development, leading to alveolar simplification and arrested alveolarization. At the same time, the preterm infant's immune system remains notably underdeveloped and immature (4). This developmental vulnerability leaves the newborn extremely sensitive to environmental insults such as respiratory viruses, where, among preterm patients with severe respiratory infections, RSV emerges as the most frequently identified pathogen. Children with BPD demonstrate a 12 times higher risk of RSV hospitalisation compared with term-born babies, with substantially longer hospital stays and greater intensive care unit admission rates (93, 94).

This study employed a neonatal murine model subjected to sustained hyperoxia (85% O_2) and subsequent PVM infection to elucidate the interplay between oxygen-induced pulmonary injury and antiviral immune response.

5.1. Hyperoxia effects on lung structure, survival, and dose-dependent interactions with viral infection

Hyperoxia alone induced profound structural changes characteristic of arrested lung development, recapitulating the alveolar simplification seen in BPD. Continuous exposure to 85% O_2 from birth resulted in enlarged alveolar spaces and reduced septation across all hyperoxia-exposed groups, regardless of infection status, demonstrating that supraphysiologic oxygen concentrations are sufficient to disrupt normal alveologenesis (145). Despite this pronounced architectural disruption, hyperoxia alone was remarkably non-lethal, with 100% survival observed in all

hyperoxia control groups throughout the study period. This finding, severe structural injury without mortality, aligns with clinical observations that preterm infants can survive prolonged oxygen therapy but develop chronic lung disease and other lifelong impairments (146). However, when combined with PVM infection, hyperoxia transformed from a developmentally disruptive but survivable insult into a lethal condition, with complete mortality observed by P12 at the highest viral load (1:1,000 dilution). Strikingly, this hyperoxia-virus interaction demonstrated clear dose-dependency, with intermediate mortality at 1:2,500 PVM dilution and reduced but still notable mortality at 1:5,000 dilution, while normoxia-exposed mice infected at corresponding viral loads showed either delayed onset mortality (80% survival at 1:2,500) or complete survival (1:5,000). The dose-response pattern indicates that under hyperoxia, there is a threshold beyond which the lung's ability to control viral infection steadily weakens as the viral dose rises.

5.2. Impact of hyperoxia on neonatal lung function and viral load dynamics: inflammation-driven pathogenesis independent of viral replication

Hyperoxia exposure profoundly disrupted respiratory mechanics in neonatal mice, producing dose-dependent impairments that were dramatically exacerbated by concurrent viral infection. Continuous oxygen exposure alone significantly reduced tidal volume, expiratory volume, and minute volume compared to normoxic controls, while prolonging both inspiratory and expiratory times, indicating fundamental alterations in respiratory rhythm. These functional deficits aligned with established literature demonstrating that severe neonatal hyperoxia (≥80% O_2) increased airway resistance and lung compliance due to alveolar simplification, increased collagen deposition, and increased interstitial thickness (147, 148).

When hyperoxia was combined with PVM infection, respiratory dysfunction was most pronounced, with the lowest tidal and minute volume values observed across all experimental groups, reflecting synergistic impairment of both gas exchange and ventilatory control mechanisms. Remarkably, despite this severe physiological compromise, qPCR analysis revealed no consistent elevation in viral load between hyperoxia and normoxia groups. At P7, normoxia-infected mice transiently displayed significantly higher PVM viral RNA levels than hyperoxia-infected mice. The finding that hyperoxia amplifies disease severity without boosting viral replication parallels clinical evidence indicating that children with mild RSV infection, assessed in

outpatient settings, exhibited significantly higher viral loads compared to hospitalized patients. Importantly, the peak viral load occurred before the peak of clinical disease severity and was inversely associated with the severity of clinical outcomes (79). The qPCR data further demonstrated temporal viral load dynamics, with both oxygen conditions showing significant increases from P5 to P10, but the magnitude of viral burden did not correlate with survival outcomes. Gene expression analysis revealed complementary patterns, with hyperoxia-specific upregulation of inflammatory markers including *Ccl2*, *Cxcl10*, and *Ccl3* from as early as postnatal day 5, while viral-responsive genes like *Ccl5* peaked in normoxic infected mice at postnatal day 7. These findings collectively demonstrate that hyperoxia-induced virus lethality stems primarily from dysregulated host inflammatory responses and compromised lung mechanics rather than enhanced viral replication, supporting a model wherein oxygen injury primes the immature lung for catastrophic immune-mediated tissue damage upon viral challenge.

5.3. Synergistic impact of hyperoxia and pneumonia virus infection on lung inflammation: Th17 skewing, cytokine storm, and fibrotic remodeling

Protein expression analysis revealed that normoxic PVM infection triggered a robust but balanced antiviral response characterized by elevated IL-6, IL-8, IL-10, IL-17C, CCL5, and CXCL13. This profile aligns with studies demonstrating that PVM infection in immunocompetent mice generates significant but survivable inflammation with widespread intra-alveolar and interstitial infiltrates consisting predominantly of neutrophils and macrophages (149). The transient nature of these responses in our model, with full recovery observed by P21 in similar studies, underscores the lung's capacity to resolve viral inflammation when immune homeostasis remains intact (122).

The combination of hyperoxia and PVM infection transformed individually manageable insults into a uniformly lethal condition, with 100% mortality observed by P12. This synergistic lethality cannot be explained by enhanced viral replication, as PVM viral loads were not increased. Instead, the data point toward a host-mediated pathological response where hyperoxia-induced immune dysfunction creates a permissive environment for uncontrolled inflammation upon viral challenge (150).

Protein microarray analysis revealed that hyperoxia-infected lungs exhibited the most severe inflammatory signature among all experimental groups. This included

marked elevation of CCL17, CCL20, and IL-15, indicating a shift toward Th17-skewed immunity and fibrotic remodelling. The prominence of CCL20 is particularly significant, as this chemokine specifically recruits Th17 cells and is strongly associated with neutrophilic inflammation and tissue damage in various lung diseases. Pathway enrichment analysis confirmed this inflammatory shift, with cytokine-cytokine receptor interactions representing the most significantly enriched pathway in both normoxic and hyperoxic infected conditions. In hyperoxic conditions specifically, additional overrepresentation of pathways related to lymphocyte migration, leukocyte cell–cell adhesion regulation, and fibrotic tissue remodeling, most notably, heightened enrichment of the lung fibrosis pathway, demonstrated the amplified and dysregulated nature of the immune response. IL-17 signaling, enriched in pathway analysis, promotes neutrophil recruitment and activation while stimulating production of additional inflammatory mediators, including IL-6, IL-8, and GM-CSF (151). The dysregulated TGF-β signaling observed in hyperoxia-infected mice likely contributes to impaired immune resolution and promotes pathological tissue remodeling characteristic of severe lung injury.

5.4. Immune cell dynamics: from homeostasis to chaos

Flow cytometry revealed profound alterations in immune cell populations under hyperoxic stress, particularly when combined with viral infection. Hyperoxia alone reduced TR-AMs while expanding exudative macrophages, DCs, and neutrophils. This shift reflects the known vulnerability of TR-AMs to oxidative stress, as these cells rely predominantly on oxidative phosphorylation within their high-oxygen, low-glucose alveolar niche (152).

To gain deeper insight into these population changes at the cellular level, we employed single-cell RNA sequencing to characterize immune cell heterogeneity. We identified distinct macrophage subsets with specific roles: AM_HYX cells represent stress-adapted macrophages specialized for coping with oxidative stress, and AM_PVM cells emerge as virus-responsive macrophages during infection. Under normoxic conditions, homeostatic AM_1 cells can differentiate toward AM_HYX under oxidative stress or toward AM_PVM upon viral infection. When hyperoxia was combined with PVM infection, the immune landscape underwent further dramatic changes, with single-cell analysis demonstrating a complete loss of protective alveolar macrophage populations and their replacement by inflammatory cell types.

Specifically, we observed the disappearance of both AM_HYX and AM_PVM populations, replaced by four distinct dendritic cell subsets. This dendritic cell expansion aligns with studies showing that early-life hyperoxia induces Flt3L-dependent proliferation of CD103+ DCs, a growth factor-mediated process that drives dendritic cell development, which becomes hyper-responsive to viral challenge (153).

This cellular reprogramming represents a fundamental breakdown of normal immune development with devastating functional consequences. The emergence of multiple dendritic cell subsets in hyperoxia-infected mice reflects the lung's attempt to compensate for lost macrophage functions through enhanced antigen presentation capabilities. However, these dendritic cells appear maladapted for the regulatory needs of the neonatal lung. Unlike the immunoregulatory alveolar macrophages they replace, these dendritic cells are programmed to drive robust immune activation, making them poorly suited for maintaining the delicate balance between pathogen clearance and tissue protection required in the developing lung. This mismatch between cellular function and tissue needs likely underlies the excessive inflammation and poor outcomes observed in hyperoxia-infected neonates. This finding aligns with studies showing that early-life hyperoxia permanently alters DC function, making them hyperresponsive to subsequent challenges (153).

5.5. Hyperoxia disrupts normal T cell responses to viral challenge

Under normoxic conditions, PVM infection triggered a robust T cell response, with both CD4+ and CD8+ T cell numbers increasing significantly by P7 and persisting through to day 10. This response aligns with established literature showing that acute PVM infection in C57BL/6 mice is associated with a large influx of activated CD4+ and CD8+ T cells into the lung (154). The functional importance of this response is well-documented, as T cell-deficient mice fail to eliminate PVM and become virus carriers (149).

In contrast, hyperoxia impaired the normal T cell response to viral infection. While baseline CD4+ and CD8+ T cell populations were unaffected by hyperoxia alone at P4, hyperoxia-exposed mice showed a significantly blunted response to PVM infection. Although hyperoxia-infected mice demonstrated some increase in T cell numbers from their hyperoxia baseline by P7, they failed to achieve the robust T cell expansion seen in normoxic infected mice. This pattern persisted through P10,

indicating that hyperoxia compromises the magnitude of adaptive immune responses to viral challenge. This finding represents a critical departure from normal neonatal immune function. Previous studies demonstrated that infant T cells are developmentally adapted for robust lung immune responses, generating greater numbers of lung-homing effector cells compared to adult T cells. The failure of hyperoxia-exposed neonates to mount this characteristically robust response suggests fundamental disruption of adaptive immunity, likely contributing to the poor viral control and lethal outcomes observed in hyperoxic conditions (155).

5.6. Macrophage depletion reveals critical immunoregulatory function in viral pneumonia

The macrophage depletion experiments provide compelling evidence that TR-AMs serve as essential gatekeepers of immune homeostasis during neonatal viral infection. The dramatic conversion of an otherwise survivable PVM infection into uniformly lethal disease following clodronate treatment represents a striking demonstration of their protective function.

The complete mortality observed in both normoxic and hyperoxic macrophage-depleted, PVM-infected groups (by P15 and P16, respectively) is particularly noteworthy given that clodronate treatment reduced viral load. This outcome strongly implicates immunopathology rather than viral replication as the primary driver of mortality. This finding aligns with observations in adult influenza models, where macrophage depletion leads to lethal disease and possibly reducing normal viral clearance (156), suggesting that alveolar macrophages function as critical brakes on excessive inflammatory responses across different pneumoviral infections and age groups.

Interestingly, our results contrast with some previous studies in adult PVM models, where macrophage depletion prolonged survival (157), likely reflecting age-dependent differences in immune maturation and the critical vulnerability of neonatal hosts to immune dysregulation. The role of alveolar macrophages in pneumoviral infections appears highly context-dependent. While our neonatal PVM model demonstrates their essential protective function, studies with other pneumoviruses have yielded variable results. In adult RSV models, macrophage depletion abolished early inflammatory mediator release but had minimal impact on overall disease severity (158), whereas

depletion in some coronavirus models ameliorated disease by reducing pathological T cell responses (159).

The pronounced septal thickening, dense leukocyte infiltrates, and architectural disruption observed in macrophage-depleted lungs reflect the downstream consequences of losing this immunoregulatory function. The fact that these changes were most severe in the hyperoxia-infected group with clodronate treatment suggests that macrophages become even more critical when the lung faces multiple concurrent stressors. Interestingly, the preservation of alveolar architecture in clodronate-treated but uninfected pups indicates that macrophages are not essential for baseline lung development but become indispensable when immune activation occurs. The exacerbated respiratory dysfunction in macrophage-depleted mice, particularly the profound reductions in tidal volume, minute volume, and breathing frequency, likely reflects both direct inflammatory injury and disrupted control of breathing. The prolonged expiratory times observed in the hyperoxia-infected group with clodronate treatment may indicate airway obstruction from inflammatory exudates or loss of surfactant homeostasis, functions that alveolar macrophages normally help maintain (160).

The antibody microarray data provide mechanistic insights into how macrophage loss drives pathology. The upregulation of chemokines (CCL5, CCL20), cytotoxic T cell markers (CD8A), and fibrotic mediators (TGFB1-3) in depleted lungs suggests a shift toward Th17/Th1-dominated inflammation with excessive tissue remodeling. Perhaps most remarkably, the principal component analysis demonstrates that normoxia-infected and macrophage-depleted lungs cluster closely with hyperoxia-infected lungs, indicating that macrophage loss alone can recapitulate the molecular signature of oxygen toxicity. This finding suggests that much of the hyperoxia-associated vulnerability may stem from macrophage dysfunction rather than direct oxidative injury.

These results have important implications for understanding respiratory viral susceptibility in preterm infants with BPD. The fact that macrophage depletion in normoxia-infected mice phenocopies hyperoxic injury in combination with the virus infection suggests that therapeutic strategies aimed at preserving or restoring alveolar macrophage function could protect against viral pneumonia. This might include approaches to enhance macrophage survival during hyperoxic exposure, promote their proper differentiation, or supplement their immunoregulatory functions through

targeted therapies. The finding that viral load reduction is insufficient to prevent mortality also suggests that antiviral treatments alone may be inadequate in high-risk neonates; combination approaches addressing both viral replication and immune dysregulation may be necessary.

In conclusion, these macrophage depletion experiments establish TR-AMs as essential coordinators of protective immunity in the neonatal lung, functioning not merely as viral targets but as critical regulators that prevent immune-mediated tissue destruction while maintaining effective antiviral responses. The striking similarity between normoxia-infected, macrophage-depleted, and hyperoxia-infected lungs provides novel insights into BPD pathogenesis, revealing that alveolar macrophage dysfunction represents a key mechanistic link between oxygen exposure and increased viral susceptibility in preterm infants.

5.7. Study limitations and future directions

Several limitations of this study must be acknowledged. Our model employed continuous high-concentration oxygen (85% O_2), which may not reflect the variable oxygen exposures common in modern neonatal intensive care. The use of PVM as an RSV surrogate, while well-established, introduces potential species-specific differences in pathogen recognition and response. Additionally, our analysis focused on a single time point for molecular profiling, potentially missing earlier initiating events or later resolution phases. The temporal resolution of our single-cell analysis, while providing valuable snapshots, would benefit from additional time points to better understand the dynamics of cellular reprogramming.

Future investigations should explore dose-response relationships for both oxygen exposure and viral load, better modeling the variable clinical exposures. Genetic approaches using inducible, cell-specific knockout models would provide more definitive evidence for causality. Longitudinal studies tracking survivors into adulthood would illuminate long-term consequences of early immune dysfunction. Finally, therapeutic trials testing macrophage-preserving or immune-modulating interventions could translate these mechanistic insights into clinical benefit.

Given the prominent increase in dendritic cell populations during hyperoxic exposure with or without viral infection, future studies should focus on characterizing the functional phenotype of these dendritic cells in the injured neonatal lung. Investigating whether these cells exhibit enhanced antigen presentation capacity,

inflammatory cytokine secretion, or promote pathogenic T cell responses will be critical. Targeting dendritic cell activation or recruitment might represent a novel therapeutic avenue to dampen inflammation and improve lung repair in neonates exposed to oxygen toxicity and respiratory viral infections. Additionally, dissecting the cross-talk between expanded dendritic cells and depleted alveolar macrophages could provide mechanistic insights into immune imbalance during hyperoxia. Therapies aimed at restoring macrophage-mediated immunoregulation while modulating dendritic cell-driven inflammation may offer more balanced and effective protection against chronic lung disease in preterm infants.

VII Bibliography

1. Herriges M, Morrisey EE. Lung development: orchestrating the generation and regeneration of a complex organ. Development. 2014;141(3):502-13.
2. Morty RE, Konigshoff M, Eickelberg O. Transforming growth factor-beta signaling across ages: from distorted lung development to chronic obstructive pulmonary disease. Proc Am Thorac Soc. 2009;6(7):607-13.
3. Burri PH. Structural aspects of postnatal lung development - alveolar formation and growth. Biol Neonate. 2006;89(4):313-22.
4. Domm W, Misra RS, O'Reilly MA. Affect of early life oxygen exposure on proper lung development and response to respiratory viral infections. Front Med (Lausanne). 2015;2:55.
5. Voelkel NF, MacNee W. Chronic obstructive lung diseases. Hamilton, Ontario: BC Decker Inc.; 2002.
6. Morrisey EE, Hogan BL. Preparing for the first breath: genetic and cellular mechanisms in lung development. Dev Cell. 2010;18(1):8-23.
7. Madurga A, Mizikova I, Ruiz-Camp J, Morty RE. Recent advances in late lung development and the pathogenesis of bronchopulmonary dysplasia. Am J Physiol Lung Cell Mol Physiol. 2013;305(12):L893-905.
8. Caldeira I, Fernandes-Silva H, Machado-Costa D, Correia-Pinto J, Moura RS. Developmental pathways underlying lung development and congenital lung disorders. cells. 2021;10(11).
9. Schittny JC. Development of the lung. Cell Tissue Res. 2017;367(3):427-44.
10. Chawanpaiboon S, Vogel JP, Moller AB, Lumbiganon P, Petzold M, Hogan D, et al. Global, regional, and national estimates of levels of preterm birth in 2014: a systematic review and modelling analysis. Lancet Glob Health. 2019;7(1):e37-e46.
11. Manuck TA, Rice MM, Bailit JL, Grobman WA, Reddy UM, Wapner RJ, et al. Preterm neonatal morbidity and mortality by gestational age: a contemporary cohort. Am J Obstet Gynecol. 2016;215(1):103.e1-.e14.
12. Teune MJ, Bakhuizen S, Gyamfi Bannerman C, Opmeer BC, van Kaam AH, van Wassenaer AG, et al. A systematic review of severe morbidity in infants born late preterm. Am J Obstet Gynecol. 2011;205(4):374.e1-9.

13. Ohuma EO, Moller AB, Bradley E, Chakwera S, Hussain-Alkhateeb L, Lewin A, et al. National, regional, and global estimates of preterm birth in 2020, with trends from 2010: a systematic analysis. Lancet. 2023;402(10409):1261-71.
14. Morniroli D, Tiraferri V, Maiocco G, De Rose DU, Cresi F, Coscia A, et al. Beyond survival: the lasting effects of premature birth. Front Pediatr. 2023;11:1213243.
15. Neu J, Walker WA. Necrotizing enterocolitis. N Engl J Med. 2011;364(3):255-64.
16. Ballabh P. Intraventricular hemorrhage in premature infants: mechanism of disease. Pediatr Res. 2010;67(1):1-8.
17. Cao G, Liu J, Liu M. Global, regional, and national incidence and mortality of neonatal preterm birth, 1990-2019. JAMA Pediatrics. 2022;176(8):787-96.
18. Venkatesan T, Rees P, Gardiner J, Battersby C, Purkayastha M, Gale C, et al. National trends in preterm infant mortality in the United States by race and socioeconomic status, 1995-2020. JAMA Pediatr. 2023;177(10):1085-95.
19. Spong CY. Prediction and prevention of recurrent spontaneous preterm birth. Obstet Gynecol. 2007;110(2 Pt 1):405-15.
20. Stewart A, Graham E. Preterm birth: an overview of risk factors and obstetrical management. Dev Disabil Res Rev. 2010;16(4):285-8.
21. Smith GC, Pell JP, Dobbie R. Interpregnancy interval and risk of preterm birth and neonatal death: retrospective cohort study. BMJ. 2003;327(7410):313.
22. Hediger ML, Scholl TO, Schall JI, Krueger PM. Young maternal age and preterm labor. Ann Epidemiol. 1997;7(6):400-6.
23. Fuchs F, Monet B, Ducruet T, Chaillet N, Audibert F. Effect of maternal age on the risk of preterm birth: a large cohort study. PLoS One. 2018;13(1):e0191002.
24. Goldenberg RL, Hauth JC, Andrews WW. Intrauterine infection and preterm delivery. N Engl J Med. 2000;342(20):1500-7.
25. Medley N, Poljak B, Mammarella S, Alfirevic Z. Clinical guidelines for prevention and management of preterm birth: a systematic review. BJOG. 2018;125(11):1361-9.
26. Shepherd ES, Goldsmith S, Doyle LW, Middleton P, Marret S, Rouse DJ, et al. Magnesium sulfate before preterm birth for neuroprotection: an updated Cochrane systematic review. Obstet Gynecol. 2024;144(2):161-70.
27. Romero R, Yeo L, Chaemsaithong P, Chaiworapongsa T, Hassan SS. Progesterone to prevent spontaneous preterm birth. Semin Fetal Neonatal Med. 2014;19(1):15-26.

28. McDougall ARA, Aboud L, Lavin T, Cao J, Dore G, Ramson J, et al. Effect of antenatal corticosteroid administration-to-birth interval on maternal and newborn outcomes: a systematic review. EClinicalMedicine. 2023;58:101916.
29. Tana M, Tirone C, Aurilia C, Lio A, Paladini A, Fattore S, et al. Respiratory management of the preterm infant: supporting evidence-based practice at the bedside. Children (Basel). 2023;10(3).
30. Fujiwara T, Maeta H, Chida S, Morita T, Watabe Y, Abe T. Artificial surfactant therapy in hyaline-membrane disease. Lancet. 1980;1(8159):55-9.
31. Hohlfeld J, Fabel H, Hamm H. The role of pulmonary surfactant in obstructive airways disease. Eur Respir J. 1997;10(2):482-91.
32. Griese M. Pulmonary surfactant in health and human lung diseases: state of the art. Eur Respir J. 1999;13(6):1455-76.
33. Owen LS, Manley BJ, Davis PG, Doyle LW. The evolution of modern respiratory care for preterm infants. Lancet. 2017;389(10079):1649-59.
34. Diggikar S, Galis R, Nagesh K, Pandita A, Ognean ML, Rudiger M, et al. Surfactant therapy - The conundrum of which infant should be given, when, which drug in what dose via which route of administration? Semin Fetal Neonatal Med. 2024;29(6):101568.
35. Hartel C, Paul P, Hanke K, Humberg A, Kribs A, Mehler K, et al. Less invasive surfactant administration and complications of preterm birth. Sci Rep. 2018;8(1):8333.
36. Flannery DD, O'Donnell E, Kornhauser M, Dysart K, Greenspan J, Aghai ZH. Continuous positive airway pressure versus mechanical ventilation on the first day of life in very low-birth-weight infants. Am J Perinatol. 2016;33(10):939-44.
37. Smolarova S, Kocvarova L, Matasova K, Zibolen M, Calkovska A. Impact of updated European Consensus Guidelines on the management of neonatal respiratory distress syndrome on clinical outcome of preterm infants. Adv Exp Med Biol. 2015;835:61-6.
38. Subramaniam P, Ho JJ, Davis PG. Prophylactic or very early initiation of continuous positive airway pressure (CPAP) for preterm infants. Cochrane Database Syst Rev. 2021;10(10):CD001243.
39. Behnke J, Lemyre B, Czernik C, Zimmer KP, Ehrhardt H, Waitz M. Non-invasive ventilation in neonatology. Dtsch Arztebl Int. 2019;116(11):177-83.

40. Schmidt AR, Ramamoorthy C. Bronchopulmonary dysplasia. Paediatr Anaesth. 2022;32(2):174-80.
41. Bhandari A, Panitch HB. Pulmonary outcomes in bronchopulmonary dysplasia. Semin Perinatol. 2006;30(4):219-26.
42. Northway WH, Jr., Rosan RC, Porter DY. Pulmonary disease following respirator therapy of hyaline-membrane disease. Bronchopulmonary dysplasia. N Engl J Med. 1967;276(7):357-68.
43. Bose CL, Dammann CE, Laughon MM. Bronchopulmonary dysplasia and inflammatory biomarkers in the premature neonate. Arch Dis Child Fetal Neonatal Ed. 2008;93(6):F455-61.
44. Hwang JS, Rehan VK. Recent advances in bronchopulmonary dysplasia: pathophysiology, prevention, and treatment. Lung. 2018;196(2):129-38.
45. Fanaroff AA, Stoll BJ, Wright LL, Carlo WA, Ehrenkranz RA, Stark AR, et al. Trends in neonatal morbidity and mortality for very low birthweight infants. Am J Obstet Gynecol. 2007;196(2):147 e1-8.
46. Nardiello C, Mizikova I, Morty RE. Looking ahead: where to next for animal models of bronchopulmonary dysplasia? Cell Tissue Res. 2017;367(3):457-68.
47. Liu L, Johnson HL, Cousens S, Perin J, Scott S, Lawn JE, et al. Global, regional, and national causes of child mortality: an updated systematic analysis for 2010 with time trends since 2000. Lancet. 2012;379(9832):2151-61.
48. Chan GJ, Lee AC, Baqui AH, Tan J, Black RE. Risk of early-onset neonatal infection with maternal infection or colonization: a global systematic review and meta-analysis. PLoS Med. 2013;10(8):e1001502.
49. Levy O. Innate immunity of the newborn: basic mechanisms and clinical correlates. Nat Rev Immunol. 2007;7(5):379-90.
50. Melville JM, Moss TJ. The immune consequences of preterm birth. Front Neurosci. 2013;7:79.
51. Santos RP, Tristram D. A practical guide to the diagnosis, treatment, and prevention of neonatal infections. Pediatr Clin North Am. 2015;62(2):491-508.
52. Li J, Shen L, Qian K. Global, regional, and national incidence and mortality of neonatal sepsis and other neonatal infections, 1990-2019. Front Public Health. 2023;11:1139832.
53. Liu L, Oza S, Hogan D, Chu Y, Perin J, Zhu J, et al. Global, regional, and national causes of under-5 mortality in 2000-15: an updated systematic analysis with

implications for the Sustainable Development Goals. Lancet. 2016;388(10063):3027-35.
54. Fleischmann-Struzek C, Goldfarb DM, Schlattmann P, Schlapbach LJ, Reinhart K, Kissoon N. The global burden of paediatric and neonatal sepsis: a systematic review. Lancet Respir Med. 2018;6(3):223-30.
55. Seale AC, Blencowe H, Manu AA, Nair H, Bahl R, Qazi SA, et al. Estimates of possible severe bacterial infection in neonates in sub-Saharan Africa, south Asia, and Latin America for 2012: a systematic review and meta-analysis. Lancet Infect Dis. 2014;14(8):731-41.
56. Stoll BJ, Puopolo KM, Hansen NI, Sanchez PJ, Bell EF, Carlo WA, et al. Early-onset neonatal sepsis 2015 to 2017, the rise of Escherichia coli, and the need for novel prevention strategies. JAMA Pediatr. 2020;174(7):e200593.
57. Cotten CM, McDonald S, Stoll B, Goldberg RN, Poole K, Benjamin DK, Jr., et al. The association of third-generation cephalosporin use and invasive candidiasis in extremely low birth-weight infants. Pediatrics. 2006;118(2):717-22.
58. Kelly MS, Benjamin DK, Jr., Smith PB. The epidemiology and diagnosis of invasive candidiasis among premature infants. Clin Perinatol. 2015;42(1):105-17, viii-ix.
59. Weimer KED, Smith PB, Puia-Dumitrescu M, Aleem S. Invasive fungal infections in neonates: a review. Pediatr Res. 2022;91(2):404-12.
60. Pichler K, Assadian O, Berger A. Viral respiratory infections in the neonatal intensive care unit - a review. Front Microbiol. 2018;9:2484.
61. Sanchez Garcia L, Calvo C, Casas I, Pozo F, Pellicer A. Viral respiratory infections in very low birthweight infants at neonatal intensive care unit: prospective observational study. BMJ Paediatr Open. 2020;4(1):e000661.
62. Rodrigo-Munoz JM, Sastre B, Sanchez-Garcia L, Garcia-Garcia ML, Gonzalez-Carrasco E, Fabra C, et al. Filaggrin and cytokines in respiratory samples of preterm infants at risk for respiratory viral infection. Sci Rep. 2022;12(1):21278.
63. Steletou E, Whitley R. Status and future management of congenital cytomegalovirus and neonatal herpes simplex virus infections. Medical Research Archives. 2024;12(11).
64. Kaler J, Hussain A, Patel K, Hernandez T, Ray S. Respiratory syncytial virus: a comprehensive review of transmission, pathophysiology, and manifestation. Cureus. 2023;15(3):e36342.

65. Andeweg SP, Schepp RM, van de Kassteele J, Mollema L, Berbers GAM, van Boven M. Population-based serology reveals risk factors for RSV infection in children younger than 5 years. Sci Rep. 2021;11(1):8953.
66. Reis J, Shaman J. Retrospective parameter estimation and forecast of respiratory syncytial virus in the United States. PLoS Comput Biol. 2016;12(10):e1005133.
67. Papi A, Ison MG, Langley JM, Lee DG, Leroux-Roels I, Martinon-Torres F, et al. Respiratory syncytial virus prefusion F protein vaccine in older adults. N Engl J Med. 2023;388(7):595-608.
68. Farina F, Sannipoli D, Diral E, Mastaglio S, Oltolini C, Dell'Acqua R, et al. Impact of respiratory syncytial virus (RSV) on adult haematology oncology patients. J Infect. 2024;89(6).
69. Curns AT, Rha B, Lively JY, Sahni LC, Englund JA, Weinberg GA, et al. Respiratory syncytial virus-associated hospitalizations among children <5 years old: 2016 to 2020. Pediatrics. 2024;153(3).
70. Li Y, Wang X, Blau DM, Caballero MT, Feikin DR, Gill CJ, et al. Global, regional, and national disease burden estimates of acute lower respiratory infections due to respiratory syncytial virus in children younger than 5 years in 2019: a systematic analysis. The Lancet. 2022;399(10340):2047-64.
71. O'Brien KL, Baggett HC, Brooks WA, Feikin DR, Hammitt LL, Higdon MM, et al. Causes of severe pneumonia requiring hospital admission in children without HIV infection from Africa and Asia: the PERCH multi-country case-control study. The Lancet. 2019;394(10200):757-79.
72. Anderson J, Do LAH, Wurzel D, Quan Toh Z, Mulholland K, Pellicci DG, et al. Severe respiratory syncytial virus disease in preterm infants: a case of innate immaturity. Thorax. 2021;76(9):942-50.
73. Blount RE, Jr., Morris JA, Savage RE. Recovery of cytopathogenic agent from chimpanzees with coryza. Proc Soc Exp Biol Med. 1956;92(3):544-9.
74. Staadegaard L, Caini S, Wangchuk S, Thapa B, de Almeida WAF, de Carvalho FC, et al. Defining the seasonality of respiratory syncytial virus around the world: national and subnational surveillance data from 12 countries. Influenza Other Respir Viruses. 2021;15(6):732-41.
75. Daniels D. A review of respiratory syncytial virus epidemiology among children: linking effective prevention to vulnerable populations. J Pediatric Infect Dis Soc. 2024;13(Supplement_2):S131-S6.

76. Obando-Pacheco P, Justicia-Grande AJ, Rivero-Calle I, Rodriguez-Tenreiro C, Sly P, Ramilo O, et al. Respiratory syncytial virus seasonality: a global overview. J Infect Dis. 2018;217(9):1356-64.
77. Langedijk AC, Bont LJ. Respiratory syncytial virus infection and novel interventions. Nat Rev Microbiol. 2023;21(11):734-49.
78. Brynes A, Williams JV. Small hydrophobic (SH) proteins of Pneumoviridae and Paramyxoviridae: small but mighty. J Virol. 2024;98(9):e0080924.
79. Garcia-Maurino C, Moore-Clingenpeel M, Thomas J, Mertz S, Cohen DM, Ramilo O, et al. Viral load dynamics and clinical disease severity in infants with respiratory syncytial virus infection. J Infect Dis. 2019;219(8):1207-15.
80. Souza AP, Leitao LA, Luisi F, Souza RG, Coutinho SE, Silva JR, et al. Lack of association between viral load and severity of acute bronchiolitis in infants. J Bras Pneumol. 2016;42(4):261-5.
81. Nicholson EG, Schlegel C, Garofalo RP, Mehta R, Scheffler M, Mei M, et al. Robust cytokine and chemokine response in nasopharyngeal secretions: association with decreased severity in children with physician diagnosed bronchiolitis. J Infect Dis. 2016;214(4):649-55.
82. Suleiman-Martos N, Caballero-Vazquez A, Gomez-Urquiza JL, Albendin-Garcia L, Romero-Bejar JL, Canadas-De la Fuente GA. Prevalence and risk factors of respiratory syncytial virus in children under 5 years of age in the WHO European region: a systematic review and meta-analysis. J Pers Med. 2021;11(5).
83. McGinley JP, Lin GL, Oner D, Golubchik T, O'Connor D, Snape MD, et al. Clinical and viral factors associated with disease severity and subsequent wheezing in infants with respiratory syncytial virus infection. J Infect Dis. 2022;226(Suppl 1):S45-S54.
84. Bont L, Versteegh J, Swelsen WT, Heijnen CJ, Kavelaars A, Brus F, et al. Natural reinfection with respiratory syncytial virus does not boost virus-specific T-cell immunity. Pediatr Res. 2002;52(3):363-7.
85. Sande CJ, Mutunga MN, Okiro EA, Medley GF, Cane PA, Nokes DJ. Kinetics of the neutralizing antibody response to respiratory syncytial virus infections in a birth cohort. J Med Virol. 2013;85(11):2020-5.
86. Nyiro JU, Bukusi E, Mwaengo D, Nyaguara A, Nyawanda B, Otieno N, et al. Efficiency of transplacental transfer of respiratory syncytial virus (RSV) specific antibodies among pregnant women in Kenya. Wellcome Open Res. 2022;7:43.

87. Sampah MES, Hackam DJ. Prenatal immunity and influences on necrotizing enterocolitis and associated neonatal disorders. Front Immunol. 2021;12:650709.
88. McLaurin KK, Farr AM, Wade SW, Diakun DR, Stewart DL. Respiratory syncytial virus hospitalization outcomes and costs of full-term and preterm infants. J Perinatol. 2016;36(11):990-6.
89. Escobar GJ, Clark RH, Greene JD. Short-term outcomes of infants born at 35 and 36 weeks gestation: we need to ask more questions. Semin Perinatol. 2006;30(1):28-33.
90. Wang X, Li Y, Shi T, Bont LJ, Chu HY, Zar HJ, et al. Global disease burden of and risk factors for acute lower respiratory infections caused by respiratory syncytial virus in preterm infants and young children in 2019: a systematic review and meta-analysis of aggregated and individual participant data. Lancet. 2024;403(10433):1241-53.
91. Garcia-Garcia ML, Gonzalez-Carrasco E, Quevedo S, Munoz C, Sanchez-Escudero V, Pozo F, et al. Clinical and virological characteristics of early and moderate preterm infants readmitted with viral respiratory infections. Pediatr Infect Dis J. 2015;34(7):693-9.
92. Wildenbeest JG, Billard MN, Zuurbier RP, Korsten K, Langedijk AC, van de Ven PM, et al. The burden of respiratory syncytial virus in healthy term-born infants in Europe: a prospective birth cohort study. Lancet Respir Med. 2023;11(4):341-53.
93. Chaw PS, Hua L, Cunningham S, Campbell H, Mikolajczyk R, Nair H, et al. Respiratory syncytial virus-associated acute lower respiratory infections in children with bronchopulmonary dysplasia: Systematic review and meta-analysis. J Infect Dis. 2020;222(Suppl 7):S620-S7.
94. Boyce TG, Mellen BG, Mitchel EF, Jr., Wright PF, Griffin MR. Rates of hospitalization for respiratory syncytial virus infection among children in medicaid. J Pediatr. 2000;137(6):865-70.
95. Schmidt B, Kirpalani HJPM. Safe and sound oxygen therapy for extremely preterm infants: a literature review. Pediatr Med. 2022;5:20.
96. Stenson BJ, Tarnow-Mordi WO, Darlow BA, Simes J, Juszczak E, Askie L, et al. Oxygen saturation and outcomes in preterm infants. N Engl J Med. 2013;368(22):2094-104.

97. Badiee Z, Naseri F, Sadeghnia A. Early versus delayed initiation of nasal continuous positive airway pressure for treatment of respiratory distress syndrome in premature newborns: a randomized clinical trial. Adv Biomed Res. 2013;2:4.
98. Ho JJ, Subramaniam P, Sivakaanthan A, Davis PG. Early versus delayed continuous positive airway pressure (CPAP) for respiratory distress in preterm infants. Cochrane Database Syst Rev. 2020;10(10):CD002975.
99. Sotiropoulos JX, Oei JL, Schmolzer GM, Libesman S, Hunter KE, Williams JG, et al. Initial oxygen concentration for the resuscitation of infants born at less than 32 weeks' gestation: a systematic review and individual participant data network meta-analysis. JAMA Pediatr. 2024;178(8):774-83.
100. Sweet DG, Carnielli V, Greisen G, Hallman M, Ozek E, Te Pas A, et al. European Consensus guidelines on the management of respiratory distress syndrome - 2019 update. Neonatology. 2019;115(4):432-50.
101. Hanidziar D, Nakahori Y, Cahill LA, Gallo D, Keegan JW, Nguyen JP, et al. Characterization of pulmonary immune responses to hyperoxia by high-dimensional mass cytometry analyses. Sci Rep. 2020;10(1):4677.
102. Nagato AC, Bezerra FS, Talvani A, Aarestrup BJ, Aarestrup FM. Hyperoxia promotes polarization of the immune response in ovalbumin-induced airway inflammation, leading to a TH17 cell phenotype. Immun Inflamm Dis. 2015;3(3):321-37.
103. Masalunga C, Rozycki HJ, Mainali ES. The impact of hyperoxia on the neonatal and adult developing dendritic cell. Pediatr Res. 2007;62(1):78-82.
104. Baleeiro CE, Wilcoxen SE, Morris SB, Standiford TJ, Paine R, 3rd. Sublethal hyperoxia impairs pulmonary innate immunity. J Immunol. 2003;171(2):955-63.
105. Herrera-Campos AB, Zamudio-Martinez E, Delgado-Bellido D, Fernandez-Cortes M, Montuenga LM, Oliver FJ, et al. Implications of hyperoxia over the tumor microenvironment: an overview highlighting the importance of the immune system. Cancers (Basel). 2022;14(11).
106. Torow N, Marsland BJ, Hornef MW, Gollwitzer ES. Neonatal mucosal immunology. Mucosal Immunol. 2017;10(1):5-17.
107. Kramer BW, Joshi SN, Moss TJ, Newnham JP, Sindelar R, Jobe AH, et al. Endotoxin-induced maturation of monocytes in preterm fetal sheep lung. Am J Physiol Lung Cell Mol Physiol. 2007;293(2):L345-53.

108. Guilliams M, De Kleer I, Henri S, Post S, Vanhoutte L, De Prijck S, et al. Alveolar macrophages develop from fetal monocytes that differentiate into long-lived cells in the first week of life via GM-CSF. J Exp Med. 2013;210(10):1977-92.
109. Granot T, Senda T, Carpenter DJ, Matsuoka N, Weiner J, Gordon CL, et al. Dendritic cells display subset and tissue-specific maturation dynamics over human life. Immunity. 2017;46(3):504-15.
110. Ignacio A, Czyz S, McCoy KD. Early life microbiome influences on development of the mucosal innate immune system. Semin Immunol. 2024;73:101885.
111. Collins A, Weitkamp JH, Wynn JL. Why are preterm newborns at increased risk of infection? Arch Dis Child Fetal Neonatal Ed. 2018;103(4):F391-F4.
112. Morales-Nebreda L, Misharin AV, Perlman H, Budinger GR. The heterogeneity of lung macrophages in the susceptibility to disease. Eur Respir Rev. 2015;24(137):505-9.
113. Hussell T, Bell TJ. Alveolar macrophages: plasticity in a tissue-specific context. Nat Rev Immunol. 2014;14(2):81-93.
114. Hu G, Christman JW. Editorial: Alveolar macrophages in lung inflammation and resolution. Front Immunol. 2019;10:2275.
115. Panahipoor Javaherdehi A, Ghanbari S, Mahdavi P, Zafarani A, Razizadeh MH. The role of alveolar macrophages in viral respiratory infections and their therapeutic implications. Biochem Biophys Rep. 2024;40:101826.
116. Sahoo D, Zaramela LS, Hernandez GE, Mai U, Taheri S, Dang D, et al. Transcriptional profiling of lung macrophages identifies a predictive signature for inflammatory lung disease in preterm infants. Commun Biol. 2020;3(1):259.
117. Kalymbetova TV, Selvakumar B, Rodriguez-Castillo JA, Gunjak M, Malainou C, Heindl MR, et al. Resident alveolar macrophages are master regulators of arrested alveolarization in experimental bronchopulmonary dysplasia. J Pathol. 2018;245(2):153-9.
118. Altamirano-Lagos MJ, Diaz FE, Mansilla MA, Rivera-Perez D, Soto D, McGill JL, et al. Current animal models for understanding the pathology caused by the respiratory syncytial virus. Front Microbiol. 2019;10:873.
119. Rydell-Tormanen K, Johnson JR. The applicability of mouse models to the study of human disease. Methods Mol Biol. 2019;1940:3-22.

120. Collins RA, Gualano RC, Zosky GR, Atkins CL, Turner DJ, Colasurdo GN, et al. Hyperresponsiveness to inhaled but not intravenous methacholine during acute respiratory syncytial virus infection in mice. Respir Res. 2005;6(1):142.
121. Graham BS, Perkins MD, Wright PF, Karzon DT. Primary respiratory syncytial virus infection in mice. J Med Virol. 1988;26(2):153-62.
122. Limkar AR, Percopo CM, Redes JL, Druey KM, Rosenberg HF. Persistent airway hyperresponsiveness following recovery from infection with pneumonia virus of mice. Viruses. 2021;13(5).
123. Jafri HS, Chavez-Bueno S, Mejias A, Gomez AM, Rios AM, Nassi SS, et al. Respiratory syncytial virus induces pneumonia, cytokine response, airway obstruction, and chronic inflammatory infiltrates associated with long-term airway hyperresponsiveness in mice. J Infect Dis. 2004;189(10):1856-65.
124. Bonville CA, Ptaschinski C, Percopo CM, Rosenberg HF, Domachowske JB. Inflammatory responses to acute pneumovirus infection in neonatal mice. Virol J. 2010;7:320.
125. Rosenberg HF, Domachowske JB. Pneumonia virus of mice (PVM): Exploring novel therapeutic options in a severe respiratory disease model. In: Georgiev VS, editor. National Institute of Allergy and Infectious Diseases, NIH: Volume 3: Intramural Research. Totowa, NJ: Humana Press; 2010. p. 353-9.
126. Horsfall FL, Hahn RG. A latent virus in normal mice capable of producing pneumonia in its natural host. J Exp Med. 1940;71(3):391-408.
127. Horsfall FL, Jr., Ginsberg HS. The dependence of the pathological lesion upon the multiplication of pneumonia virus of mice (PVM); kinetic relation between the degree of viral multiplication and the extent of pneumonia. J Exp Med. 1951;93(2):139-50.
128. Schoch CL, Ciufo S, Domrachev M, Hotton CL, Kannan S, Khovanskaya R, et al. NCBI Taxonomy: a comprehensive update on curation, resources and tools. Database (Oxford). 2020;2020.
129. Chambers P, Pringle CR, Easton AJ. Sequence analysis of the gene encoding the fusion glycoprotein of pneumonia virus of mice suggests possible conserved secondary structure elements in paramyxovirus fusion glycoproteins. J Gen Virol. 1992;73 (Pt 7):1717-24.

130. Easton AJ, Chambers P. Nucleotide sequence of the genes encoding the matrix and small hydrophobic proteins of pneumonia virus of mice. Virus Res. 1997;48(1):27-33.
131. Rosenberg HF, Bonville CA, Easton AJ, Domachowske JB. The pneumonia virus of mice infection model for severe respiratory syncytial virus infection: identifying novel targets for therapeutic intervention. Pharmacol Ther. 2005;105(1):1-6.
132. Rosenberg HF, Domachowske JB. Pneumonia virus of mice: severe respiratory infection in a natural host. Immunol Lett. 2008;118(1):6-12.
133. Anh DB, Faisca P, Desmecht DJ. Differential resistance/susceptibility patterns to pneumovirus infection among inbred mouse strains. Am J Physiol Lung Cell Mol Physiol. 2006;291(3):L426-35.
134. Domachowske JB, Bonville CA, Easton AJ, Rosenberg HF. Differential expression of proinflammatory cytokine genes in vivo in response to pathogenic and nonpathogenic pneumovirus infections. J Infect Dis. 2002;186(1):8-14.
135. Ellis JA, Martin BV, Waldner C, Dyer KD, Domachowske JB, Rosenberg HF. Mucosal inoculation with an attenuated mouse pneumovirus strain protects against virulent challenge in wild type and interferon-gamma receptor deficient mice. Vaccine. 2007;25(6):1085-95.
136. Krempl CD, Collins PL. Reevaluation of the virulence of prototypic strain 15 of pneumonia virus of mice. J Virol. 2004;78(23):13362-5.
137. Krempl CD, Lamirande EW, Collins PL. Complete sequence of the RNA genome of pneumonia virus of mice (PVM). Virus Genes. 2005;30(2):237-49.
138. Thorpe LC, Easton AJ. Genome sequence of the non-pathogenic strain 15 of pneumonia virus of mice and comparison with the genome of the pathogenic strain J3666. J Gen Virol. 2005;86(Pt 1):159-69.
139. Dyer KD, Garcia-Crespo KE, Glineur S, Domachowske JB, Rosenberg HF. The pneumonia virus of mice (PVM) model of acute respiratory infection. Viruses. 2012;4(12):3494-510.
140. Cook PM, Eglin RP, Easton AJ. Pathogenesis of pneumovirus infections in mice: detection of pneumonia virus of mice and human respiratory syncytial virus mRNA in lungs of infected mice by in situ hybridization. J Gen Virol. 1998;79 (Pt 10):2411-7.

141. Bem RA, van Woensel JBM, Lutter R, Domachowske JB, Medema JP, Rosenberg HF, et al. Granzyme A- and B-cluster deficiency delays acute lung injury in pneumovirus-infected mice. J Immunol. 2009;184(2):931-8.
142. Khan MM, Poeckel D, Halavatyi A, Zukowska-Kasprzyk J, Stein F, Vappiani J, et al. An integrated multiomic and quantitative label-free microscopy-based approach to study pro-fibrotic signalling in ex vivo human precision-cut lung slices. Eur Respir J. 2021;58(1).
143. Bradley E, Blencowe H, Moller AB, Okwaraji YB, Sadler F, Gruending A, et al. Born too soon: global epidemiology of preterm birth and drivers for change. Reprod Health. 2025;22(Suppl 2):105.
144. Zhang EY, Bartman CM, Prakash YS, Pabelick CM, Vogel ER. Oxygen and mechanical stretch in the developing lung: risk factors for neonatal and pediatric lung disease. Front Med (Lausanne). 2023;10:1214108.
145. Buczynski BW, Maduekwe ET, O'Reilly MA. The role of hyperoxia in the pathogenesis of experimental BPD. Semin Perinatol. 2013;37(2):69-78.
146. Lithopoulos MA, Toussay X, Zhong S, Xu L, Mustafa SB, Ouellette J, et al. Neonatal hyperoxia in mice triggers long-term cognitive deficits via impairments in cerebrovascular function and neurogenesis. J Clin Invest. 2022;132(22).
147. Warner BB, Stuart LA, Papes RA, Wispe JR. Functional and pathological effects of prolonged hyperoxia in neonatal mice. Am J Physiol. 1998;275(1):L110-7.
148. Dylag AM, Haak J, Yee M, O'Reilly MA. Pulmonary mechanics and structural lung development after neonatal hyperoxia in mice. Pediatr Res. 2020;87(7):1201-10.
149. Frey S, Krempl CD, Schmitt-Graff A, Ehl S. Role of T cells in virus control and disease after infection with pneumonia virus of mice. J Virol. 2008;82(23):11619-27.
150. O'Reilly MA, Marr SH, Yee M, McGrath-Morrow SA, Lawrence BP. Neonatal hyperoxia enhances the inflammatory response in adult mice infected with influenza A virus. Am J Respir Crit Care Med. 2008;177(10):1103-10.
151. Lawrence SM, Ruoss JL, Wynn JL. IL-17 in neonatal health and disease. Am J Reprod Immunol. 2018;79(5):e12800.
152. Woods PS, Kimmig LM, Meliton AY, Sun KA, Tian Y, O'Leary EM, et al. Tissue-resident alveolar macrophages do not rely on glycolysis for LPS-induced inflammation. Am J Respir Cell Mol Biol. 2020;62(2):243-55.

153. Cui TX, Brady AE, Zhang YJ, Fulton CT, Goldsmith AM, Popova AP. Early-life hyperoxia-induced Flt3L drives neonatal lung dendritic cell expansion and proinflammatory responses. Front Immunol. 2023;14:1116675.
154. Vandersarren L, Bosteels C, Vanheerswynghels M, Moon JJ, Easton AJ, Van Isterdael G, et al. Epitope mapping and kinetics of CD4 T cell immunity to pneumonia virus of mice in the C57BL/6 strain. Sci Rep. 2017;7(1):3472.
155. Thapa P, Guyer RS, Yang AY, Parks CA, Brusko TM, Brusko M, et al. Infant T cells are developmentally adapted for robust lung immune responses through enhanced T cell receptor signaling. Sci Immunol. 2021;6(66):eabj0789.
156. David C, Verney C, Si-Tahar M, Guillon A. The deadly dance of alveolar macrophages and influenza virus. Eur Respir Rev. 2024;33(174).
157. Rigaux P, Killoran KE, Qiu Z, Rosenberg HF. Depletion of alveolar macrophages prolongs survival in response to acute pneumovirus infection. Virology. 2012;422(2):338-45.
158. Pribul PK, Harker J, Wang B, Wang H, Tregoning JS, Schwarze J, et al. Alveolar macrophages are a major determinant of early responses to viral lung infection but do not influence subsequent disease development. J Virol. 2008;82(9):4441-8.
159. Hartwig SM, Holman KM, Varga SM. Depletion of alveolar macrophages ameliorates virus-induced disease following a pulmonary coronavirus infection. PLoS One. 2014;9(3):e90720.
160. Malainou C, Abdin SM, Lachmann N, Matt U, Herold S. Alveolar macrophages in tissue homeostasis, inflammation, and infection: evolving concepts of therapeutic targeting. J Clin Invest. 2023;133(19).

VIII Declaration

I declare that I have completed this dissertation single-handedly without the unauthorized help of a second party and only with the assistance acknowledged therein. I have appropriately acknowledged and referenced all text passages that are derived literally from or are based on the content of published or unpublished work of others, and all information that relates to verbal communications. I have abided by the principles of good scientific conduct laid down in the charter of the Justus Liebig University of Giessen in carrying out the investigations described in the dissertation.

Miša Gunjak

IX Acknowledgments

I extend my deepest gratitude to my supervisor, Prof. Dr. Rory Morty, for his continuous support, invaluable guidance, and wise advice throughout this project. His mentorship has played a crucial role in my personal and academic growth. I am especially thankful for the opportunity he provided to join the postgraduate program *Molecular Biology and Medicine of the Lung*, which significantly broadened my knowledge and allowed me to connect with inspiring fellow scientists. His encouragement and constructive feedback have been instrumental in shaping this research and my development as an independent scientist.

I would also like to express my sincere appreciation to Prof. Dr. Werner Seeger for granting me the opportunity to begin my PhD in the excellent laboratory of the Max Planck Institute for Heart and Lung Research in Bad Nauheim, as well as for his ongoing advice and support.

My sincere thanks go to the technicians, secretarial staff, and all other employees of the Max Planck Institute, whose essential contributions have greatly supported this work.

I am particularly appreciative of the technical staff in Heidelberg who have undertaken a significant portion of the laboratory work since our relocation. Their dedication and commitment made a profound impact. I would also like to thank the entire Heidelberg lab staff and colleagues for their support and collaborative spirit throughout this endeavor.

I am thankful to Dr. Reinout Bem and Prof. Dr. Job B. M. Van Woensel for their valuable collaboration. Special gratitude goes to Dr. Bem for his expert guidance in virus handling and continual advice throughout the project’s development. I also wish to thank Thijs Lilien for his collaboration in the viral work alongside Dr. Bem and Prof. Dr. Van Woensel.

Finally, I wish to express my heartfelt appreciation to my parents and my sister Tara. Their unwavering support, belief in me, and encouragement have provided constant strength and motivation throughout this journey. Without their love and confidence, this achievement would not have been possible.